博士論文

Stability analysis of non-neutral ion plasma in a linear Paul trap and its application to particle beam dynamics

線形ポールトラップ中に捕獲された
非中性イオンプラズマの安定性解析
とその粒子ビーム力学への応用

福島 慧

広島大学大学院先端物質科学研究科

2016 年 3 月

目次

1. 主論文

Stability analysis of non-neutral ion plasma in a linear Paul trap and its application to particle beam dynamics
(線形ポールトラップ中に捕獲された非中性イオンプラズマの安定性解析とその粒子ビーム力学への応用)
福島　慧

2. 公表論文

(1) Experimental study of resonance crossing with a Paul trap
Hiroki Takeuchi, Kei Fukushima, Kiyokazu Ito, Katsuhiro Moriya, Hiromi Okamoto and Hiroshi Sugimoto
Physical Review Special Topics - Accelerators and Beams **15**, 074201, pp. 1 - 14 (2012).

(2) Experimental verification of resonance instability bands in quadrupole doublet focusing channels
Kei Fukushima, Kiyokazu Ito, Hiromi Okamoto, Shisei Yamaguchi, Katsuhiro Moriya, Hiroyuki Higaki, Toshihiro Okano and Steven M. Lund
Nuclear Instruments and Methods in Physics Research Section A **733**, pp. 18 - 24 (2014).

(3) Design study of a multipole ion trap for beam physics applications
Kei Fukushima and Hiromi Okamoto
Plasma and Fusion Research **10**, 1401081, pp. 1 - 9 (2015).

3. 参考論文

(1) Theoretical study on the stability of Coulomb crystallized beams in periodic focusing channels
Kei Fukushima, Hiromi Okamoto and Hiroshi Sugimoto
Proceedings of the 8th Annual Meeting of Particle Accelerator Society of Japan, pp. 1134 - 1137 (2011).

(2) Plasma traps for space-charge studies: status and perspectives
Hiromi Okamoto, Masahiro Endo, Kei Fukushima, Hiroyuki Higaki, Kiyokazu Ito, Katsuhiro Moriya, Toshihiro Okano, Shisei Yamaguchi and Akihiro Mohri
Proceedings of the 52nd ICFA Advanced Beam Dynamics Workshop on High-Intensity and High-Brightness Hadron Beams (HB2012), pp. 235 - 239 (2012).

(3) Experimental studies of resonance crossing in linear non-scaling FFAGs with the S-POD plasma trap
Suzanne L. Sheehy, David J. Kelliher, Shinji Machida, Chris R. Prior, Kei Fukushima,

Kiyokazu Ito, Katsuhiro Moriya, Toshihiro Okano and Hiromi Okamoto
Proceedings of the 4th International Particle Accelerator Conference (IPAC2013), pp. 2675 - 2677 (2013).

(4) Experimental simulation of beam propagation over long path lengths using radio-frequency and magnetic traps
Hiromi Okamoto, Masahiro Endo, <u>Kei Fukushima</u>, Hiroyuki Higaki, Kiyokazu Ito, Katsuhiro Moriya, Shisei Yamaguchi and Steven M. Lund
Nuclear Instruments and Methods in Physics Research Section A **733**, pp. 119 - 128 (2014).

(5) Beam dynamics studies with non-neutral plasma traps
Hiromi Okamoto, <u>Kei Fukushima</u>, Hiroyuki Higaki, Daiki Ishikawa, Kiyokazu Ito, Takaaki Iwai, Katsuhiro Moriya, Toshihiro Okano, Kazuya Osaki and Mikio Yamaguchi
Proceeding of the 5th International Particle Accelerator Conference (IPAC2014), pp. 4052 - 4056 (2014).

(6) Study of resonance crossing in non-scaling FFAGs using the S-POD linear Paul trap
David J. Kelliher, Shinji Machida, Chris R. Prior, Suzanne L. Sheehy, <u>Kei Fukushima</u>, Kiyokazu Ito, Katsuhiro Moriya, Hiromi Okamoto and Toshihiro Okano
Proceeding of the 5th International Particle Accelerator Conference (IPAC2014), pp. 1571 - 1573 (2014).

(7) Recent results from the S-POD trap systems on the stability of intense hadron beams
Hiromi Okamoto, Kiyokazu Ito, <u>Kei Fukushima</u> and Toshihiro Okano
Proceeding of the 54th ICFA Advanced Beam Dynamics Workshop on High-Intensity, High-Brightness and High-Power Hadron Beams (HB2014), pp. 178 - 182 (2014).

(8) Experimental study of integer-resonance crossing in a non-scaling fixed field alternating gradient accelerator with a Paul ion trap
Katsuhiro Moriya, <u>Kei Fukushima</u>, Kiyokazu Ito, Toshihiro Okano, Hiromi Okamoto, Suzanne L. Sheehy, David J. Kelliher, Shinji Machida and Chris R. Prior
Physical Review Special Topics - Accelerators and Beams **18**, 034001, pp. 1 - 13 (2015).

(9) Experimental study on dipole motion of an ion plasma confined in a linear Paul trap
Kiyokazu Ito, Toshihiro Okano, Katsuhiro Moriya, <u>Kei Fukushima</u>, Hiroyuki Higaki and Hiromi Okamoto
Hyperfine Interactions, DOI 10.1007/s10751-015-1196-y, 9 pages (2015).

主論文

Stability analysis of non-neutral ion plasma in a linear Paul trap and its application to particle beam dynamics

Kei Fukushima

Graduate School of Advanced Sciences of Matter, Hiroshima University

1-3-1 Kagamiyama, Higashi-Hiroshima, Hiroshima, 739-8530 Japan

March 2016

Abstract

It is extremely important to have clear understanding of resonant beam instability for a better design of a modern particle accelerator. For this purpose, we have developed "Simulator of Particle Orbit Dynamics" (S-POD) that enables us to clarify various beam-dynamics issues without relying on large-scale machines. This unique tabletop experiment is based on an isomorphism between non-neutral plasmas in a compact Paul trap and charged-particle beams in a linear focusing channel. S-POD is particularly useful in exploring collective effects in intense hadron beams. This thesis addresses systematic Particle-In-Cell (PIC) simulations performed to explain experimental data from S-POD. A possible design of a novel multipole ion trap is also proposed for a future experiment study of nonlinear beam dynamics. The contents of the present work include the following three main subjects.

(1) Collective resonance instabilities and its lattice-structure dependence [Chapter 4].
Almost all modern particle accelerator systems exploit the principle of strong focusing. Each accelerator has a unique lattice structure optimized for a certain experimental purpose. We here focus on several standard alternating-gradient (AG) lattices such as doublet, triplet, FDDF, etc. These AG focusing potentials can readily be reproduced in S-POD. We employ the PIC code "Warp" to support S-POD experiments. A number of systematic multi-particle simulations are carried out to explain the experimentally observed collective instabilities induced by the external AG driving forces. The excitation of extra resonance bands due to lattice symmetry breaking is also studied in detail. We confirm that PIC simulation results are consistent to experimental observations as well as theoretical predictions from the linearized Vlasov analysis.

(2) Theoretical and simulation study of resonance crossing [Chapter 5].
Considerable theoretical and experimental efforts have recently been devoted to design studies of nonscaling fixed-field alternating gradient (ns-FFAG) accelerators are for various purposes including hadron therapy, accelerator-driven reactor systems, a muon collider, and a neutrino factory. In this type of machines, the bare betatron tunes keep decreasing rapidly while the beam is accelerated by radio-frequency cavities. It is almost inevitable for the operating point to cross resonance stop bands, some of which may be quite dangerous.

In this chapter, we first investigate fundamental features of collective resonance crossing with the Warp code and compare simulation results with experimental observations in S-POD. A simple scaling law is derived for a quick estimate of the emittance growth caused by crossing of an in-

trinsic space-charge-driven resonance. We then proceed to an extensive study of integer resonance crossing. A dipole driving field was intentionally added in recent S-POD experiments to excite integer resonances. We show that experimental results can be well explained by Warp simulations and predictions from analytic models. The rate of ion losses after consecutive crossing of integer resonance bands is evaluated as a function of crossing speed and the relative initial phase of dipole driving forces. An effect of nonlinear external fields, practically unavoidable due to finite mechanical imperfections and other sources, is also briefly studied.

(3) A modified Paul trap for study of nonlinear beam-dynamics studies [Chapter 6].
Any particle accelerators include weak nonlinear fields generated by mechanical errors and even nonlinear multipole magnets for beam orbit correction. Nonlinear error fields are also present in a Paul ion trap, enhancing high-order resonances under certain conditions. The main source of nonlinearity in a regular trap is the misalignments of the quadrupole rods, which means that the strength and time structure of the nonlinear fields cannot be controlled independently of the linear focusing field.

In this chapter, we propose a multipole ion trap that enables us to conduct a systematic experimental study of nonlinear effects in particle accelerators. The proposed modified Paul trap has four extra electrodes in between the regular quadrupole rods. It is possible to control low-order nonlinearities in the plasma confinement potential by applying proper rf voltages to these electrodes. Simple scaling laws are derived for a quick estimation of low-order nonlinear field strengths. We perform test numerical simulations to verify the controllability of sextupole and octupole resonances in the modified trap.

Acknowledgements

Contents

Chapter 1

Introduction

In a modern particle accelerator, high-intensity and high-quality beams are often demanded by physics experiments. The intensity of beam is the product of beam kinetic energy and beam current density. For a high-quality beam, the emittance defined as the volume of the beam in six-dimensional phase space must be low to preserve focusability. The phase space density of a high intensity beam inevitably becomes high - regardless of the absolute beam energy. Consequently, the charged particles composing the beam strongly interact via their repulsive Coulomb fields giving rise to collective response. This collective effect by Coulomb interaction is called the "space charge effect" and can be strongly nonlinear. The space charge effect has the possibility of causing beam instability that leads to the undesirable emittance growth and possible loss of beam particles. Therefore, we have to know the detail of this effect to respond to above demands.

The space charge effect is one of the dominant theme in accelerator physics from the early days, and so various theoretical and experimental studies were provided over the past several decades. However, we still often encounter many problems and tasks requiring analysis of space charge effect.

In the experimental study, we use real accelerators during the operation, but the accelerator is quite expensive and it is very difficult to measure the beam motion with close to the speed of light. Theoretical solutions are also developed, analytical studies are provided from of old but the external fields in the real machines and the multi-particle distributions of the beam are had to approximate quit simply. In addition parameters of an accelerator are decided and fixed in design, the systematic study is also difficult in real machines.

As computational performance advances, numerical simulations are most popular for the design and problem solving of the accelerators. In the numerical study, we can reproduce the external fields with high accuracy and the arbitrary distribution of the beam, but a calculation stress of Coulomb interactions between particles depends on the squared number of the particles. Therefore, we have to introduce some of approximations for beam simulations due to the real beam that consists by too many particles. As a result, the numerical accuracy and the calculating time are related to the trade-off.

To solve problems within a space charge effect, we developed a tabletop experimental tool

"Simulator of Particle Orbit Dynamics" (S-POD). S-POD is a non-neutral plasma trap system based on Ref [1, 2, 3, 4]. for fundamental beam physics studies. This unique experiment is based on the isomorphism between non-neutral plasmas in a compact trap and charged-particle beams in a linear focusing channel; namely, S-POD can approximately reproduce the rest-frame motion of a beam in the laboratory frame, thus enabling us to obtain fundamental beam-dynamics information. Such a handy, inexpensive model experiment could be a powerful means for future beam-physics studies just like modern computer simulations.

In this thesis, we study dynamics of non-neutral ion plasma and its application to particle beam dynamics. It covers various situations of the particle beams and the accelerators by the theoretical and numerical solutions. Particularly, we investigate stabilities of various focusing systems and new accelerator principle and new scheme for the stability with the space-charge effect and the nonlinear fields. The body of this thesis is organized as follows.

In Chap. 2, we describe basic theory and physical analogy between a linear Paul trap (LPT) and a beam transport system of an accelerator. First, the theory of the LPT is reviewed to understand experimental and simulation systems. Next, we deal with the beam dynamics theory and connect to the LPT theory. In Chap. 3, a numerical simulation theory including an integration method, an area weighting, and initial distributions are described. Chapter 4 is started from a collective resonance theory, and we recognize it by numerical methods. Moreover, we provide simulation studies for the lattice structure dependence of the resonance instabilities. In Chap 5, we have studied the effect of resonance crossing on beam stability systematically. First, we assume the collective instabilities due to the resonance crossing. Second, investigate integer resonances that turn into a problem in "EMMA" (Electron Model for Many Applications) accelerator. Chapter 6 shows a new LPT structure for study of nonlinear field effects. In the above studies, the nonlinear effects are actualized in the S-POD. Therefore, we produce a nonlinear-field controllable trap system by extra electrodes.

Chapter 2

Linear Paul trap and Accelerator

2.1 Linear Paul trap

A linear Paul trap (LPT) performs a confinement of non-neutral plasma by a transverse oscillating electric field and a longitudinal static barrier potential [5]. Figure 2.1 is a schematic of a typical LPT. In the Paul trap, the non-neutral plasma is trapped by a radio-frequency (rf) quadrupole field in transverse direction. In addition, we apply static voltages to axial side rods to confine a plasma in axial direction. The Hamiltonian of a particle evolving in a trap has the non-relativisitic form,

$$H = \frac{1}{2m}(\boldsymbol{p} - q\boldsymbol{A})^2 + q\phi. \tag{2.1}$$

Here, m and q are the rest mass and the charge of the particle, and $\boldsymbol{p}$ is the particle canonical momentum with conjugate spatial coordinate $\boldsymbol{x}$, $\boldsymbol{A}$ is the magnetic vector potential, and ϕ is the electric potential. Generally, we set the rf wavelength much larger than the trap size, and consequently $\boldsymbol{A}$ is negligible. The scalar potential ϕ can be written as $\phi = \phi_{\text{ext}} + \phi_{\text{sc}}$ where ϕ_{ext} is an external potential associated with the applied focusing field and ϕ_{sc} is an internal potential generated by the charged particles in the trap and their mirror charges which are induced to the electrodes.

2.1.1 Quadrupole focusing electrodes

A quadrupole field is generated by applying proper rf voltages to the four electrodes with quadrupole symmetry. Each pair of the electrodes facing each other across the trap center has the same rf voltages and neighboring electrodes have the reverse polarity.

This external quadrupole potential which is generated by electrodes can be approximated as

$$\phi_{\text{ext}} \approx \frac{1}{2}\hat{K}(t)(x^2 - y^2), \tag{2.2}$$

where the coefficient $\hat{K}(t)$ is related to the time varying voltage which applied to the electrodes by $\hat{K}(t) = V(t)/R_0^2$. Here, R_0 is the radius of closest approach of the electrodes. In a typical Paul trap, $V(t) = U + V_{\text{rf}}\cos(\omega_{\text{rf}}t)$ is satisfied. Here, $U = \text{const.}$ is a direct current (DC) voltage, V_{rf} is
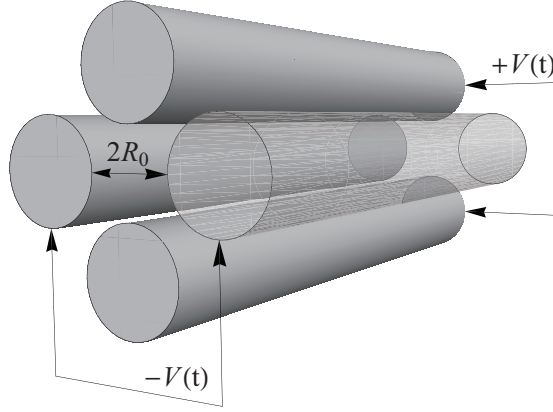
Figure 2.1: A schematics of a linear Paul trap.

the amplitude of rf voltage, and ω_{rf} is the rf angular frequency. Assuming the plasma distribution is uniform on the axial direction, the transverse collective motion of confined charged particles obeys the Hamiltonian

$$H = \frac{p_x^2 + p_y^2}{2m} + \frac{q}{2}\hat{K}(t)(x^2 - y^2) + q\phi_{\text{sc}}.$$ (2.3)

2.1.2 Mathieu equation

If we neglect the space-charge potential ϕ_{sc}, the Hamiltonian (2.3) gives the equations of motion

$$\frac{d^2 x}{dt^2} + \frac{2q}{mR_0^2}(U + V_{\text{rf}}\cos\omega_{\text{rf}}t)x = 0,$$

$$\frac{d^2 y}{dt^2} - \frac{2q}{mR_0^2}(U + V_{\text{rf}}\cos\omega_{\text{rf}}t)y = 0.$$ (2.4)

Note that the x- and y- equations are decoupled. Define dimensionless parameters

$$\xi = \frac{\omega_{\text{rf}}t}{2}, \quad a_M = \frac{8qU}{mR_0^2\omega_{\text{rf}}^2}, \quad q_M = \frac{4qV}{mR_0^2\omega_{\text{rf}}^2},$$ (2.5)

and Eq. (2.4) becomes

$$\frac{d^2 x}{d\xi^2} + (a_M + 2q_M\cos 2\xi)x = 0,$$

$$\frac{d^2 y}{d\xi^2} - (a_M + 2q_M\cos 2\xi)y = 0.$$ (2.6)

This is the standard form of a "Mathieu equation", and the x-equation can solve as

$$x(\xi) = Ae^{\alpha_M\xi} \sum_{n=-\infty}^{+\infty} C_{2n}e^{(2n+\beta_M)i\xi} + Be^{-\alpha_M\xi} \sum_{n=-\infty}^{+\infty} C_{2n}e^{-(2n+\beta_M)i\xi}. \tag{2.7}$$

Here, A and B are the constants determined by the initial condition of the particle and the phase of the external fields. α_M, β_M, and C_{2n} are the constants defined by a_M and q_M. Note that, the equation for y-direction is the same as x-direction without $a_M \to -a_M$ and $q_M \to -q_M$, so

$$y(\xi) = Ae^{\alpha_M\xi} \sum_{n=-\infty}^{+\infty} C_{2n}e^{(2n-\beta_M)i\xi} + Be^{-\alpha_M\xi} \sum_{n=-\infty}^{+\infty} C_{2n}e^{-(2n-\beta_M)i\xi}. \tag{2.8}$$

In order to meet the orbit does not diverge at $\xi \to \pm\infty$, $\alpha_M = 0$ is required. As a result, Eq. (2.7) can be written as

$$x(\xi) = A \sum_{n=-\infty}^{+\infty} C_{2n}e^{(2n+\beta_M)i\xi} + B \sum_{n=-\infty}^{+\infty} C_{2n}e^{-(2n+\beta_M)i\xi}$$

$$= (A+B) \sum_{n=-\infty}^{+\infty} C_{2n}\cos(2n+\beta_M)\xi + i(A-B) \sum_{n=-\infty}^{+\infty} C_{2n}\sin(2n+\beta_M)\xi. \tag{2.9}$$

From this solution, the time variation of the particle $\sin(\omega_n t)$, $\cos(\omega_n t)$, and

$$\omega_n = (2n+\beta_M)\frac{\omega_{\text{rf}}}{2} = n\omega_{\text{rf}} + \frac{\beta_M\omega_{\text{rf}}}{2} \tag{2.10}$$

are given. This shows, the frequency spectrum of the particle motion consists of the fundamental frequency ω_0 and high-order frequencies ω_n. Generally, the fundamental frequency ω_0 has the largest effect contribute to the particle motion, and it is called the "secular motion". Fig 2.2 is an exmaple of a particle orbit with an focusing system. Note that $\omega_0/2\pi$ corresponds to the bare betatron tune ν_0 in accelerator physics (see Sec 2.2).

2.1.3   Stability diagram

In the system which the motion is composed different frequencies, there is a possibility to take an unstable solution which diverges in time and a stable solution which maintains limited amplitude for all time, and the stability depends on β_M. If β_M is an integer value, the motion becomes unstable. For all other values of β_M, the motion is stable. Therefore, the particle motion described by Mathieu equation can be characterized by β_M, and it is also called Mathieu's characteristic exponent. β_M can expressed in terms of a_M and q_M as

$$\beta_M = \sqrt{a_M - \frac{(a_M-1)q_M^2}{2(a_M-1)^2 - q_M^2} - \frac{(5a_M+7)q_M^4}{32(a_M-1)^3(a_M-4)} - \cdots}. \tag{2.11}$$

11
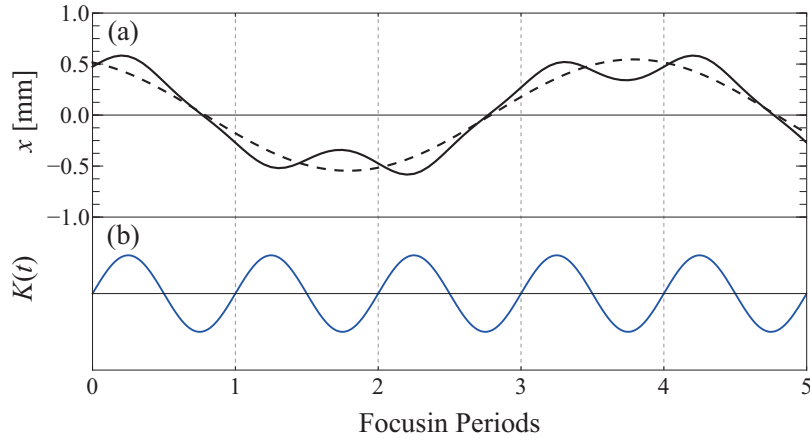
Figure 2.2: (a) The particle orbit (solid line) and the secular motion (dashed line) in a Paul trap. (b) The rf focusing system.

This shows, the stability of the particle motion is defined by a_M and q_M. Fig 2.3 (a) shows the stability region in a_M and q_M space. These stability regions have an axial symmetry on q_M coordinate and overlap partially. If we choose a_M and q_M within these overlapped regions, the particle is stable transversely. Fig 2.3 (b) is the closest region to the origin ($a_M > 0$) and it is called "first stability region".

A typical LPT uses this first stability region for plasma confinement. This correlates to single particle phase advance is designed less than $180°$ per lattice period.

2.2 Physical analogy between a Paul trap and a beam transport channel

2.2.1 Beam transport channel

Beam manipulations in particle accelerators are carried out by using electromagnetic fields. The relativistic Hamiltonian of a charged particle in electromagnetic fields is given by

$$H = q\phi + c\sqrt{(\boldsymbol{p} - q\boldsymbol{A})^2 + m^2c^2}. \tag{2.12}$$

Here c is the speed of light in vacuo. We introduce the Frenet-Serret coordinate system which is typically used in accelerator physics. The orbit which has the design energy of the accelerator is called "design orbit" and it is closed in the circuit of the ring generally [6, 7]. We define the axial beam position along the design orbit as s, the axial direction within the beam as z, the horizontal directions orthogonal to z as x (bend-plane), and its vertical (out of bend plane) direction as y. Then, The s component C_s of an arbitrary vector $\boldsymbol{C}$ is

$$C_s = C_x \frac{\partial x}{\partial s} + C_y \frac{\partial y}{\partial s} + C_z \frac{\partial z}{\partial s} = \left(1 + \frac{x}{\rho}\right) C_z, \tag{2.13}$$

12
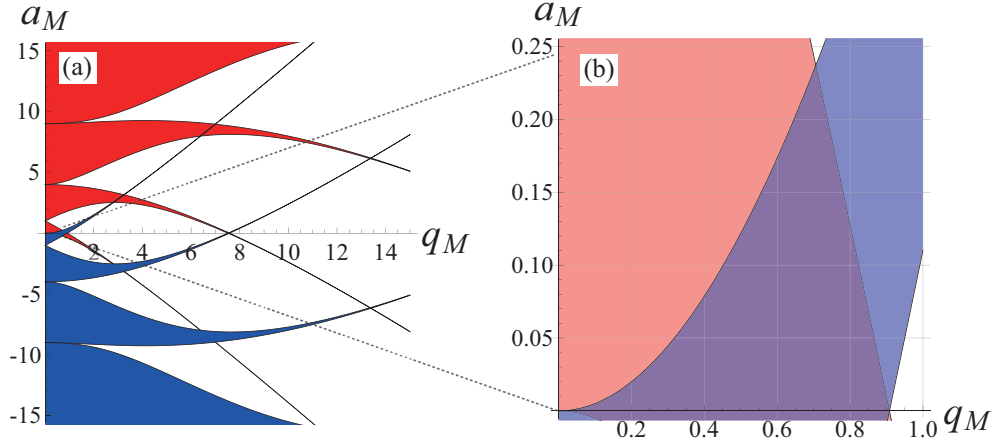
Figure 2.3: (a) Stability regions (color) of the Mathieu equation. x-coordinate stability region is shown in red, and y-coordinate is blue. These regions have an axial symmetry to $q_M < 0$. (b) Mathieu's first stability region($a_M > 0$). The boundaries correspond to $\beta_M = 0$ and $\beta_M = 1$ lines.
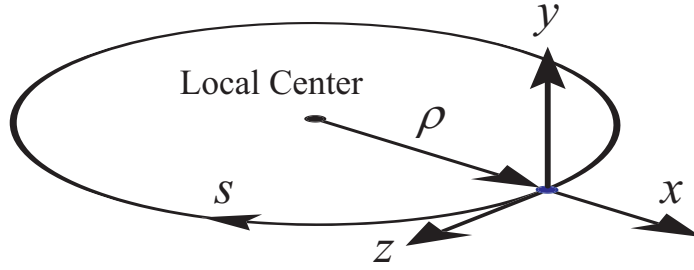
Figure 2.4: Frenet-Serret coordinate system

where ρ is the local radial curvature in the bend plane. Generally, these x ans y is called transverse direction and z is called axial direction.

The vector potentials in the new coordinate system are

$$A_s = \boldsymbol{A} \cdot \hat{s}, \quad A_x = \boldsymbol{A} \cdot \hat{x}, \quad A_y = \boldsymbol{A} \cdot \hat{y}, \tag{2.14}$$

and the Hamiltonian is

$$H = q\phi + c\sqrt{(p_x - qA_x)^2 + (p_y - qA_y)^2 + \left(\frac{p_s - qA_s}{1 + x/\rho}\right)^2 + m^2 c^2}. \tag{2.15}$$

The independent variable in H is the time t, but the momentum of the each particle is different, so the external potential is not a periodic function of t generally. Therefore, we convert the independent variable from the time t to the position on the design particle orbit s. The conjugate momentum about the time t is $-H = -E = $ const, and the new Hamiltonian $\hat{H}$ with the

independent variable s is given by $H - p_s$. As a result, by using the total kinetic momentum $p = \sqrt{(E - q\phi)^2/c^2 - m^2c^2}$, and the new Hamiltonian $\hat{H}$ is

$$\hat{H} = -\left(1 + \frac{x}{\rho}\right)\left(qA_s + \sqrt{(p_x - qA_x)^2 - (p_y - qA_y)^2 - \frac{(E - q\phi)^2}{c^2} - m^2c^2}\right). \tag{2.16}$$

This new Hamiltonian $\hat{H}$ will hereafter be denoted as H. A typical accelerator satisfies $|p_x/p| \ll 1$ and $|p_y/p| \ll 1$ (paraxial approximation), so we can analyse the linearized Hamiltonian

$$\hat{H} \approx -\left(1 + \frac{x}{\rho}\right)\left(qA_s + p - \frac{(p_x - qA_x)^2 + (p_y - qA_y)^2}{2p}\right). \tag{2.17}$$

to approximate the motion. Here, the relation between the momentum deviation and the energy deviation is

$$\delta p \equiv p - p_0 \approx \frac{\Delta E}{\beta_0 c} - \frac{1}{2p_0}\left(\frac{\Delta E}{\beta_0 c \gamma_0}\right)^2 - \frac{q\phi_{\text{sc}}}{\beta_0 c}, \tag{2.18}$$

and we approximate the Hamiltonian as

$$H \approx \left(1 + \frac{x}{\rho}\right)\left(-qA_s + \frac{(p_x - qA_x)^2 + (p_y - qA_y)^2}{2p_0} \right. $$
$$\left. + \frac{q\phi_{\text{sc}}}{\beta_0 c \gamma_0^2} - \frac{\Delta E}{\beta_0 c} + \frac{1}{2p_0}\left(\frac{\Delta E}{\beta_0 c \gamma_0}\right)^2\right), \tag{2.19}$$

where γ_0 and β_0 are the axial Lorentz factors, p_0 is the momentum on the design orbit and ϕ_{sc} is the self potential of the beam. For the case of the single particle motion with $\phi_{\text{sc}} = 0$, this Hamiltonian is expressed with $\Delta E/(\beta_0 c \gamma_0) = p_z$ as

$$H = \left(1 + \frac{x}{\rho}\right)\left(-\frac{qA_s}{p_0} + \frac{(p_x - qA_x)^2 + (p_y - qA_y)^2 + p_z^2}{2} - \gamma_0 p_z\right). \tag{2.20}$$

In this equation, we applied the following normalization,

$$H \to H/p_0, \ p_x \to p_x/p_0, \ p_y \to p_y/p_0, \ p_z \to p_z/p_0. \tag{2.21}$$

2.2.2 Quadrupole focusing potential

A quadrupole field in an accelerator is similar to a Paul trap field. In the focusing quadrupole magnet, the beam is focused in the x-direction and defocused in the y-direction at the same time. Conversely, the defocusing quadrupole magnet generates focusing force in the y-direction and defocusing in the x-direction. The "alternating gradient (AG) focusing" is realized by the combi-

14

nation of the focusing and defocusing magnets. The Hamiltonian of a charged particle in the ideal quadrupole magnet is

$$
\begin{cases}
\boldsymbol{A} & = \left(0, 0, \pm \frac{1}{2} B_1 \left(x^2 - y^2\right)\right) \\
1/\rho(s) & = 0
\end{cases}
\tag{2.22}
$$

$$
H_{\text{quad}} = \frac{p_x^2 + p_y^2 + p_z^2}{2} \pm \frac{1}{2} K(x^2 - y^2).
\tag{2.23}
$$

Here, B_1 is the gradient of the quadrupole field which is defined by $K = qB_1/p_0$.

2.2.3 Dipole bending potential

A dipole field is mainly in order to bend a charged particle beam. For example, it is used to make a closed orbit in a storage ring or introduce a beam to a ring. The vector potential and the Hamiltonian are written as

$$
\begin{cases}
\boldsymbol{A} & = \left(0, 0, -\frac{p_0}{2q} \left(1 + \frac{x}{\rho}\right)\right) \\
1/\rho(s) & = \text{const.}
\end{cases}
\tag{2.24}
$$

$$
H_{\text{dipole}} = \frac{p_x^2 + p_y^2 + p_z^2}{2} + \frac{1}{\rho^2} x^2 - \left(1 + \frac{x}{\rho}\right) \gamma_0 p_z.
\tag{2.25}
$$

In the ideal bending magnet strength is defined by the radial curvature ρ also, and it satisfies $B_0 \rho = \gamma_0 \beta_0 mc/q$.

2.2.4 Hill's equation

A single charged particle transverse motion in an accelerator which is consisted by linear fields is

$$
\frac{d^2 x}{ds^2} + K(s)x = 0
\tag{2.26}
$$

This equation of motion is the same between x-direction and y-direction without the sign of $K(s)$. $K(s)$ is the quadrupole focusing function in a ring. In the LPT, the independent variable of the focusing function is the time t, on the other hand, in the accelerator, the independent variable is the position of the beam. When the focusing function has a periodicity, the particles are oscillated by the focusing fields and this transverse oscillation is so called "betatron oscillation". In addition, this equation concludes the "Hill's equation". According to the Floquet theory, the solution of the Hill's equation is known as

$$
x(s) = \sqrt{\varepsilon \beta(s)} \cos(\mu(s) + \mu_0),
\tag{2.27}
$$

where ε and μ_0 are the constants which defined by the initial condition of the particle. $\beta(s)$ and $\mu(s)$ are the beta- and the phase- function following the next formulas,

$$\frac{d^2}{ds^2}\sqrt{\beta} + K(s)\sqrt{\beta} - \frac{1}{\sqrt{\beta}^3},$$ (2.28)

$$\mu(s) = \int_{s_0}^{s} \frac{1}{\beta(s)} ds.$$ (2.29)

$\beta(s)$ is the scaled amplitude, and so it does not depend on the initial distribution of the beam. Therefore, the beta function is used for the index of the focusing system in the accelerator. The betatron frequency per one focusing period is called "betatron tune" or simply "tune" and represented by ν, and also defined as following

$$\nu = \frac{\mu(s_0 + L) - \mu(s_0)}{2\pi} = \frac{1}{2\pi} \oint \frac{1}{\beta(s)} ds.$$ (2.30)

Here L is lattice period. This tune is correlated to the effective focusing strength of the beam and important parameter of the accelerator. The frequency is depend on the Coulomb interaction force also, and so the frequency without the self-interaction force is called "bare tune ν_0".

2.2.5 Twiss parameters and transfer matrix

Eq. (2.27) can be rewritten as

$$x(s) = A\sqrt{\varepsilon\beta(s)}\exp[i\mu(s)] + B\sqrt{\varepsilon\beta(s)}\exp[-i\mu(s)].$$ (2.31)

As the initial condition at $s = 0$, set x_0 and $x_0' \equiv \frac{dx_0}{ds}$, and the arbitrary constants A and B are

$$A = \frac{1}{2}[x_0 X_0 \mu_0' - \mathrm{i}(x_0' X_0 - x_0 X_0')]\exp[-i\mu(s)],$$ (2.32)

$$B = \frac{1}{2}[x_0 X_0 \mu_0' + \mathrm{i}(x_0' X_0 - x_0 X_0')]\exp[i\mu(s)].$$ (2.33)

Here, $\sqrt{\varepsilon\beta(s)} = X(s)$ and $X_0^2 \mu_0' = 1$.

These linear ordinary differential equations can be rewritten by a matrix. In accelerator physics, a matrix for a beam focusing system is called "transfer matrix", and described with a phase-space vector $Q = \begin{pmatrix} x \\ x' \end{pmatrix}$,

$$Q(s) = M(s)Q(s_0)$$ (2.34)

Substitute them for Eq. (2.31), and obtain the transfer matrix

$$M(s|0) = \begin{pmatrix} m_{11} & m_{12} \\ m_{21} & m_{22} \end{pmatrix}$$ (2.35)

$$
\left\{
\begin{array}{l}
m_{11} = \dfrac{X(s)}{X_0}\cos(\mu(s) - \mu_0) - X_0' X(s)\sin(\mu(s) - \mu_0)] \\[3mm]
m_{12} = X_0 X(s)\sin(\mu(s) - \mu_0) \\[3mm]
m_{21} = \left(\dfrac{X'(s)}{X_0} - \dfrac{X_0'}{X(s)}\right)\cos(\mu(s) - \mu_0) - \left(\dfrac{1}{X_0 X(s)} - X_0' X(s)\right)\sin(\mu(s) - \mu_0) \\[3mm]
m_{22} = \dfrac{X_0}{X(s)}\cos(\mu(s) - \mu_0) - X_0 X'(s)\sin(\mu(s) - \mu_0)]
\end{array}
\right.
\qquad (2.36)
$$

Now, introduce the following parameters,

$$
\left.
\begin{array}{l}
\alpha(s) = -\dfrac{1}{2}\dfrac{d\beta(s)}{ds}, \\[4mm]
\gamma(s) = \dfrac{1 + \alpha(s)^2}{\beta(s)},
\end{array}
\right\}
\qquad (2.37)
$$

and the transfer matrix $M(s)$ is written as

$$
M(s) = \begin{pmatrix} \cos\sigma + \alpha(s)\sin\sigma & \beta(s)\sin\sigma \\ -\gamma(s)\sin\sigma & \cos\sigma - \alpha(s)\sin\sigma \end{pmatrix}.
\qquad (2.38)
$$

These parameters are so called "twiss parameter" and depended on only s and its focusing system [6]. In addition, $\mu(s+L) - \mu(s)$ has the same meaning as the tune. It is called "phase advance σ" and given as

$$
\sigma = \mu(s+L) - \mu(s) = \int_s^{s+L}\frac{1}{X(s)^2}ds = \int_s^{s+L}\frac{1}{\beta(s)}ds.
\qquad (2.39)
$$

2.2.6 Courant-Snyder invariant and emittance

Using the twiss parameter, the solution of the Hill's equation is written as

$$
\begin{array}{rcl}
x(s) & = & \sqrt{\varepsilon\beta(s)}\cos(\mu(s) + \mu_0), \\[4mm]
x'(s) & = & -\sqrt{\dfrac{\varepsilon}{\beta(s)}}[\alpha(s)\cos(\mu(s) + \mu_0) + \sin(\mu(s) + \mu_0)] \\[4mm]
& = & -\sqrt{\varepsilon\gamma(s)}\sin(\mu(s) + \mu_0).
\end{array}
\qquad (2.40)
$$

From these equations, we can obtain the constant value as

$$
\gamma x^2 + 2\alpha x x' + \beta x'2 = \varepsilon = \text{constant}.
\qquad (2.41)
$$
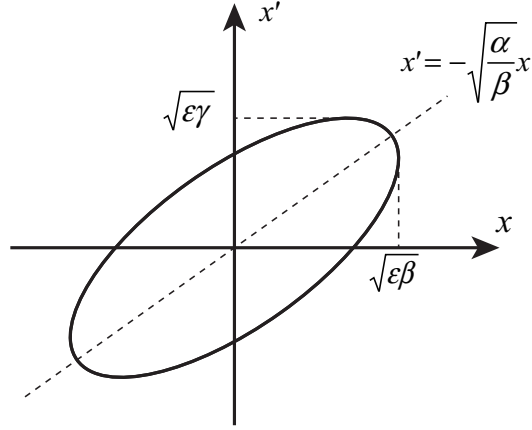
Figure 2.5: A particle orbit in phase space.

This ε does not depend on s, and so called "Courant-Snyder Invariant". Here, ε is determined by the initial condition of the particles and $\pi\varepsilon$ in Fig 2.5 shows the area of the ellipse in the phase-space. Therefore, we can represent the quality of the beam by using this invariant and it is so call "emittance". In other words, the area which is occupied by the constant rate is the emittance, and so the smaller emittance means high quality beam. The definition of the "constant rate" varies with the accelerator or the beam species.

2.2.7 Stability condition of linear beam transport

It is known to the determination of the transfer matrix becomes 1,

$$\det M = (\cos\sigma + \alpha\sin\sigma)(\cos\sigma - \alpha\sin\sigma) + \beta\gamma\sin^2\sigma \qquad (2.42)$$
$$= 1. \qquad (2.43)$$

This also shows the particle motion does not attenuate and the emittance is saved in the transformation. It is known as Liouville's theorem.

Also, the trace of the transfer matrix shows the stability of the particle orbit. The phase-space vector Q after n times passed the periodic focusing system is

$$Q_n = M^n Q \qquad (2.44)$$
$$= c_1 M^n Q_1 + c_2 M^n x_2 \qquad (2.45)$$
$$= c_1 \lambda_1^n Q_1 + c_2 \lambda_2^n Q_2, \qquad (2.46)$$

where λ_1 and λ_2 are the eigenvales, Q_1 and Q_2 are the eigenvectors. In order not to diverge Q_n

by $n \to \infty$, $|\lambda_1| < 1$ and $|\lambda_2| < 1$ is required. The eigenvalue equation is written as

$$\det(M - \lambda I) = \lambda^2 - 2\lambda \cos \sigma + \det M \tag{2.47}$$
$$= \lambda^2 - 2\lambda \cos \sigma + 1 = 0, \tag{2.48}$$

and the eigenvalues are given as

$$\left.\begin{array}{c} \lambda_1 + \lambda_2 = 2\cos\sigma, \\ \\ \lambda_1 \lambda_2 = 1. \end{array}\right\} \tag{2.49}$$

$$\lambda_1, \lambda_2 = e^{\pm i\sigma} \tag{2.50}$$

As a result, we can obtain the necessary and sufficient condition for the stable particle orbit,

$$-1 < \cos \sigma < 1. \tag{2.51}$$

Here, using $\mathrm{Tr}M = 2\cos\sigma$ and the stability condition is written as

$$|\mathrm{Tr}M| < 2. \tag{2.52}$$

This condition is the same meaning as the mathieu's stability condition.

2.2.8 Analogy between the two dynamical systems

The Hamiltonian of the 2D beam in quadrupole transport system is given by Eq. (2.19) and (2.22),

$$H_{\mathrm{beam}} = \frac{p_x^2 + p_y^2}{2} + \frac{1}{2}K(s)(x^2 - y^2) + \frac{q}{p_0\beta_0 c \gamma_0^2}\phi_{\mathrm{sc}}. \tag{2.53}$$

where ignoring the axial motion of the beam. This Hamiltonian is the same as Eq. (2.3) without the coefficients [1, 2]. Now we apply the following scaling to Eq. (2.3)

$$\frac{H}{mc^2} \to H_{\mathrm{trap}}, \quad \frac{p_x}{mc} \to p_x, \quad \frac{p_y}{mc} \to p_y, \tag{2.54}$$

and it is reduced to

$$H_{\mathrm{trap}} = \frac{p_x^2 + p_y^2}{2} + \frac{1}{2}K_{\mathrm{p}}(\tau)(x^2 - y^2) + \frac{q}{mc^2}\phi_{\mathrm{sc}}, \tag{2.55}$$

where

$$K_{\mathrm{p}}(\tau) = \frac{2qV(\tau)}{mc^2 R_0^2}, \tag{2.56}$$

19

and the scaled independent variable is $\tau = ct$. Therefore, in this scaling transformation, we can consider the non-neutral plasma in the trap as the light speed beam in the accelerator ignoring Lorentz factors.

2.3 Some useful formulas

Charged particles are interacted by their self-potential and consist a Coulomb system. In beam dynamics, this internal Coulomb interaction is so called the space charge effect. Space charge effect can ignore in a rarefied beam or close to the speed of light beam like an electron beam. However, in the modern high intensity beam, it affects to the particle motion and the beam stability. In this section, we introduce the linear theory including space charge effect.

2.3.1 Vlasov-Poisson model

Here, we assume an longitudinal-uniform (coasting) beam or non-neutral plasma, and so it can be ignore that the longitudinal collective motion. Therefore, the self potential ϕ_{sc} satisfies the following 2D Poisson equation with Liouville's theorem [8],

$$\nabla^2 \phi_{\text{sc}} = -\frac{q}{\varepsilon_0} \int f dp_x dp_y. \tag{2.57}$$

In the case of ignoring the Coulomb collision effect in the beam, the phase-space distribution function f satisfies the Vlasov equation,

$$\frac{\partial f}{\partial s} + [f, H] = 0. \tag{2.58}$$

Here, [,] denotes the Poisson bracket and assuming the following 2D Hamiltonian,

$$H = \frac{p_x^2 + p_y^2}{2} + K_x(t)\frac{x^2}{2} + K_y(t)\frac{y^2}{2} + q\phi_{sc}. \tag{2.59}$$

As an evaluation method of a space charge effect, solve these three simultaneous equations and obtain a solution of a distribution function. KV distribution is known as a stationary solution of a Vlasov-Poisson equation in a periodic focusing system [9]. The smoothed KV distribution is defined as

$$f(x,y,p_x,p_y) = \frac{N}{\pi^2 \varepsilon_x \varepsilon_y} \delta \left(\frac{x^2}{a^2} + \frac{y^2}{b^2} + \frac{a^2 p_x^2}{\varepsilon_x^2} + \frac{b^2 p_y^2}{\varepsilon_y^2} - 1 \right). \tag{2.60}$$

$a(s)$ and $b(s)$ are the beam size of x- and y-directions, and N is the particle line density. This distribution often uses for analytical solution due to it has linear space-charge force.

However, KV distribution is not a realistic distribution, and it is very hard to obtain the time evolution of the general distribution by analytically. Accordingly, the multi-particle simulation is popular to solve the time evolution. In the general numerical simulation, the program does not

solve Vlasov equation directly, but integrates the equation of motion of the particles [10, 11, 12, 13, 14, 15].

2.3.2 RMS envelope equation

One analytical solution of the space charge effect which based on statical averaged values is given by Sacherer [16, 17, 18]. This equation is developed from the self-consistent distribution case so called KV envelope equation to the elliptic symmetry distribution. Start from one particle in the beam, and it satisfies

$$x' = p_x, \tag{2.61}$$

$$p_x' = F_{\text{ext}} + F_{\text{sc}}, \tag{2.62}$$

where F_{ext} is the external force and F_{sc} is the internal (space charge) force. From the Vlasov equation, 1st order moments are,

$$\bar{x}' = \overline{p_x}, \tag{2.63}$$

$$\overline{p_x}' = \overline{F_{\text{ext}} + F_{\text{sc}}} = -K_x(s)\bar{x} + \overline{F_{\text{sc}}}. \tag{2.64}$$

Also, 2nd order moments are written as

$$\overline{x^2}' = 2\overline{xx'} = 2\overline{xp_x} \tag{2.65}$$

$$\overline{xp_x}' = \overline{x'p_x} + \overline{xp_x'} = \overline{p_x^2} - K_x(s)\overline{x^2} + \overline{xF_{\text{sc}}} \tag{2.66}$$

$$\overline{p_x^2}' = 2\overline{p_xp_x'} = -2K_x(s)\overline{xp_x} + 2\overline{p_xF_{\text{sc}}}. \tag{2.67}$$

Now, define the rms emittance for the elliptic symmetry distribution beam,

$$\varepsilon_x^{\text{rms}} \equiv \sqrt{\overline{x^2}\,\overline{p_x^2} - \overline{xp_x}^2}, \; \varepsilon_y^{\text{rms}} \equiv \sqrt{\overline{y^2}\,\overline{p_y^2} - \overline{yp_y}^2}. \tag{2.68}$$

Assuming the elliptic symmetry distribution function as

$$f(x, y, p_x, p_y ; s) = f\left(\frac{x^2}{x_{\text{rms}}^2} + \frac{y^2}{y_{\text{rms}}^2}, p_x, p_y; s\right). \tag{2.69}$$

The solution is known as the rms envelope equation and given by

$$\frac{d^2 x_{\text{rms}}}{ds^2} + K_x(s)\, x_{\text{rms}} - \frac{(\varepsilon_x^{\text{rms}})^2}{x_{\text{rms}}^3} - \frac{K_{\text{sc}}}{2(x_{\text{rms}} + y_{\text{rms}})} = 0, \tag{2.70}$$

$$\frac{d^2 y_{\text{rms}}}{ds^2} + K_y(s)\, y_{\text{rms}} - \frac{(\varepsilon_y^{\text{rms}})^2}{y_{\text{rms}}^3} - \frac{K_{\text{sc}}}{2(x_{\text{rms}} + y_{\text{rms}})} = 0, \tag{2.71}$$

where $x_{\text{rms}} = \sqrt{\overline{x^2}}$, $y_{\text{rms}} = \sqrt{\overline{y^2}}$, and $K_{\text{sc}} = 2Nr_p/(\beta_0^2\gamma_0^3)$ is the beam perveance which is proportionally to the beam current. Here, N is the number of particle and r_p is the classical radius of the

particle. The rms beam size satisfies this rms envelope equation. This equation is difficult to solve without definition of the time evolution of the rms emittance, however, the rms emittance is almost constant in the equilibrium state beam. Therefore, it is generally solved with this assumption. Also, the KV emittance has following relation to the rms emittance

$$\varepsilon_{x(y)} = 4\varepsilon_{x(y)}^{\mathrm{rms}}. \tag{2.72}$$

In the KV distribution, the particles distribute uniformly and the outermost shell radius is twice as large as the rms radius. The rms emittance is the effective emittance in the macro scale, and so the emittance grows up by the resonance instability in the numerical simulation etc.

On the other hand, the rms envelope equation can be rewritten as the time-dependent equations for the Paul trap [2],

$$\frac{d^2 x_{\mathrm{rms}}}{dt^2} + \hat{K}_x(t)\, x_{\mathrm{rms}} - \frac{(\varepsilon_x^{\mathrm{rms}} c)^2}{x_{\mathrm{rms}}^3} - \frac{K_{\mathrm{sc}} c^2}{2(x_{\mathrm{rms}} + y_{\mathrm{rms}})} = 0, \tag{2.73}$$

$$\frac{d^2 y_{\mathrm{rms}}}{dt^2} + \hat{K}_y(t)\, y_{\mathrm{rms}} - \frac{(\varepsilon_y^{\mathrm{rms}} c)^2}{y_{\mathrm{rms}}^3} - \frac{K_{\mathrm{sc}} c^2}{2(x_{\mathrm{rms}} + y_{\mathrm{rms}})} = 0, \tag{2.74}$$

and,

$$\hat{K}_{x,y}(t) = \frac{2q}{mR_0^2}(U + V_{\mathrm{rf}}\cos\omega_{\mathrm{rf}} t), \tag{2.75}$$

where the constants are the same as Eq. (2.4).

2.3.3   Tune shift and tune depression

The effective focusing strength is reduced by the Coulomb repulsion force, therefore the tune is depressed. This depressed tune is called "incoherent tune v" and the difference between the incoherent tune and bare tune is called "tune shift Δv". The incoherent tune is given by the periodic solution of the envelope equation,

$$v_x = \frac{\varepsilon_x}{2\pi}\oint \frac{1}{a^2}ds = \frac{\varepsilon_x^{\mathrm{rms}}}{2\pi}\oint \frac{1}{x_{\mathrm{rms}}^2}ds, \tag{2.76}$$

$$v_y = \frac{\varepsilon_y}{2\pi}\oint \frac{1}{b^2}ds = \frac{\varepsilon_y^{\mathrm{rms}}}{2\pi}\oint \frac{1}{y_{\mathrm{rms}}^2}ds, \tag{2.77}$$

where $a(s) = 2x_{\mathrm{rms}}(s)$ and $b(s) = 2y_{\mathrm{rms}}(s)$.

As an index of a space-charge effect, a tune shift and a tune depression are used. The tune depression is written by the bare tune and the incoherent tune,

$$\eta = \frac{v}{v_0}. \tag{2.78}$$

In the case of the tune depression close to one, it means the plasma is rarefied.
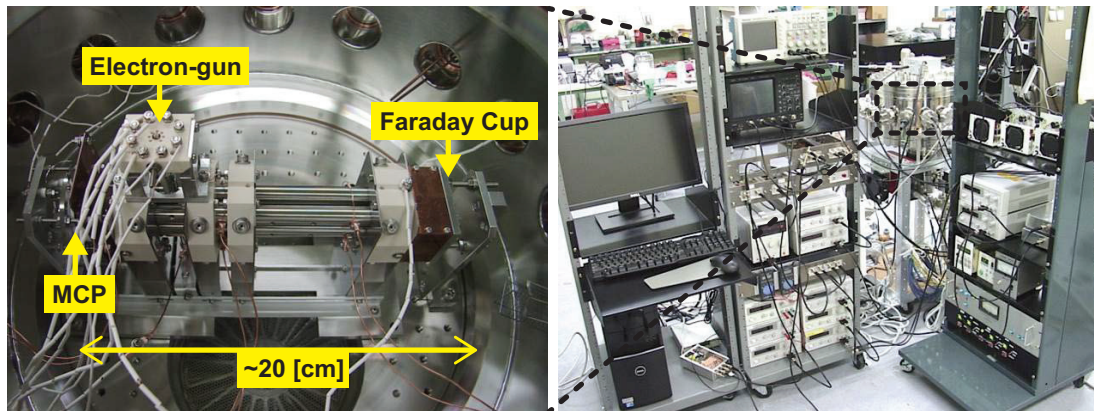
Figure 2.6: Overview of the S-POD system. Right picture is the whole control system of the S-POD. Left picture is the S-POD trap system in the vacuum chamber.

2.4 Simulator of Particle Orbit Dynamics

At Hiroshima University, a unique tabletop tool called "S-POD" (Simulator of Particle Orbit Dynamics) has been developed which allows acceleratorfree experiments on diverse beam-dynamics issues. The S-POD system is based on a compact linear Paul trap in which we can confine a large number of ions. As we mentioned above, a non-neutral plasma stored in the trap can be made approximately equivalent to a charged particle beam in an alternating-gradient (AG) transport channel [1]

2.4.1 Overview

Figure 2.6 is the overview of the whole S-POD system and Fig 2.7 is the schematic sideview of the trap system. The trap system is set up in the vacuum chamber, consisted by the five sections of the quadrupole electrodes, the electron gun (e-gun), the micro channel plate (MCP), and the Faradey cup. In the experiments, accumulate the Ar^+ ions in the trap mostly. First, we ionize neutral Ar gas with a low energy electron beam from the e-gun in section A in Fig 2.7. Second, stop the e-gun and check the stability of the Ar plasma for few msec. We often use 1MHz rf voltage for the quadrupole. In this case, one msec correspond to one thousand focusing cells. After that, measure the number of confined ions with a Faraday cup or a MCP by dropping one of the axial DC potential barriers. The Faraday cup is used for measurement of large number ($> 10^6$) of ions, conversely, The MCP is used for the small number ($< 10^6$) of ions. In our trap system, The vacuum pressure before the ionization procedure is less than 10^{-7} Pa. These S-POD experiments process is controlled by a personal computer with an extensive "LabVIEW"-based system. This system can carry out a large number of systematic measurements quickly and automatically.

---

[1]Gilson, Davidson, and their coworkers of Princeton Plasma Physics Laboratory also constructed a linear Paul trap for beam physics purposes. Their trap geometry is not the most popular four-rod type but a cylinder consisting of four 90-degree azimuthal sectors. The system is referred to as "PTSX" (Paul Trap Simulator Experiment) that has produced fruitful experimental results for the last decade [19, 20, 21].

Axial Potential Configuration
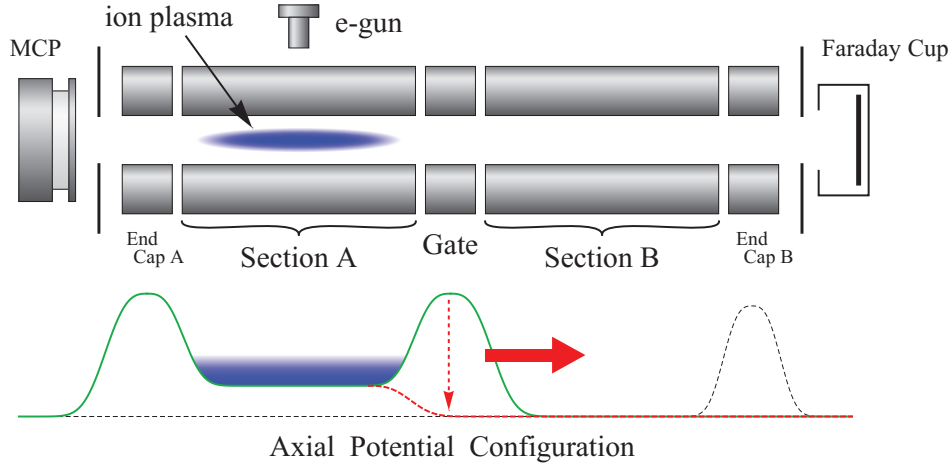
Figure 2.7: A schematic of a typical linear Paul trap for S-POD. The quadrupole rods of the multi-sectioned LPT for S-POD are divided into five electrically independent pieces [3, 4]. We can form two axial potential wells simultaneously by applying DC bias voltages to both the "End Caps" and "Gate" quadrupoles. We mostly confine ions in Section A above which an electron gun is installed for ionizing neutral gases. Ion plasmas are eventually detected either by a Faraday cup or by a micro-channel plate sitting on both sides of the trap. In order to use the Faraday cup for ion number measurements, the DC bias voltage on the Gate quadrupole is dropped to release the plasma from Section A. Section A is typically biased with a low DC voltage to accelerate ions toward the detector in the measurement process.

As noted above, the ideal LPT confine the plasma with the quadrupole field, so the electrodes should have hyperbola surfaces. However, it is difficult to make accurate hyperbola electrodes. By the practical reason, cylindrical electrodes are used to the S-POD. The electrostatic potential field F produced by the cylindrical electrodes has high order nonlinearities. F can be expanded in cylindrical polar coordinates (r, θ),

$$F(r, \theta) = \sum_{n=1}^{\infty} W_n \left(\frac{r}{R_0} \right)^n \cos(n\theta + \varphi_n). \tag{2.79}$$

Here, W_n and φ_n are constant amplitudes defined by the applied voltage and the geometry of the electrodes. Figure 2.8 is the relation between the transverse bare tune and the rf quadrupole voltage in our trap system (inner radius $R_0 = 5$ [mm] and rf frequency is 1 MHz). In this case, the operating point will break out of the Mathieu first stability region at about 90 V.

In addition, it is not negligible that the nonlinear field caused by the electrodes misalignment. Figure 2.9 shows the multipole field amplitude by the rms electrodes misalignments.

2.4.2 Axial plasma confinement

Figure 2.10 shows the longitudinal barrier potential in the S-POD on central axis. This potential is calculated with the numerical field solver. We generally choose the trap parameters for $R_0 = 5$ [mm], the length of the Section A is 75 mm, and the length of the End Cap A and the Gate are
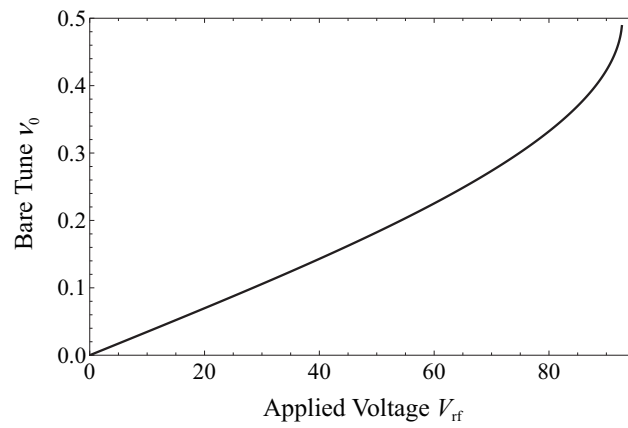
Figure 2.8: The relation between the transverse bare tune ν_0 and the applied rf quadrupole voltage V_{rf} where the rf frequency is 1 MHz.

17 mm. In this case, the longitudinal potential shapes like square well, and the confined plasma is able to approximate longitudinal uniform distribution in the middle of the trap.
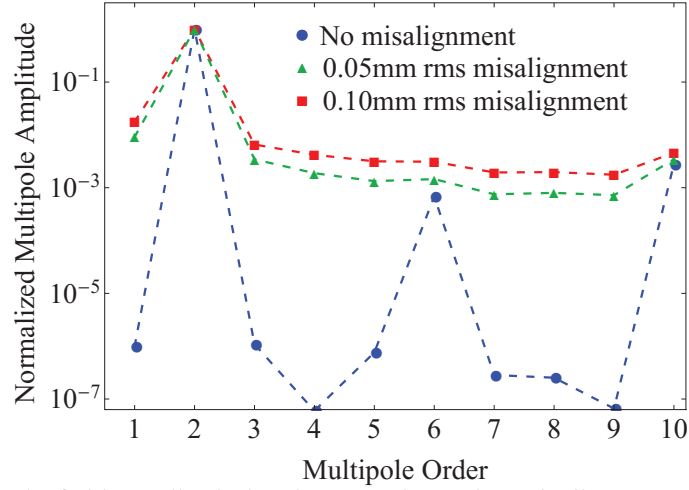
Figure 2.9: Multipole field amplitude by the rms electrodes misalignments. The amplitude is scaled by the 2nd order (quadrupole) field amplitude. Blue symbols are multipole amplitudes of the cylindrical electrodes without misalignment. Red and green symbols show the multipole amplitudes with 0.05 mm and 0.10 mm rms misalignment. These results are calculated with the Warp field solver and averaged for 100 cases.
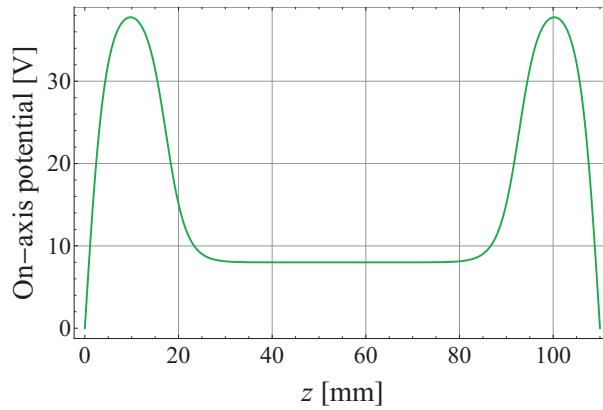
Figure 2.10: Longitudinal barrier potential in the S-POD on central axis. The result is calculated with the Warp field solver. The applied bias voltages are 40 V at the End Cap A and the Gate, and 10 V at the Section A.

Chapter 3

Numerical simulation of beams

As previously described, the multi-particle simulation is a popular method to solve the time evolution of the arbitrary distribution. In the numerical simulation, it is important that the integration method of the time evolution and the method to calculate the Coulomb interaction.

3.1   Leapfrog method and Boris method

There are many types of the numerical integration method to calculate the particle motion. For example, 4th order Runge-Kutta(rk4) method is famous for easy method. However, rk4 method is not a symplectic advance, so the particle motion overflows by the accumulation of the numerical errors. Here, the "symplectic" means the particle motion satisfies,

$$\begin{pmatrix} x_{i+1} \\ v_{i+1} \end{pmatrix} = M \begin{pmatrix} x_i \\ v_i \end{pmatrix} \quad \text{and} \quad \det M = 1. \tag{3.1}$$

The accelerator simulations require the long term calculation for the beam stability analysis. Therefore, it requires symplectic and faster method. Generally, high-order integration methods have high order numerical accuracy, but the calculation cost is trade-off of the number of the order. The leapfrog method is often used for the charged particle as a low-order method. It only needs to store prior position and velocity and one field-solve per time step.

   Figure 3.1 is the schematic of the leapfrog method. The integration cycle is,

$$\text{(i)} \quad m \frac{v_{i+1/2} - v_{i-1/2}}{\Delta t} = F_i(x),$$

$$\text{(ii)} \quad \frac{x_{i+1} - x_i}{\Delta t} = v_{i+1/2},$$

where, $\Delta t = t_i - t_{i-1}$. x and v are not evaluated at the same time, so the initial velocity v_0 should be pushed back a half cycle $v_{-1/2} = v_0 - F_0(x)\Delta t/2$ with the simple approximation.

   On the other hand, the previous leapfrog method can not use for the velocity dependent force as occurs with magnetic field. The Boris method solves this problem [22]. Assuming the electric

(a) position advance

t_0 t_1 t_2 t_3 t_4

(b) velocity advance

$t_{-1/2}$ $t_{1/2}$ $t_{3/2}$ $t_{5/2}$ $t_{7/2}$
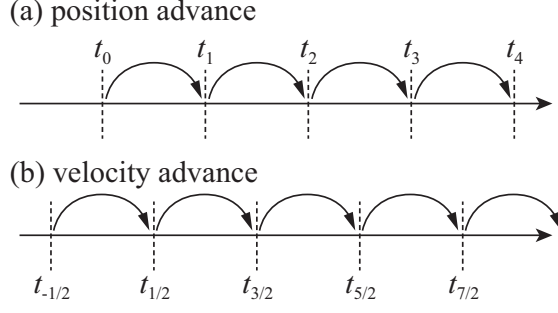
Figure 3.1: Schematic of the leapfrog method. (a) Position is evaluated at integral time steps, while (b) velocity is evaluated at half times.

field E and the magnetic field B, the force F is

$$F = q(E + v \times B).$$ (3.2)

The velocity advance is modified as following 3 steps.

$$\text{(i)} \quad v_- = v_{i-1/2} + \frac{q}{m} E \frac{\Delta t}{2},$$

$$\text{(ii)} \quad \frac{v_+ - v_-}{\Delta t} = \frac{q}{2m}(v_+ + v_-) \times B,$$

$$\text{(iii)} \quad v_{i+1/2} = v_+ + \frac{q}{m} E \frac{\Delta t}{2}.$$

3.2 PIC method

As the electric field in accelerator physics, it is important that not only the external field but also the internal field generated by the Coulomb interaction of the beam. A charged particle beam in an accelerator generally contains large number of ions. In this case, it is very expensive to calculate the Coulomb interaction of the beam, because the number of the calculation increases proportionally to the square of the number of ions. "Particle-In-Cell (PIC)" method commonly used to simulate the multi particle motion approximately. The PIC method uses "macro-particles" to represent the real particles. Generally a macro-particle takes over plural real particles.

3.2.1 Area weighting

In the PIC method, the electrical charges of the macro-particles are scattered to the mesh points in the real space. Figure 3.2 schematically shows the scattering method so called the "area weighting". Scattered charges from a macro particle on four nearest mesh points are written as
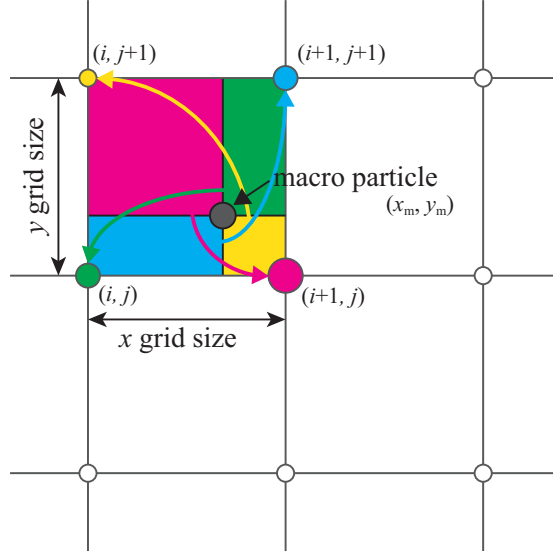
Figure 3.2: Schematic of the scattering of the macro-particle (gray circle). The charge of the macro-particle is scattered to the four nearest mesh points.

$$q_{i,j} = q_{\mathrm{m}} \frac{(x_{i+1} - x_{\mathrm{m}})(y_{i+1} - y_{\mathrm{m}})}{\Delta x \Delta y} \tag{3.3}$$

$$q_{i+1,j} = q_{\mathrm{m}} \frac{(x_{\mathrm{m}} - x_i)(y_{i+1} - y_{\mathrm{m}})}{\Delta x \Delta y} \tag{3.4}$$

$$q_{i,j+1} = q_{\mathrm{m}} \frac{(x_{i+1} - x_{\mathrm{m}})(y_{\mathrm{m}} - y_i)}{\Delta x \Delta y} \tag{3.5}$$

$$q_{i+1,j+1} = q_{\mathrm{m}} \frac{(x_{\mathrm{m}} - x_i)(y_{\mathrm{m}} - y_i)}{\Delta x \Delta y}, \tag{3.6}$$

where $x_{i,j}$, $y_{i,j}$, $q_{i,j}$ are the positions and the charges of the mesh point, x_{m}, y_{m}, q_{m} are the positions and the charges of the macro-particle. The internal electric field is calculated by the mesh points.

3.3 Computational cycle

Summarizing the above, the one step cycle of the PIC simulation is described as

(i)   Moving particles: $\boldsymbol{F} \to \boldsymbol{v} \to \boldsymbol{x}$.

(ii)   Weighting (particles to mesh point): $(\boldsymbol{x}, \boldsymbol{v}) \to (\rho, \boldsymbol{J})$.

(iii)   Field solver: $(\rho, \boldsymbol{J}) \to (\boldsymbol{E}, \boldsymbol{B})$.

(iv)   Weighting (mesh point to particles): $(\boldsymbol{E}, \boldsymbol{B}) \to \boldsymbol{F}$.

Needless to say, the step size, the grid size, and the number of the macro-particles should be set to appropriate values in the simulation.

3.4 Initial distributions

In 1D or 2D Vlasov-Poisson system, we need to define an initial distribution on a transverse phase space. Following 3 types distribution are generally used to solve the system [23].

3.4.1 Kapchinskij-Vladimirskij (KV) distribution

KV distribution is known as the only self-consistent solution. Therefore, this distribution is often used for analytical theories, but the distribution is defined by the delta function in the phase space, and so it is not realistic. The KV distribution can be expressed as

$$f(x,y,p_x,p_y;s) = \frac{N}{\pi^2 \varepsilon_x \varepsilon_y} \delta \left[\frac{x^2}{a^2} + \frac{y^2}{b^2} + \frac{(ap_x - a'x)^2}{\varepsilon_x^2} + \frac{(bp_y - b'y)^2}{\varepsilon_y^2} - 1 \right], \tag{3.7}$$

where, the symbols are the same as Eq. (2.60).

3.4.2 Waterbag distribution

Waterbag distribution has a sharp edge in a phase space. The distribution is written as

$$f(x,y,p_x,p_y) = \frac{8N}{9\pi^2 \varepsilon_x \varepsilon_y} \Theta \left\{ 1 - \frac{2}{3} \left[\frac{x^2}{a^2} + \frac{y^2}{b^2} + \frac{(ap_x - a'x)^2}{\varepsilon_x^2} + \frac{(bp_y - b'y)^2}{\varepsilon_y^2} \right] \right\}, \tag{3.8}$$

where

$$\Theta(x) = \begin{cases} 1, & x > 0, \\ 0, & x < 0. \end{cases} \tag{3.9}$$

3.4.3 Gaussian distribution

When we assume the trap or accelerator experiments, Gaussian distribution is the most realistic in these three distributions. The phase space distribution is the same as Gaussian, and

$$f(x,y,p_x,p_y) = \frac{4N}{\pi^2 \varepsilon_x \varepsilon_y} \text{Exp} \left\{ -2 \left[\frac{x^2}{a^2} + \frac{y^2}{b^2} + \frac{(ap_x - a'x)^2}{\varepsilon_x^2} + \frac{(bp_y - b'y)^2}{\varepsilon_y^2} \right] \right\}. \tag{3.10}$$

3.5 PIC simulation code "Warp"

The Warp code is originally developed for heavy ion fusion researches by David Grote [24, 25, 26, 27, 28, 29]. In this code, the main routines including particle-mover, field-solver, particle-loading, etc. are written in Fortran90. These Fortran codes are compiled with *Forthon* (Python

Grid size (x,y)	0.072 [mm]
Number of macro particles	1×10^5
Steps per cell	$200 \sim 1680$
Ion Specie	$^{40}\mathrm{Ar}^+$
Initial distribution	KV, Gaussian, Waterbag
Plasma Temperature	0.1 [eV]
Inner radius	5.00 [mm]
Rod radius	5.75 [mm],
Rf frequency	1 [MHz]

Table 3.1: 2D numerical simulation parameters for the PIC code Warp. The ion specie, the inner radius, rod radius, and the rf frequency are the same as the experimental parameters.

interface generator for Fortran based codes) as a Python-type module [30]. The Warp code works on the Python interpreter, and Python have powerful scientific module packages represented by the NumPy [31]. Using the Python interface with the NumPy, we can be easy to reproduce various situation not only of the charged-particle beam but also the confined non-neutral plasma without modifying the source code.

The code supports full 3D, *r-z* and *x-y* 2D PIC packages, and with the multi-species PIC calculation. Moreover, the self-field symmetry, the mesh refinement method, and the parallel computing system with MPI(Message Passing Interface) are equipped to reduce the calculation cost. The field solver can also solve electromagnetic field with detailed conducting object using Dirichlet, Neumann, or periodic boundary conditions. The diagnostics are outputted as CGM (Computer Graphics Metafiles) with the scientific graphics library; *Gist* by default, but of course, we can also use other Python graphics library like *matplotlib* [32].

The Warp code is continuously and extensively extended, and the source code and the documentation of the Warp is provided in Ref. [29].

We generally use the Warp code for the 2D multi-particle simulation in the S-POD system, because systematic 3D simulation requires large computational resources, and as we mentioned above, uniform longitudinal distribution are produced in the middle of confinement area in the trap. Table 3.1 is the typical Warp simulation parameters. These numerical parameters are chosen for converging in the simulation results which studies in old works [33]. The steps per cell is used various numbers for various focusing systems with converging the statical values. Figure 3.3 shows a simulation area and the confined plasma. The Warp code provides the multi-grid field solver not only for a space-charge but also conductors. About a square of 20 mm on each side is chosen for the simulation area, and the side boundary conditions are Dirichlet.

In the 2D (transverse) Warp simulations, the initial "pseudo-equilibrium" distribution matched to the periodic focusing channel is formed by canonically transforming a root-mean-squared (rms) equivalent thermal equilibrium distribution which is constructed under the smooth approximation [23]. Figure 3.4 is a Warp simulation example. The emittance growth is defined by $(\varepsilon_x(s) + \varepsilon_y(s))/(\varepsilon_x^{\mathrm{ini}} + \varepsilon_y^{\mathrm{ini}})$. There is no emittance growth for 100 periods in the stable operating point
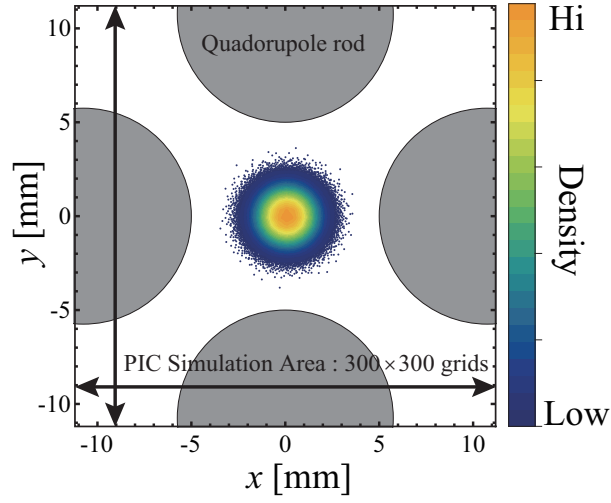
Figure 3.3: Simulation area in the cross section of the trap.
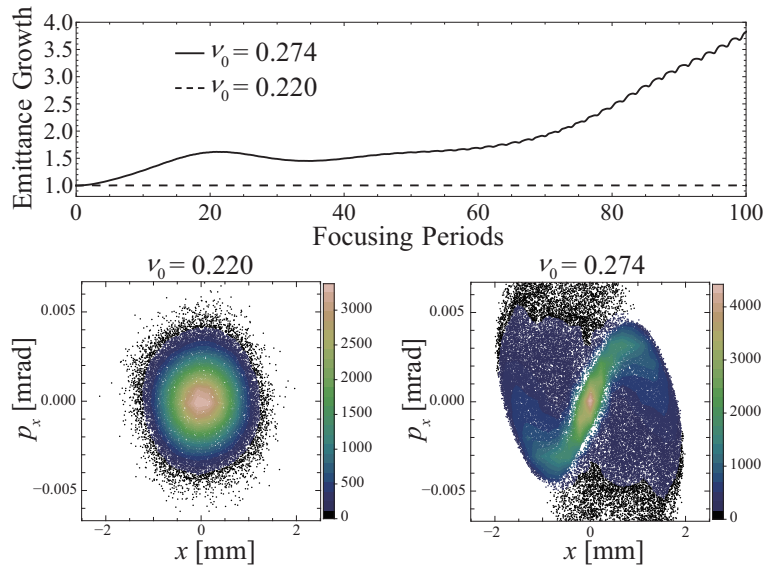
Figure 3.4: An example of the 2D slice Warp simulation in two operating points ($\nu_0 = 0.22$:dashed line and $\nu_0 = 0.274$:solid line). The tune depression η is 0.90 for both operating point. The initial distribution is pseudo-equilibrium Gaussian matched to the periodic focusing system. Upper panel shows the emittance growth histories. Lower left panel is the final phase space distribution at the stable operating point ($\nu_0 = 0.22$). Lower right panel is at the unstable operating point ($\nu_0 = 0.274$), and the phase space distribution is blown up widely.

(an example $\nu_0 = 0.22$). However, the emittance growth becomes larger in the unstable operating point (an example $\nu_0 = 0.274$). To repeat these simulations for the wide range of bare tunes, we can obtain the "stop band" which shows the unstable tune region.

Chapter 4

Collective resonance

With a beam cooling or a beam densification in an accelerator, particles in a beam are connected each other by a Coulomb interaction (space-charge effect), and a charged particle beam have a "collective motion". In addition the Coulomb repulsive forces make weaker the effective focusing force from the external field to the beam. In addition, a particle motion in a periodic focusing system has resonance conditions which rely on a tune, so the resonance conditions are changeable by the space-charge effect. We describe the collective resonance condition by theoretically and numerically in this chapter.

4.1 Resonance conditions

4.1.1 Resonances in the absence of space charge

At the beginning, assuming the space charge effect is negligible, the resonance condition is the same single particle theory [7]. It returns to the simple parametric resonance, so the resonance condition in zero-space-charge limit becomes

$$\Omega_k = k\nu_0 = n, \tag{4.1}$$

where Ω_k is the coherent tune of mode number k, and n is an integer. When the coherent tune satisfies the resonance condition, the beam becomes unstable.

4.1.2 Linearized Vlasov approach

As mentioned in 2.3.1, the arbitrary Vlasov-Poisson model is hard to solve analytically for the time evolution of the beam distribution. Therefore, the perturbation approach so called "linearized Vlasov analysis" is employed to study collective resonances [11, 15, 34]. In the linearized Vlasov analysis, we solve the evolution of the perturbation distribution instead of the whole distribution. Assuming the equilibrium state distribution function f_0 and the perturbation distribution function

δf, the Vlasov-Poisson equations are described as

$$\frac{\partial f_0}{\partial s} + \frac{\partial \delta f}{\partial s} + [f_0, H_0] + [\delta f, H_0] - \frac{q}{p_0 \beta_0 c \gamma_0^2} ([\delta \phi^{sc}, f_0] + [\delta \phi^{sc}, \delta f]) = 0, \qquad (4.2)$$

and

$$\Delta \phi_0^{sc} + \Delta \phi^{sc} = -\frac{1}{\varepsilon_0} \int f_0 dp_x dp_y - \frac{1}{\varepsilon_0} \int \delta f dp_x dp_y. \qquad (4.3)$$

Here, H_0 is the equilibrium-state Hamiltonian, and it satisfies the following zero-th order Vlasov-Poisson equations,

$$\frac{\partial f_0}{\partial s} + [f_0, H_0] = 0, \qquad (4.4)$$

$$\Delta \phi_0^{sc} = -\frac{q}{\varepsilon_0} \int f_0 dp_x dp_y. \qquad (4.5)$$

Disregarding all terms of δ^2 and higher orders, the linearized Vlasov-Poisson equations are derived from above four equations,

$$\frac{\partial \delta f}{\partial s} + [\delta f, H_0] = \frac{q}{p_0 \beta_0 c \gamma_0^2} [\delta \phi^{sc}, f_0], \qquad (4.6)$$

$$\Delta \delta \phi_0^{sc} = -\frac{q}{\varepsilon_0} \int \delta f dp_x dp_y. \qquad (4.7)$$

In this analysis, derive the equilibrium state from Eq. (4.4) and (4.5) firstly. As we know, only cognize self-consistent equilibrium solution as the KV distribution. After that, substitute these results for Eq. (4.6) and (4.7). In the case of diverging the perturbation term after one period, the state can be said as unstable.

4.1.3   One-dimensional Vlasov theory

One-dimensional analytic study of space-charge dominated beams was established by Sacherer over 40 years ago [18]. His study has attracted more attention in the modern high-power accelerator design studies. The resonance condition is derived by a Vlasov dispersion relation assuming a sheet beam with an uniform charge density, and shown as

$$\Omega_k = k(\nu_0 - C_k \Delta \nu) \approx n. \qquad (4.8)$$

Here, $\Delta \nu$ is the incoherent tune shift by the space-charge effect, and C_k is a positive constant less than 1. Sacherer predict that in his study, $C_1 = 0$, $C_2 = 0.75$, $C_3 = 0.88$, and $C_4 = 0.92$. Subsequent study, the more detailed analytic description is derived from the linearized Vlasov approach with the perturbed system [35]. In this work, the resonance condition is written as

$$\Omega_k = k(\nu_0 - \hat{C}_k \Delta \nu) \approx \frac{n}{2}. \qquad (4.9)$$

34

Here, $\hat{C}_k$ is similar to Sacherer's C_k, but $\hat{C}_1 = 0.15$, $\hat{C}_2 = 0.83$, $\hat{C}_3 = 0.93$, and $\hat{C}_4 = 0.96$ are given. The resonance condition Eq. (4.9) shows the linear resonance ($k = 2$) occurs in near the quarter integer tunes. In addition, the growth rate of this linear-quarter integer resonance gets higher according as the tune depression close to zero.

4.1.4 Two-dimensional Vlasov analysis

Two-dimensional analysis is also derived from the linearized Vlasov approach, and it is solved numerically [11]. Assuming the periodic focusing and KV distribution, the total Hamiltonian with the perturbation potential is written as

$$H = \frac{1}{2}(p_x^2 + p_y^2) + \frac{1}{2}(\kappa_x(s)x^2 + \kappa_y(s)y^2) + \Phi, \tag{4.10}$$

where

$$\kappa_x = K_x - \frac{Q}{a(a+b)}, \quad \kappa_y = K_y - \frac{Q}{b(a+b)}. \tag{4.11}$$

$K_{x,y}(s)$ are the external periodic focusing force. and the beam envelopes $a(s)$ and $b(s)$ are determined by the envelope equations Eq. (2.70). The perturbation potential Φ can be described as

$$\Phi = \frac{4\pi q}{m\gamma_0^3(\beta_0 c)^2}\delta V, \tag{4.12}$$

where δV is the electrostatic potential function due to perturbations. Using the Courant-Snyder invariants $\alpha(s)$ and $\beta(s)$, and the generating function for the Hamiltonian Eq. (4.10),

$$F = \frac{x}{\beta_x^{1/2}}\left(\overline{p_x} - \frac{\alpha_x}{2}\frac{x}{\beta_x^{1/2}}\right) + \frac{y}{\beta_y^{1/2}}\left(\overline{p_y} - \frac{\alpha_y}{2}\frac{y}{\beta_y^{1/2}}\right). \tag{4.13}$$

Here, make use of the scaling transformation $\tilde{x} = \overline{x}/\sqrt{\varepsilon}$, $\tilde{p}_x = \overline{p}_x/\sqrt{\varepsilon}$, and the canonical variables are written as

$$\tilde{x} = \frac{x}{(\beta_x\varepsilon)^{1/2}}, \quad \tilde{p}_x = \left(\frac{\beta_x}{\varepsilon}\right)^{1/2}\left(p_x + \frac{\alpha_x}{\beta_x}x\right) \tag{4.14}$$

where similarly for $\tilde{y}$ and $\tilde{p}_y$. Consequently, the new Hamiltonian is expressed as

$$\tilde{H} = \frac{1}{2\beta_x}(\tilde{p}_x{}^2 + \tilde{x}^2) + \frac{1}{2\beta_y}(\tilde{p}_y{}^2 + \tilde{y}^2) + \frac{1}{\varepsilon}\Phi. \tag{4.15}$$

Now we assume the KV distribution, the infinitely distant self-potential as zero, and the perturbation potential Φ in the inside of the beam satisfies Poisson equation,

$$\nabla\Phi \equiv \frac{1}{a^2}\frac{\partial^2\Phi}{\partial x^2} + \frac{1}{b^2}\frac{\partial^2\Phi}{\partial y^2} \tag{4.16}$$

$$= \frac{Q}{\pi\varepsilon ab}\int^s ds' \left(\frac{\partial}{\partial\Psi'_x} + \frac{\partial}{\partial\Psi'_y}\right)\left[\frac{d}{d(p^2)}\int_0^{2\pi} d\theta\Phi(x',y';s)\right]\Bigg|_{p^2=1-x^2-y^2}. \tag{4.17}$$

Here, $\Psi_{x,y}$ are the phase advance of the beam. We apply elliptic coordinates (ξ,ζ) for the real space, and obtain

$$x = \frac{h}{a}\cosh\xi\cos\zeta \quad\text{and}\quad \frac{h}{b}y = \frac{h}{b}\sinh\xi\sin\zeta \tag{4.18}$$

where $h^2 = a^2 - b^2$, in addition, $\cosh\xi = a/h$ and $\sinh\xi = b/h$ at the boundary of the beam surface $x^2 + y^2 = 1$. The discontinuity of the self-potential field at the beam boundary can be written as

$$\Delta\frac{\partial\Phi}{\partial\xi} = \frac{Q}{\varepsilon}\int^s ds'\left(\frac{\partial}{\partial\Psi'_x} + \frac{\partial}{\partial\Psi'_y}\right)\Phi(\cos\zeta\cos(\Psi'_x - \Psi_x), \sin\zeta\sin(\Psi'_y - \Psi_y); s') \tag{4.19}$$

$\Delta\partial\Phi/\partial\xi$ in Eq. (4.19) is the gap of the self-potential at the beam surface between the perturbation potential inside the beam and the perturbation potential outside the beam which satisfies Laplace equation,

$$\frac{\partial^2\Phi}{\partial\xi^2} + \frac{\partial^2\Phi}{\partial\zeta^2} = 0. \tag{4.20}$$

When we obtain the perturbation potential which satisfies Eq. (4.16) and (4.19), it equals to obtain the self-consistent solution of the linearized Vlasov-Poisson equations.

As a general solution, we assume a perturbation potential can develop as

$$\Phi_n = \sum_{i=0}^{\infty}\sum_{m=0}^{n-2i} A_m^{(i)}(s)x^{n-m-2k}y^m. \tag{4.21}$$

Here, n is the mode order of the perturbation potential. m shows the normal and the skew component of the potential. An even m is the normal and an odd m is the skew. Now we define the variable for k-th mode perturbation vibration I as

$$I_{k;j,l} = \int^s A_k(s')\sin[j(\Psi'_x - \Psi_x) + l(\Psi'_y - \Psi_y)]. \tag{4.22}$$

Equation (4.16) and (4.19) are rewritten by I, and it satisfies,

$$D_{j,l}(s)\frac{d}{ds}\left(D_{j,l}(s)\frac{dI}{ds}\right) + I = -D_{j,l}(s)A_i, \tag{4.23}$$
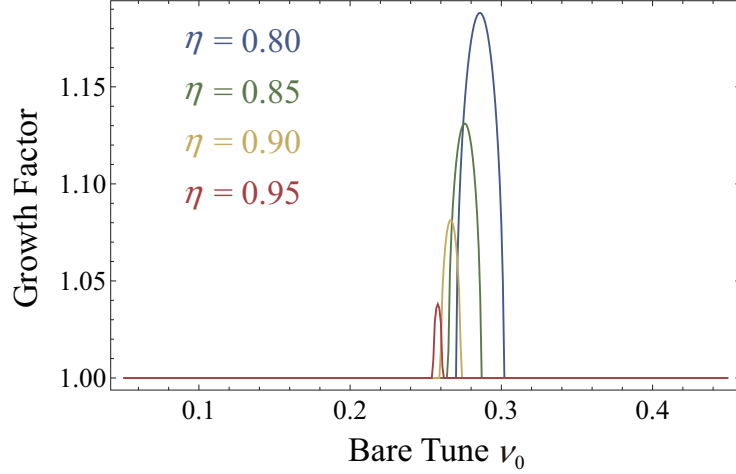
Figure 4.1: Stop band of the growth factor of $k = 2$ in the rf focusing system. By the tune depression, the peak tune of the growth factor is shifted and the peak value becomes larger.

where

$$D_{j,l} = \left(\frac{j}{\beta_x} + \frac{l}{\beta_y} \right)^{-1} \tag{4.24}$$

A_i can be represented by the polynomial expression of I, Eq (4.24) becomes a second-order differential equation in terms of I. Therefore, we can get the transfer matrix for I by the numerical integrations through one period of the cell. The transfer matrix M is written as

$$\boldsymbol{I}(s_0 + L) = M\boldsymbol{I}(s_0), \quad \boldsymbol{I} = (I_1, I'_1, I_2, I'_2, ...). \tag{4.25}$$

Solving the eigenvalue of the matrix, we obtain the stability of the perturbation vibration and the growth factor of the beam. Figure shows second-order ($k = 2$) growth factor for various bare tunes in the rf focusing system. In the case of tune depression $\eta \neq 1$, the growth factor becomes larger than one near the quarter integer tune. In addition, the peak tune of the growth factor moves to left side. These results are consistent to the resonance condition Eq. (4.9).

4.2 Lattice-dependence of resonance instability bands (stop bands)

4.2.1 Sinusoidal focusing lattice

Figure 4.2 shows the stop band of the emittance growth by the 2D Warp simulations. The initial distributions are set up to KV (a), Gaussian (thermal-equilibrium) (b), and water bag (c), for each tune depressions ($\eta = 0.80 \sim 0.95$). The emittance growth is defined as $(\varepsilon_x^{\text{fin}} + \varepsilon_y^{\text{fin}})/(\varepsilon_x^{\text{ini}} + \varepsilon_y^{\text{ini}})$, and $\varepsilon_{x,y}^{\text{fin}}$ is the rms emittance after 100 periods. In the each case, we can find three resonance regions which are $\nu_0 \approx 1/6$, $1/4$ and $1/3$. The largest peak near $\nu_0 = 1/4$ is generated mainly by the instability of the second-order linear collective mode, and the other two peaks near $\nu_0 = 1/6$

37
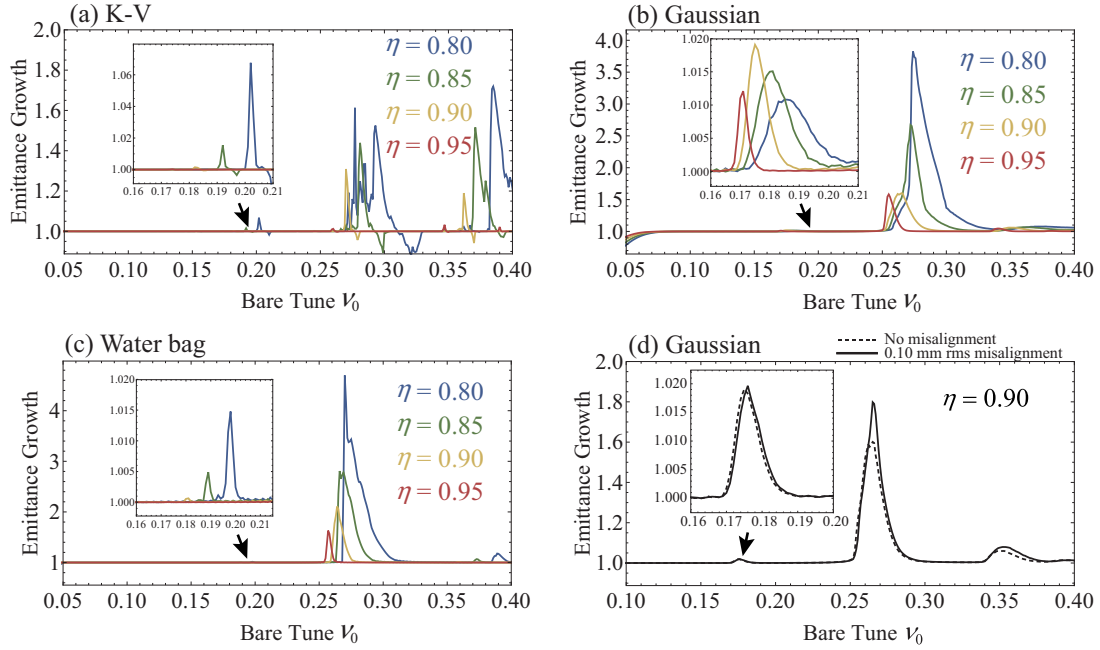
Figure 4.2: Stop band of the each distribution and the effect from the electrodes misalignment. (a) K-V, (b) thermal equilibrium (Gaussian base), (c) Water bag, (d) thermal equilibrium, no misalignment (solid line), and 0.10 mm rms misalignment (dashed line).

and $1/3$ are due to third-order nonlinear resonances. These results are consistent to the previous analytical theory Eq. (4.9). The resonance widths in KV and waterbag results are narrower than the Gaussian result, because the Gaussian distribute widely in the phase space, so the frequencies of the particles spread widely. In the case of Gaussian and waterbag, the linear resonance peak located left side from the center of the resonance region. The reason is the space-charge effect becomes weaker by the real-space beam spread on the resonance, and so the tune shift is reduced. As a result, the resonance condition Eq. (4.9) moves to low tune side.

Since this, we use the initial Gaussian distribution for the Warp simulation in the view of the experiments. Figure 4.2 (d) shows the misalignment effect (see Fig. 2.9) in the tune depression $\eta = 0.90$. Comparing from the no misalignment case (dashed line), the peak values of the growth factors near $v_0 = 1/4$ and $1/3$ are increased about $10 \sim 20$ % in 0.1 mm rms misalignment case. These are result of increasing the external third- and fourth-order nonlinear fields.

The time evolutions of the emittance growth in the resonance regions are shown in Fig. 4.3 ($v_0 \approx 1/4$:(a),(c) and $1/3$:(b),(d)). (a) and (b) are the tune depression $\eta = 0.90$, (c) and (d) are the tune depression $\eta = 0.95$, and plotted for 1000 periods. In the linear resonance region near $v_0 = 1/4$;(a) and (c), the time evolution of the emittance growth is slow, and the emittance stops after about 300 periods;(a) or about 700 periods;(c). These phenomena come from the space-charge dependence of the collective-instability growth factor, and the tune depression close to one due to the beam spread in the real space by the resonance instability. On the other hand, the time evolution by third order resonance near $v_0 = 1/3$;(b) and (d) is very quickly and then the emittance

38
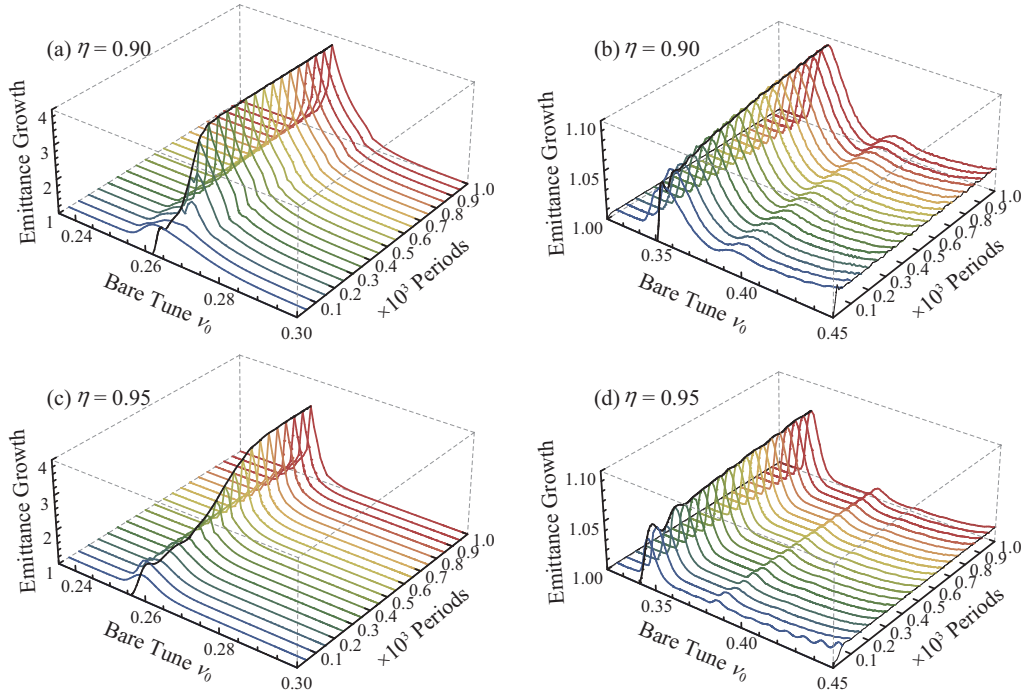
Figure 4.3: Time evolution of the stop band (thermal equilibrium distribution). (a) $\eta = 0.90$ 2nd order resonance region, (b) $\eta = 0.90$ 3rd order resonance region, (c) $\eta = 0.95$ 2nd order resonance region, (d) $\eta = 0.95$ 3rd order resonance region.

grows gently for the long over 1000 periods. This third order resonance does not depend on the space charge and always exist because of Eq. 4.1.

Comparison between the simulation results and the experimental results

The experimental results by the S-POD are shown in Fig. 4.4 upper panel. Here, N_{in} is the initial ion number which confined in the trap. We can recognize three the ion loss peaks like reversal of the simulation peaks. The experimental resonance peaks also shifted to lower tune side, and this is the same reason as the simulation results. Comparing the resonance region between these results, we can estimate the tune depression in the experiments, therefore $N_{in} \approx 1 \times 10^7$ corresponds to $\eta \approx 0.85$ and $N_{in} \approx 1 \times 10^6$ is to $\eta \approx 0.95$. The ion loss in third-order resonance is quite large, because there is a possibility of the large third order component due to the rod misalignment including the centroid shift in the confinement section of the trap system.

4.2.2 Doublet focusing lattice

The sinusoidal (rf) wave is practically easy to generate in the trap system, but the real accelerator is configured by the axial separated components. Therefore the focusing function is simply represented as like a step function in Fig. 4.5. The most standard strong focusing system is the
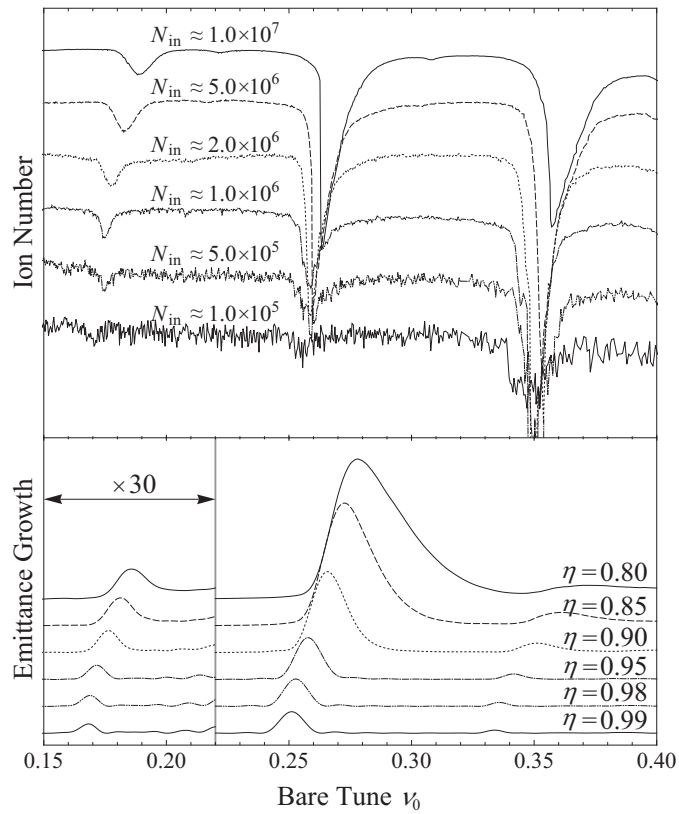
Figure 4.4: Comparison between the numerical stop band and the experimental stop band. Upper panel is the experimental stop bands which are shown by the ion loss in the trap. N_{in} is the initial ion number in the trap. Lower panel is the Warp simulation result for six tune depressions.
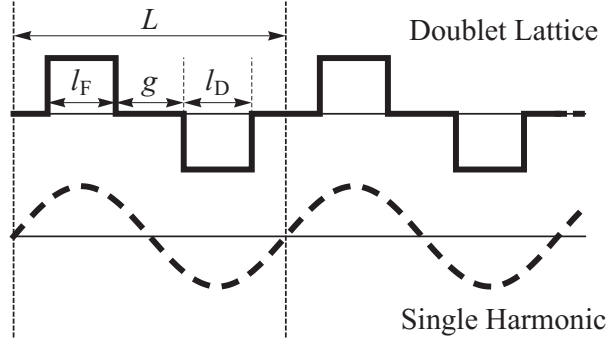
Figure 4.5: The doublet focusing lattice (upper figure) and the main Fourier harmonic.

so-called "doublet lattice" in which the beam receives one linear focusing and one defocusing quadrupole kick alternately within the lattice period. A special case of the doublet lattice with equal length of focusing and defocusing quadrupoles axially spaced equidistantly within the lattice cell is called a "FODO" lattice. FODO lattices make the most efficient use of the quadrupole focusing strength, but have short free axial drift space within the lattice for other uses (pumping, diagnostics, etc). Due to high focusing efficiency, quadrupole doublets are often adopted for beam transport channels and linear accelerators.

Figure 4.5 also shows the geometric parameter for the doublet lattice. Here, l_F and l_D are the width of focusing and defocusing pulses. The amplitudes of the focusing pulse is the same as defocusing pulse. The gap width is denoted as g, and the one lattice length as L. Using these parameters, we define the two characteristic factors for later convenience,

$$F_f = \frac{l_F + l_D}{L} \in [0,1], \tag{4.26}$$

$$D_r = \frac{g}{L - g - l_F - l_D} \in [0,1]. \tag{4.27}$$

Filling factor F_f measures the occupancy of the quadrupole magnets, and Drift ratio D_r measures the asymmetry of the gaps in the doublet lattice. $D_r = 1$ corresponds to a symmetric FODO lattice. Expanding the doublet lattice waveform into Fourier series

$$\hat{K}(\tau) = \sum_{n=1}^{\infty} A_n \sin(2\pi\tau/L + \alpha_n), \tag{4.28}$$

where A_n and α_n are the amplitude and phase of n-th Fourier harmonic. Figure 4.6 shows the $n-th$ order Fourier coefficient A_n for various filling factors F_f and drift ratios D_r. We can find the even order coefficients evaluate to zero in the case of $D_r = 1$, and there are multiple lines which the coefficients to be zero.
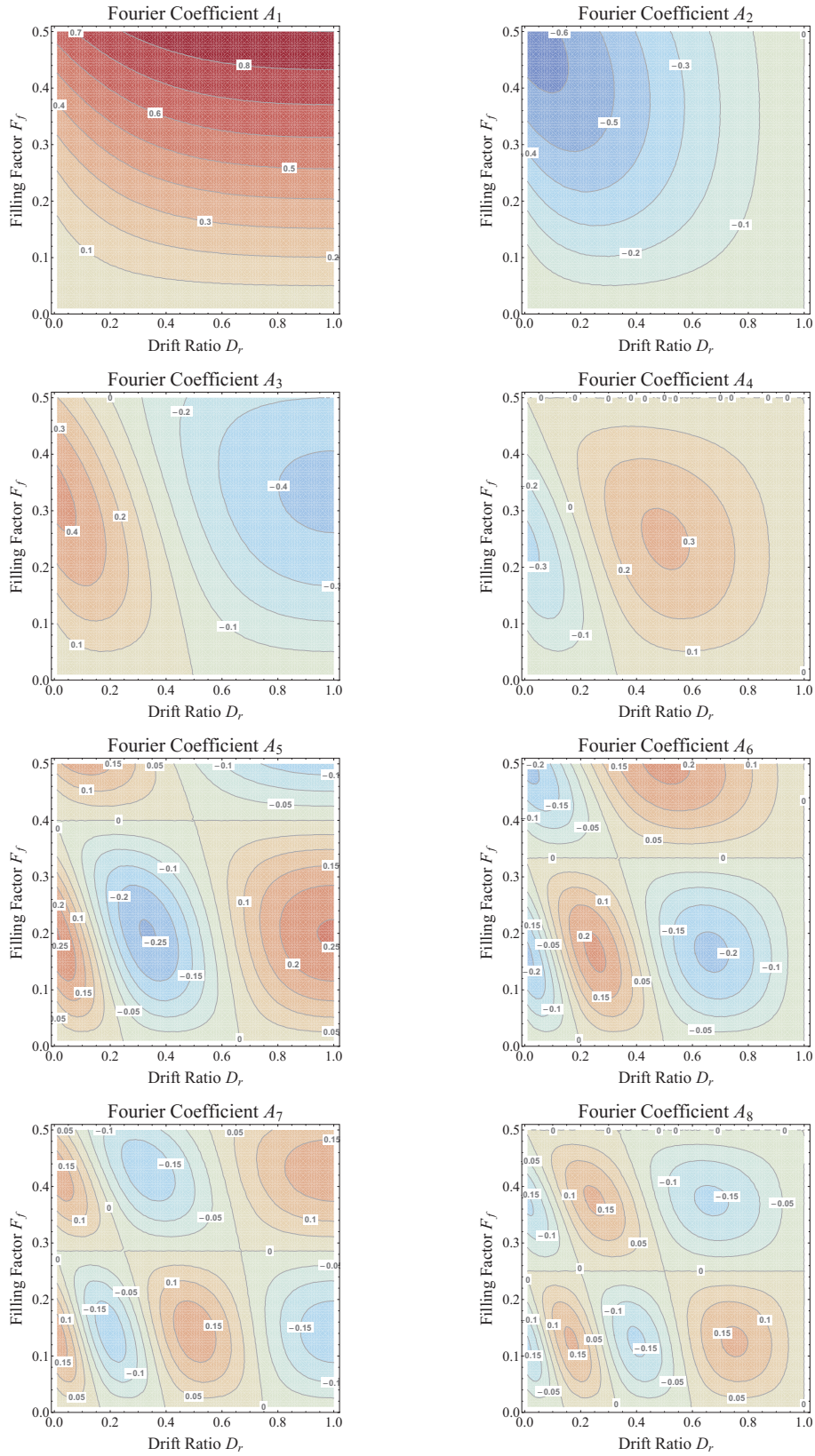
Figure 4.6: FFT result of the filling factor F_f and the drift ratio D_r dependence of the Fourier coefficient A_n ($n = 1 \sim 8$). Contours show the $n-th$ order amplitude of the Fourier harmonic. A_1 is the main harmonic wave and others are high order frequency coefficients.
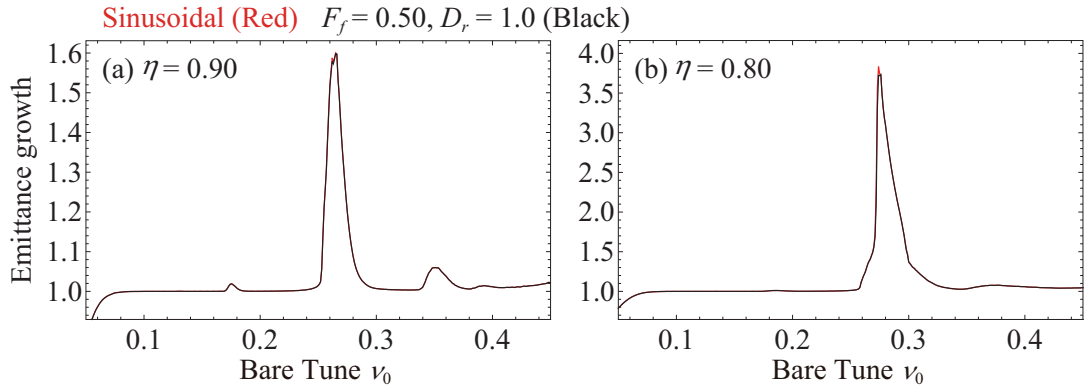
Figure 4.7: Warp simulation results corresponding to FODO (black) and single harmonic(rf, red) focusing system. An initial pseudo-equilibrium distribution with thermal equilibrium form and an rms equivalent beam tune depression η of 0.9 (a) or 0.8 (b) is loaded for all values of ν_0. The two results overlap in whole tune area.

FODO lattice and sinusoidal (rf) lattice

Figure 4.7 shows the Warp simulation result assuming FODO lattice and sinusoidal lattice. The emittance growth is defined as the rms emittance after 100 periods divided by the initial value. The tune depression is 0.9 in Fig. 4.7 (a) and 0.8 in (b). In both of them, the stop bands overlap in whole tune area. We can recognize the three resonance instability region ($\nu_0 \approx 1/6, 1/4, 1/3$) which mentioned above in the FODO lattice case.

Doublet lattice and four harmonics lattice

Figure 4.8 is the same condition as Fig. 4.7, but add the results of an approximate doublet composed from the first four Fourier components ($n \sim 1, 3, 5, 7$) in blue line. The approximate doublet result of the beta functions also overlap with each other in Fig. 4.8(b).

Next, we change both of the filling factor and drift ratio to $F_f = 0.25$ and $D_r = 0.1$, and keep the other numerical conditions. Figure 4.9 shows the three focusing waveforms corresponding to these parameters. The blue curve consists of the four Fourier components with the harmonic number $n = 1, 2, 3$, and 4; unlike the previous example in Fig. 4.8, the even harmonics are allowed due to the doublet being asymmetrical with $D_r = 0.1$. Corresponding beta functions and Warp simulation results are given in Fig. 4.9 (b) and (c). Although the three curves do not overlap, we can observe the three instability region near $\nu_0 \approx 1/6, 1/4$, and $1/3$ in all cases.

These results shows, it is reasonable that taking Fourier harmonics to assume these doublet lattice in the accelerator transport system.

Various combinations of filling factor and drift ratio

Figure 4.10 shows the result of three filling factors $F_f = 0.25, 0.50$, and 0.75 with the fixed drift ratio $D_r = 1$. Panel (a) shows the focusing system, (b) is the typical beta function, (c) is the
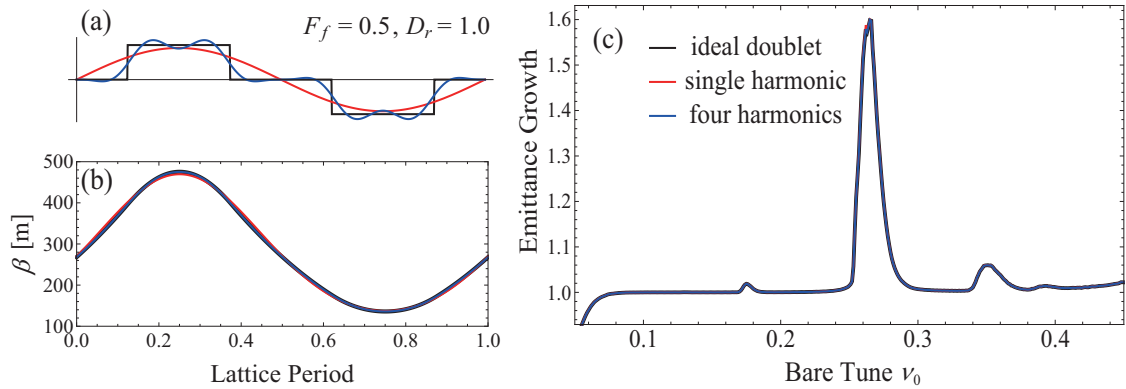
Figure 4.8: Warp simulation results corresponding to three different FODO wave forms with the initial tune depression η of 0.9. The three curves in (a) illustrate the linear focusing function and (b) plotted typical beta function for a lattice period considered in this example: the ideal piecewise constant doublet with $F_f = 0.5$ and $D_r = 1.0$ (black), a single sinusoidal harmonic (red), and an approximate doublet (blue) composed from the first four Fourier components ($n \sim 1, 3, 5, 7$). The three results almost overlap with each other.
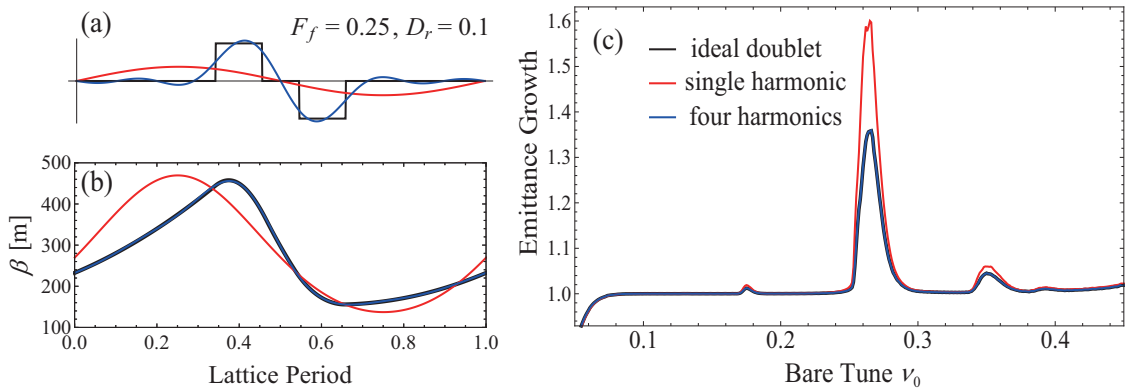
Figure 4.9: Warp simulation results corresponding to $F_f = 0.25$ and $D_r = 0.1$ and the tune depression is 0.9. The ideal doublet result (black) and the four Fourier components result (blue) overlap with each other.

Warp simulations for the tune depression $\eta = 0.90$ and 0.80, (d) is the second-order linearized Vlasov analyses, and (e) is the third-order linearized Vlasov analyses. The stop band results almost overlap ,and so there are no high dependence on the filling factor with the symmetric lattice ($D_r = 1$).

Figure 4.11 is the result of three filling factors $F_f = 0.25$, 0.50, and 0.75 with the fixed drift ratio $D_r = 0.1$. In the case of filling factor $F_f = 0.25$, the peak value of the emittance growth near $\nu_0 \approx 1/4$ is reduced. In addition, the reduction also occurs in the linearized Vlasov analyses.

Figure 4.12 is the result of three drift ratios $D_r = 0.0$, 0.1, and 0.5 with the fixed filling factor $F_f = 0.25$. In these cases, the reduction of the peak value of the emittance growth near $\nu_0 \approx 1/4$ depends on the drift ratio. However, the positions of the three resonance instability are the same

in every case. When the peak reduction occurs, we can find the small side bands in the results of linear Vlasov analysis. Therefore, We predict these reduction comes from the mode separation to the breathing mode and the quadrupole mode in the second-order resonance [36].

Figure 4.13 shows the experimental result of various filling factors and drift ratios. The resonance instability regions are the same as the simulation results which shown in above. The simulation results predict emittance growth in similar parametric regions where an envelope analysis predicts linear instability. However, these simulation and theory predictions cannot be verified from the experimental measurements in Fig. 4.13.

4.2.3 FFDD focusing lattice

The FFDD lattice is composed by two consecutive focusings and defocusings shown in Fig. 4.14 (a). (c) is typical beta functions of the horizontal and the vertical. The black solid line in Fig. 4.14 (b) shows the stop bands the Warp simulation results of the emittance growth in the FFDD lattice. The third order resonance peak near $\nu_0 \approx 1/3$ is larger than sinusoidal lattice peak. This difference comes from the envelope size of the beam in the FFDD lattice due to the third order nonlinear instability depends on the its amplitude. Figure 4.14 (d) shows the results of the trap experiments. There are three loss bands which are the same as the doublet results.

4.2.4 Triplet focusing lattice

The triplet lattice is composed by two defocusings and one focusing shown in Fig. 4.15 (a). (b) is the typical beta functions of the horizontal and the vertical. In the triplet lattice, the horizontal bare tune ν_{0x} and the vertical bare tune ν_{0x} no longer take the same value. Figure. 4.15 (b) shows the operating line in the tune diagram. The grid lines are $\nu_{0x,0y} = 1/6$, $1/4$, and $1/3$. The Warp simulation results are in Fig. 4.15 (d). The resonance instabilities rise at the intersection points of the operating line and the resonance gird lines in the tune diagram. Therefore, the resonance instability regions can estimate from Eq. (4.9) as with the previous lattices.

Figure 4.16 shows the experimental results in the triplet lattice system. We can find the resonance instability regions which appear in the same region as the simulation result in Fig. 4.15.

4.2.5 Other complex lattices

An accelerator is composed by several lattice periods. Figure 4.17 is the schematics of the periodic structure in the accelerator. The number of the lattice periods around the ring is so called the "super-periodicity" and denotes N_{sp}. Design tune around the ring is defined as N_{sp} times one lattice tune

$$\nu_0^{\mathrm{ring}} \quad = \quad \oint^{\mathrm{ring}} \frac{1}{\beta(s)} ds \tag{4.29}$$

$$= \quad N_{\mathrm{sp}} \times \oint^{\mathrm{lattice}} \frac{1}{\beta(s)} ds \tag{4.30}$$

$$= \quad N_{\mathrm{sp}} \times \nu_0^{\mathrm{lattice}}. \tag{4.31}$$
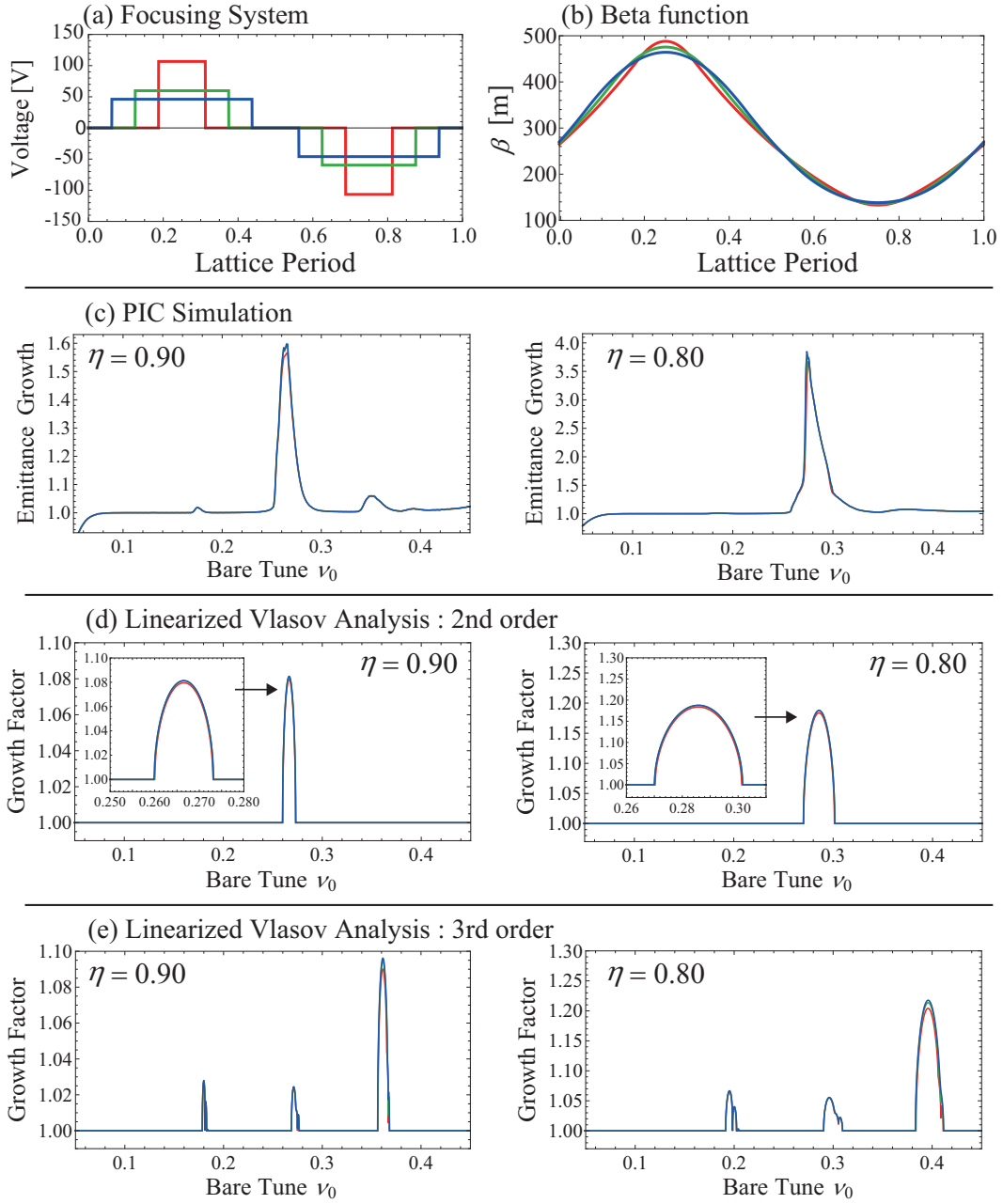
Figure 4.10: Simulation results fixed $D_r = 1.0$. $F_f = 0.25$ (red), $F_f = 0.50$ (green), $F_f = 0.75$ (blue). (a) Focusing systems. (b) Typical beta functions. (c) Stop band by the emittance growth in Warp simulations. (d),(e) 2nd and 3rd order Linearized Vlasov analysis.
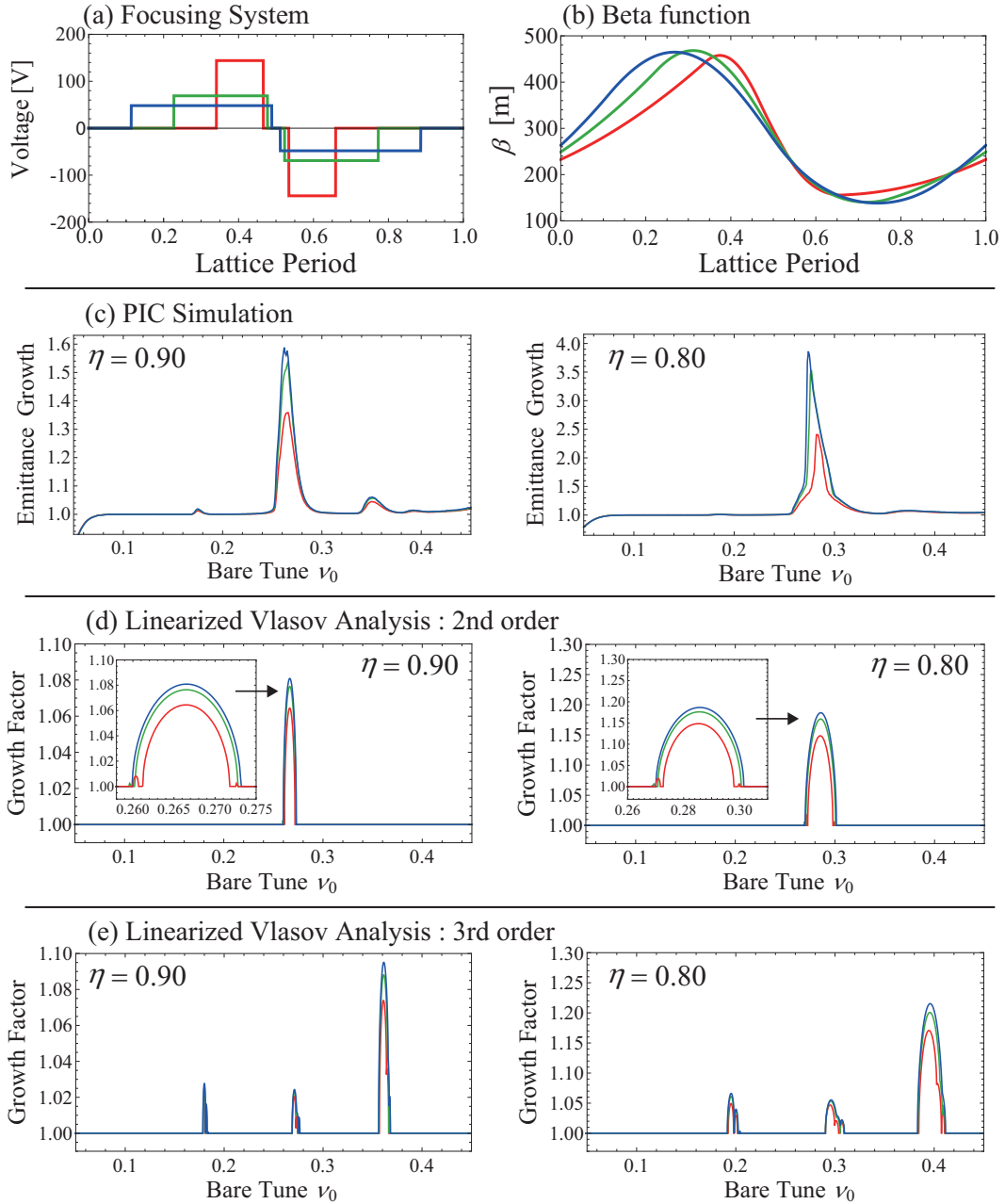
Figure 4.11: Simulation results fixed $D_r = 0.1$. $F_f = 0.25$ (red), $F_f = 0.50$ (green), $F_f = 0.75$ (blue). (a) Focusing systems. (b) Typical beta functions. (c) Stop band by the emittance growth in Warp simulations. (d),(e) 2nd and 3rd order Linearized Vlasov analysis.
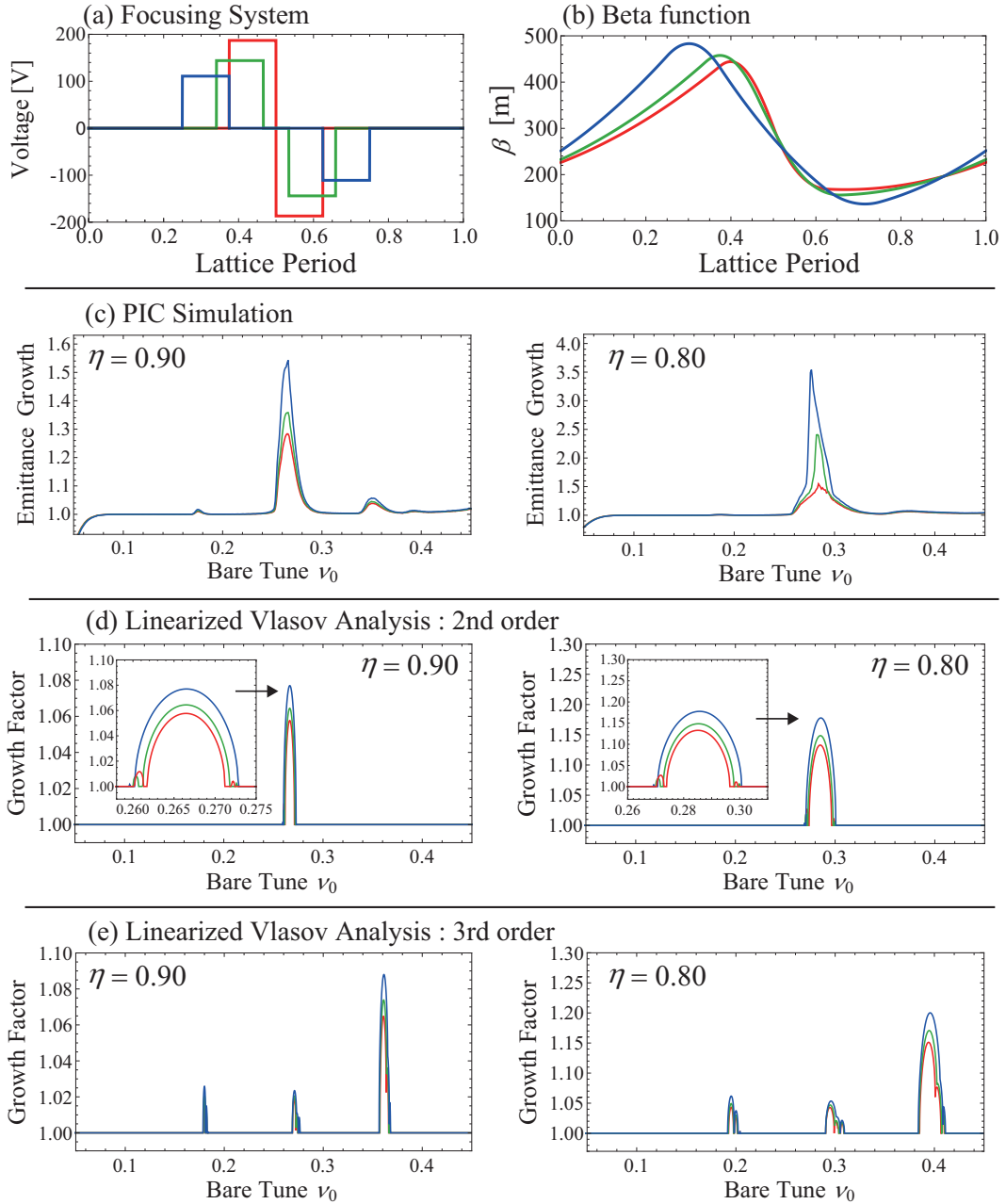
Figure 4.12: Simulation results fixed $F_f = 0.25$. $D_r = 0.0$ (red), $D_r = 0.1$ (green), $D_r = 0.5$ (blue). (a) Focusing systems. (b) Typical beta functions. (c) Stop band by the emittance growth in Warp simulations. (d),(e) 2nd and 3rd order Linearized Vlasov analysis.
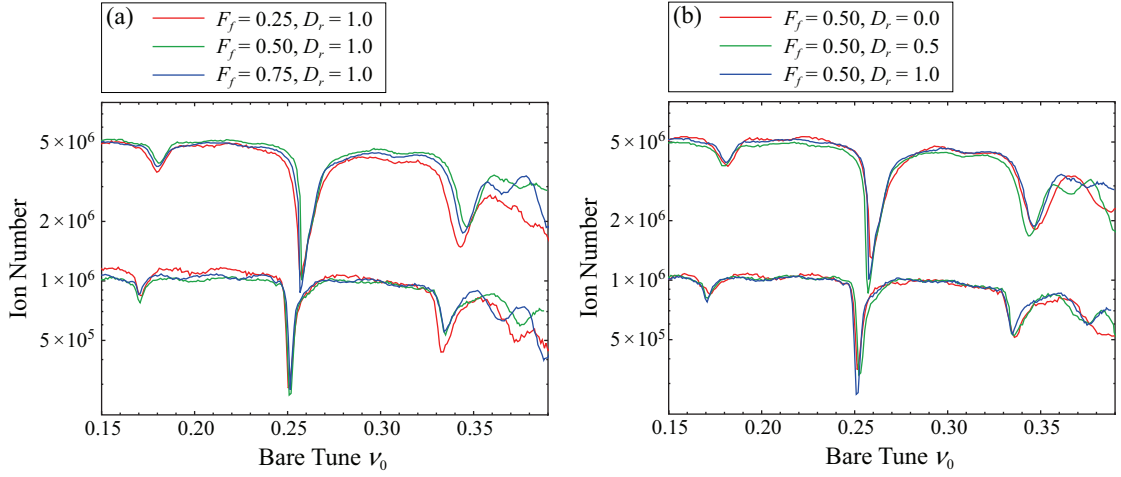
Figure 4.13: Results of the doublet lattice experiments. The ordinates of the panels are the number of Ar^+ ions surviving after a 10 ms storage (10^4 periods) at a fixed bare tune. Panel (a) is the stop band by the ion losses with fixed drift ratio. Panel (b) is the stop band with fixed filling factor. The initial number of Ar^+ ions is $N_{in} \approx 1.0 \times 10^6$ (lower curves) or $N_{in} \approx 5.0 \times 10^6$ (upper curves). We can confirm the three loss bands induced mainly by second and third-order resonances.

In addition the collective resonance condition (4.9) is rewritten as

$$\Omega_k = k(\nu_0 - \hat{C}_k \Delta \nu) \approx N_{sp} \frac{n}{2}. \tag{4.32}$$

However, a lattice symmetry breaking is inevitable in real accelerators by the electromagnetic field error, misalignment, etc. Therefore, the exact super-periodicity must be 1, and so the periodic structure closes around the ring. When the symmetry breaking is small enough, the resonance instability caused by the errors are negligible, but the large symmetry breaking exist in the ring, the new resonance instability regions appear in the stop band. In the S-POD system, the lattice structure and the lattice symmetry breaking are reproduce by superposing the low frequency rf wave. Figure 4.18 shows the primary focusing wave (a), the lattice-induced wave (b), and the error-induced wave(c). The size of the lattice symmetry breaking effect is corresponds to the amplitude of the perturbation waves.

EMMA like 42 doublets ring

As an example of a ring, we pick up 42 doublets ring like EMMA (see chapter 5)[37]. Figure 4.19 is the approximated waveforms and the Warp simulation results. We assume 1% perturbative wave towards to the primary focusing wave as the error-induced lattice symmetry breaking. Here, we use 1MHz for the primary wave in the S-POD, the perturbative wave becomes 1/42 MHz due to $N_{sp} = 1$. Comparison with the no-error case ($N_{sp} = 42$) of the stop bands, the resonance instability regions are become wider by the 1% perturbative wave.

Figure 4.20 shows the Warp simulation results adding two perturbative waves. Left column
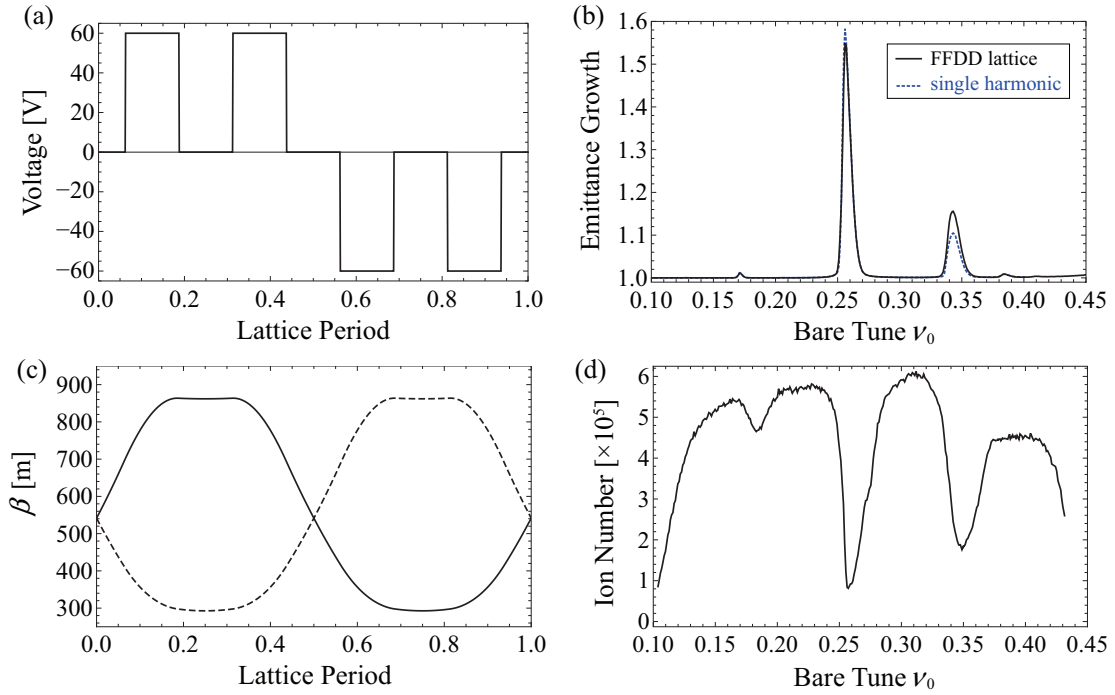
Figure 4.14: Results of the FFDD lattice simulations. (a) FFDD focusing system, (b) Stop bands by the emittance growth in Warp simulations. The black line is in the FFDD, and the blue dashed line is in the sinusoidal (rf) focusing for the comparison. where the tune depression η is 0.95. (c) Typical beta functions in the triplet lattice. Solid line is the horizontal beta function, and the dashed line is the vertical. (d) Experimental results of the FFDD lattice. The ordinate of the panel (d) is the number of Ar^+ ions surviving after a 10 ms storage (10^4 periods). The initial ion numbers differ from the doublet results, because the focusing wave frequency is lower than the doublet wave to make two times as many box functions as the doublet lattice.

panels are the case of tune depression $\eta = 0.85$, middle panels are $\eta = 0.90$, and the right panels are $\eta = 0.95$. The 1st row panels show the results of superposing perturbation of $N_{sp} = 1$ and 3, the 2nd row is $N_{sp} = 1$ and 6, the 3rd row is $N_{sp} = 1$ and 14, and the 4th row is $N_{sp} = 1$ and 21. The large peaks which appear in the stop band are consistent with Eq. (4.32). We can also observe the small side bands in (g)~(l). These side bands are predicted in Ref. and it comes from the growth factor having the Fourier series element of the beta function.

4.2.6 Summary

In summary, we have studied space-charge induced resonance of an intense charged-particle beam propagating through various periodic focusing structures. In the case of each lattice structure, the almost all resonance instability regions are consistent with the linear Vlasov theory Eq. (4.9), but we recognize the side instability bands which generated by the lattice symmetry breaking. Moreover we find the time-evolution of the resonance are characterized by the resonance order. and the resonance strength depends on the envelope form of the beam.
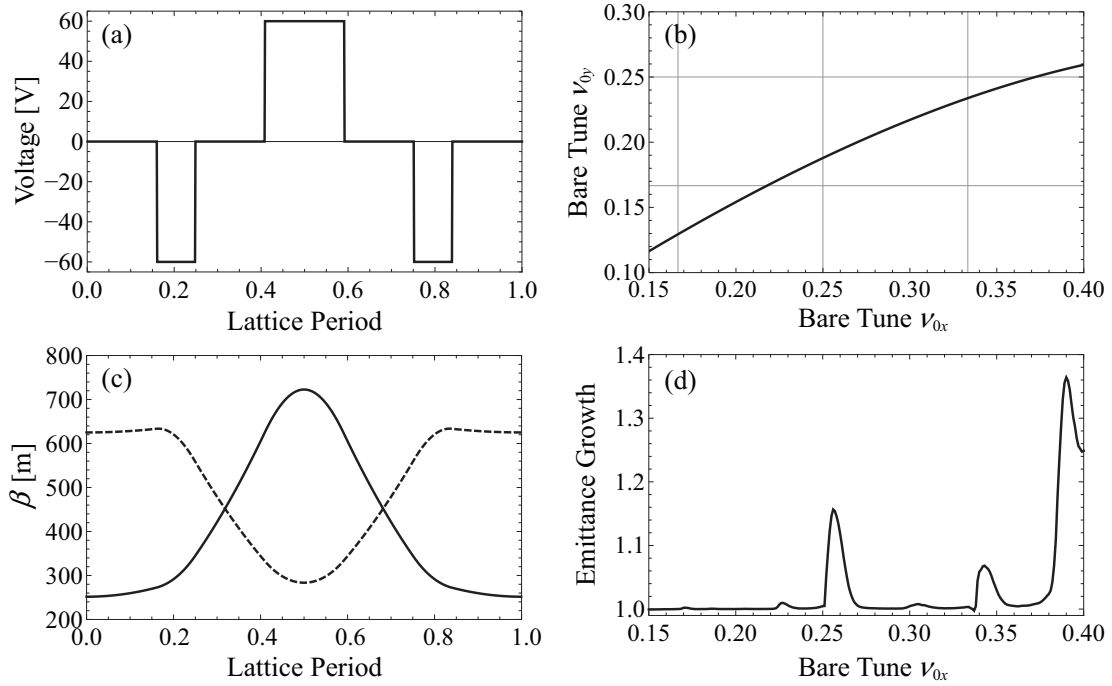
Figure 4.15: Results of the triplet lattice simulations. (a) Triplet focusing system, (b) Operating bare tune. Horizontal axis is x-coordinate bare tune and Vertical is y-coordinate bare tune. (c) Typical beta functions in the triplet lattice. Solid line is the horizontal beta function, and the dashed line is the vertical. (d) Stop band by the emittance growth in Warp simulations. The tune depression η is 0.95.
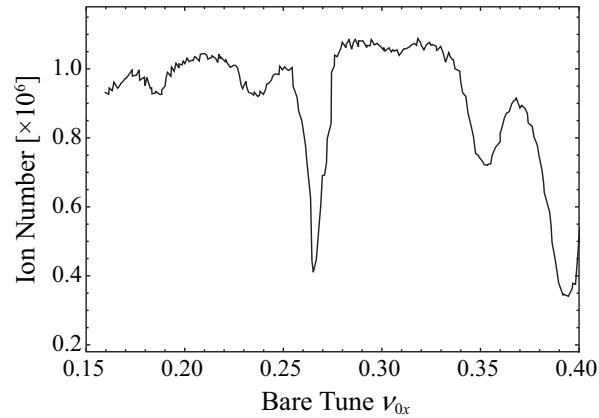
Figure 4.16: Results of the triplet lattice experiments. The ordinate of the panel is the number of Ar^+ ions surviving after a 10 ms storage (10^4 periods) at a fixed bare tune. The wave form is based on Fig. 4.15 (a), the operating bare tunes are identical to Fig. 4.15 (b). The resonance positions which shown by the ion losses are similar to the simulation results in Fig. 4.15 (d).
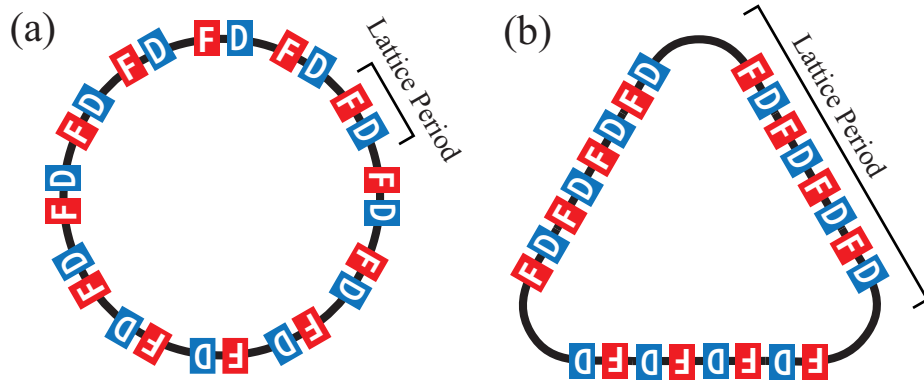
Figure 4.17: Super-periodicity and lattice period in accelerators. (a) $N_{sp} = 12$, (b) $N_{sp} = 3$.

(a) primary focusing wave   12 Focusing periods

(b) lattice-inducedwave $N_{sp} = 3$

(c) error-inducedwave $N_{sp} = 1$
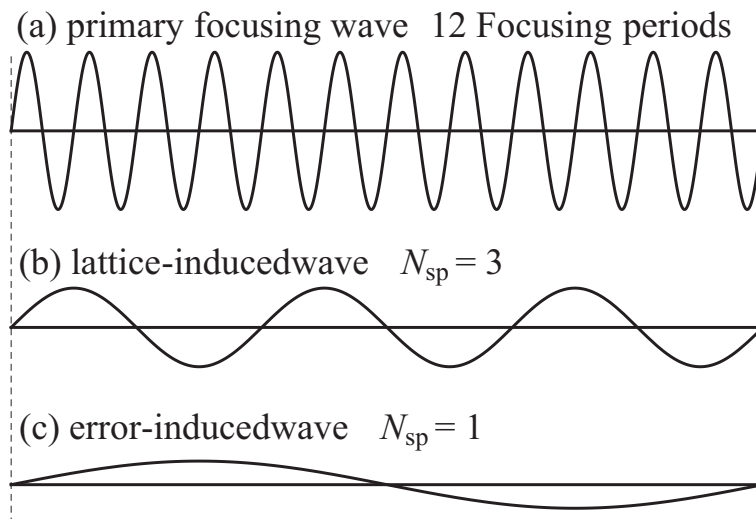
Figure 4.18: An example of focusing waves for the S-POD. This wave assumes the 4 FODO lattice and the super-periodicity is 3.
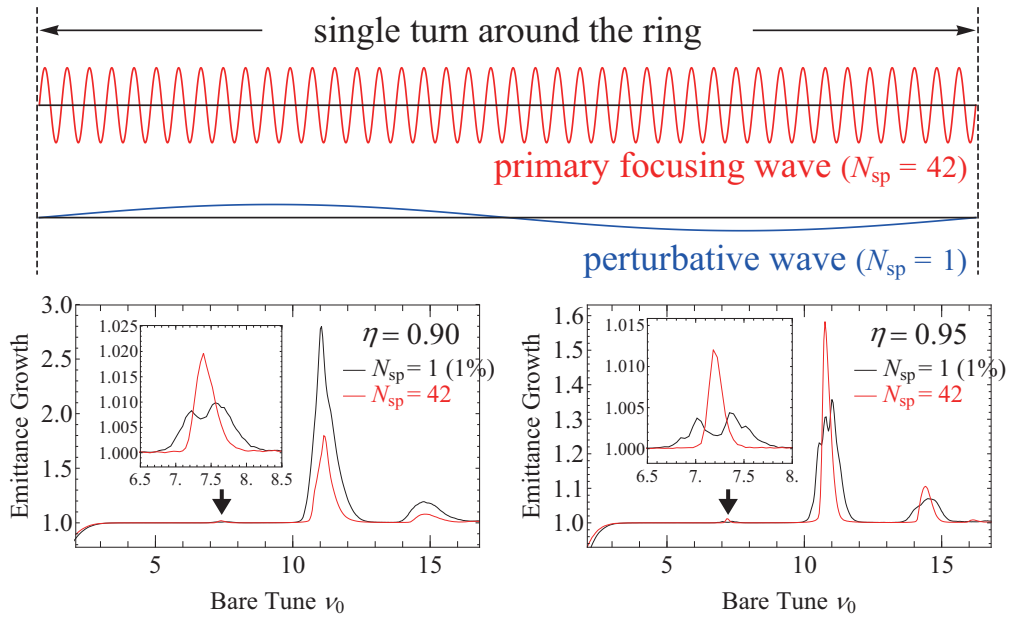
Figure 4.19: Upper panel shows the primary focusing wave (red) and the perturbative wave (blue) to reproduce the lattice symmetry breaking. Lower panels show the stop band by the Warp simulations (left: $\eta = 0.90$, right: $\eta = 0.95$), and comparing between 1% perturbative wave (black) and 0% (red) results. The resonance instability regions near $\nu_0 \approx 42/6 = 7$, $42/4 = 10.5$, and $42/3 = 14$ become wider by the symmetry breaking.
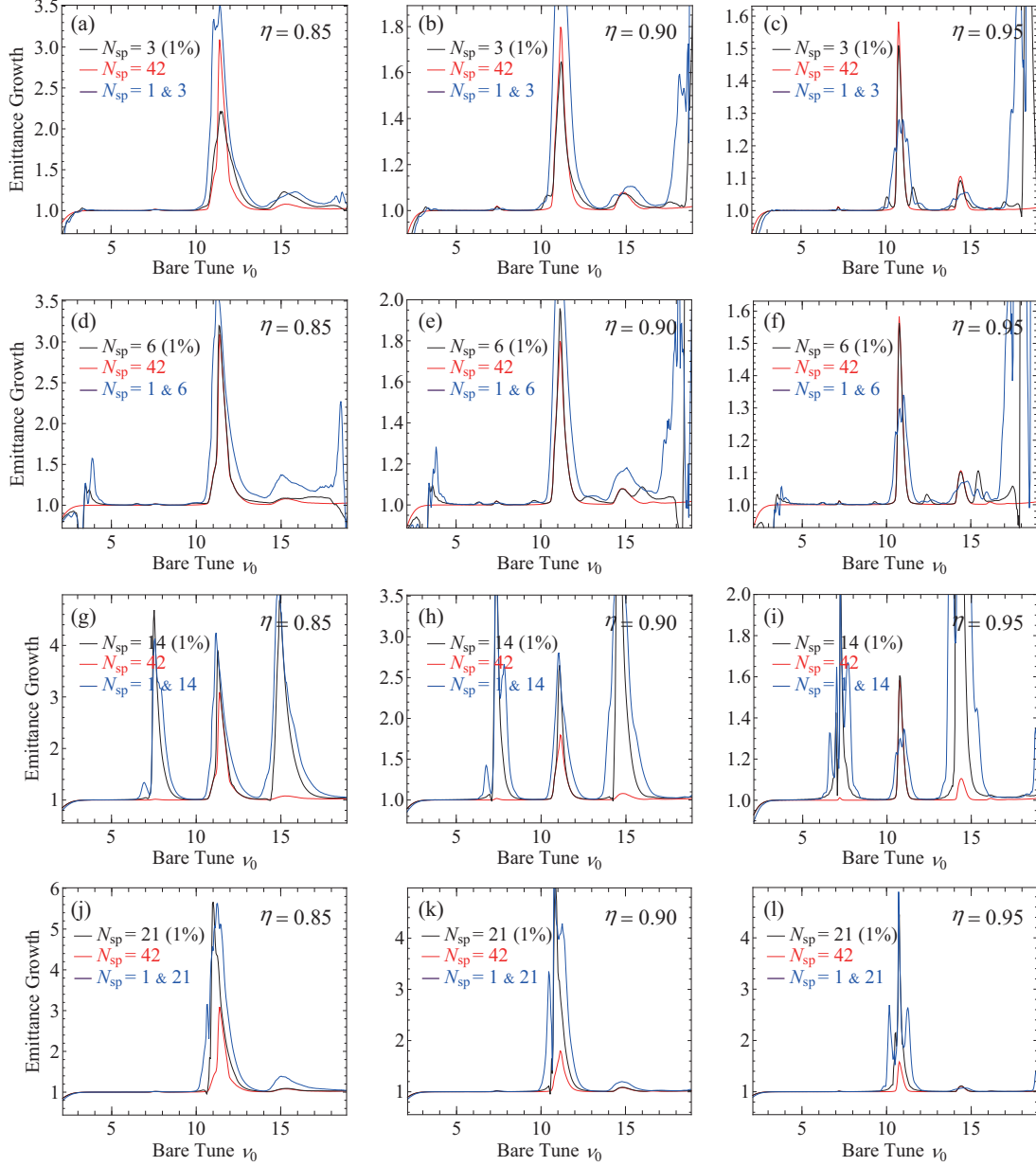
Figure 4.20: Warp simulation results with various super-periodicity perturbations. The left column shows tune depression $\eta = 0.85$ cases, the middle column is $\eta = 0.80$, the right column is $\eta = 0.95$. (a), (b), (c) $N_{sp} = 3$, (d), (e), (f) $N_{sp} = 6$, (g), (h), (i) $N_{sp} = 14$, (j), (k), (l) $N_{sp} = 21$.

54

Chapter 5

Theoretical study of resonance crossing

5.1 Motivation

In most of circular accelerators, transverse betatron tunes are usually fixed at certain optimum values that guarantee beam stability. The machine operating point is, however, not necessarily frozen but actually moves over a wide range in some cases. For instance, when the beam is exposed to a very strong cooling force, the interparticle Coulomb repulsion is gradually strengthened depressing the effective tune. As the beam density increases in phase space, the tune shift becomes larger and can eventually reach the magnitude of the initial bare tune at the ultralowemittance limit. Such a unique situation is expected to occur in advanced cooling experiments if several necessary conditions are satisfied [38, 39]. Another good example is nonscaling fixed field alternating gradient (FFAG) accelerators [40]. Considerable theoretical and experimental efforts have recently been devoted to design studies of nonscaling FFAGs for various purposes including hadron therapy, accelerator-driven reactor systems, a muon collider, and a neutrino factory [41, 42, 43, 44, 45]. In this type of machines, the bare tunes keep decreasing rapidly while the beam is accelerated by radio-frequency (rf) cavities. It is almost inevitable for the operating point to cross resonance stop bands, some of which may be quite dangerous.

5.1.1 Scaling and non-scaling FFAG accelerators

The scaling properties satisfied by the magnetic field $B_y = B_0(r/r_0)^k$ maintain a constant betatron tune, where B_y is the vertical magnetic field, r is the distance from the machine center, B_0 is the vertical magnetic field at $r = r_0$, and k is the field index. By combining a time-independent magnetic field with the stability of alternating gradient focusing, the scaling FFAG achieves a large dynamic aperture and large acceleration range. The orbits in a scaling FFAG are similar from injection to extraction, and the beam moves radially outward during acceleration unless k is chosen to be negative.

By choosing to ignore the scaling restriction, an accelerator lattice designer may introduce attractive properties such as magnet simplicity, design flexibility, and compact orbits. This violation of the scaling properties can be achieved in a number of ways, and as such the NS-FFAG

covers a wide spectrum of possible designs [46, 47]. The linear nonscaling version of the FFAG was proposed in order to simplify the design to the extent that only linear (quadrupole) fields were required, easing the magnetic construction. This is the type of accelerator recently constructed and commissioned in the United Kingdom at Daresbury Laboratory, called EMMA, the Electron Model for Many Applications [37, 41].

5.2 Crossing of half-integer and nonlinear resonance bands

It is known that the natural resonance crossing caused by beam compression in phase space can limit the achievable emittance [48, 49]. The cooling process is strongly interrupted once the effective operating point comes to a stop band of the linear (second-order) collective resonance. To avoid crossing such severe stop bands throughout the whole cooling process, the design betatron phase advance per lattice period must be below 90 degrees [49]. On the other hand, in the case of nonscaling FFAGs, the operating point moves due to the reduction of beam focusing forces during acceleration. It is often said that we could cross resonances without serious deterioration of beam quality if the crossing speed is sufficiently fast. This sounds reasonable because the beam must need a certain period of time before it recognizes that the external driving force is surely periodic. The most important question is how fast we have to move the operating point. Numerical simulations and even experimental studies with existing machines have been carried out to answer this practical question [50, 51, 52, 53, 54].

5.2.1 Emittance-growth simulation

Low-density regime

Let us first look at the case where the collective Coulomb potential is negligible. EMMA is currently operated in this low-density regime. In this subsection, we simply switch off space-charge interactions in Warp simulations. Root-mean-square emittance evolution during resonance crossing is plotted in Fig. 5.1 as a function of rf periods (time). The bare tune ν_0 per single rf period is changed from 0.4 to 0.17 in both cases by ramping the amplitude of the rf voltage. The resonance crossing speed in the upper case roughly corresponds to 20-turn (840 FODO periods) acceleration in EMMA while the lower case is twice faster. We naturally observe less emittance growth for quicker resonance crossing. It has been confirmed through separate simulations that the growth rate almost linearly increases as we slow down the bare-tune sweeping. Each panel in Fig. 5.1 indicates a slight emittance growth near a specific rf period at which the bare tune is near $\nu_0 \approx 1/3$, which suggests that the emittance growth is caused by crossing a third-order resonance stop band. Black lines have assumed 0.1 mm (rms) misalignments of the LPT electrodes that considerably strengthen nonlinear fields. The emittance growth disappears at low density without rod misalignments as demonstrated in Fig. 5.1 (red line).

High density regime
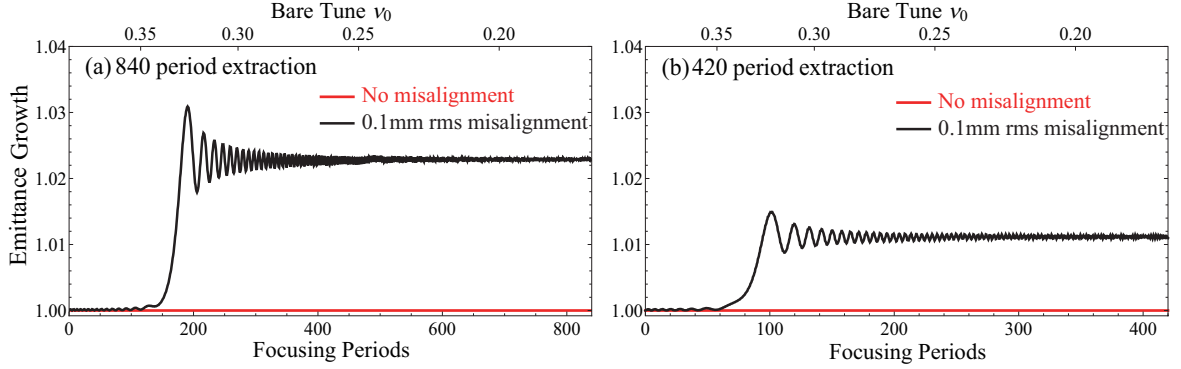
Figure 5.1: Warp simulation results without space charge. The sweep range is from $\nu_0 = 0.4$ to $\nu_0 = 0.17$ (a) Sweep tune in 20 turns. (b) Sweep tune in 10 turns. Low-order nonlinearities have been intentionally enhanced in these simulations, considering the possible electrode misalignments of 0.1 mm. For reference, simulation results without the misalignments are plotted with red lines, which indicate almost no emittance growth.

We now turn on the Coulomb potential. Because of the nonlinear nature of space-charge interactions, collective resonances of various orders can be excited even in an ideal linear focusing channel. A 1D Vlasov theory has revealed that the collective mode of m-th order becomes unstable when the following condition is fulfilled (cf. the same as Eq. (4.9)):

$$m(\nu_0 - C_m \Delta \nu) \approx \frac{n}{2}, \tag{5.1}$$

where $\Delta \nu$ is the tune shift generated by the space-charge repulsion, C_m is the positive constant depending on the mode number m, and n is an integer. In general, the incoherent tune shift $\Delta \nu$ cannot uniquely be determined due to a finite effective tune spread.

Strictly speaking, there exist not one but many resonances in the vicinity of a particular tune. As readily understood from Eq. (5.1), resonance conditions for different collective modes become similar whenever the corresponding ratios of $n = m$ are identical. Those resonances with the same $n = m$ ratio overlap each other, which may make it difficult to distinguish the instability of one mode from those of the others. The instability of a highly nonlinear mode is, however, generally quite weak in practice or even invisible due to Landau damping unless the strong external driving force of the same order is present. The amplitudes of the fourth and higher-order multipole fields at the full aperture of the LPT are estimated to be less than 0.5% of the quadrupole amplitude even with the 0.1 mm rms misalignments of the electrodes. Considering this fact, we reasonably expect no strong excitation of highly nonlinear resonances.

In the condition (5.1), special attention should be paid to the factor 1/2 on the right-hand side, which is missing in the well-known Sacherer's coherent resonance criterion [16]. The above condition says that there exist twice as many resonance stop bands as Sacherer predicted. Most importantly, the linear resonance ($m = 2$) can occur when the tune is close not only to half integers
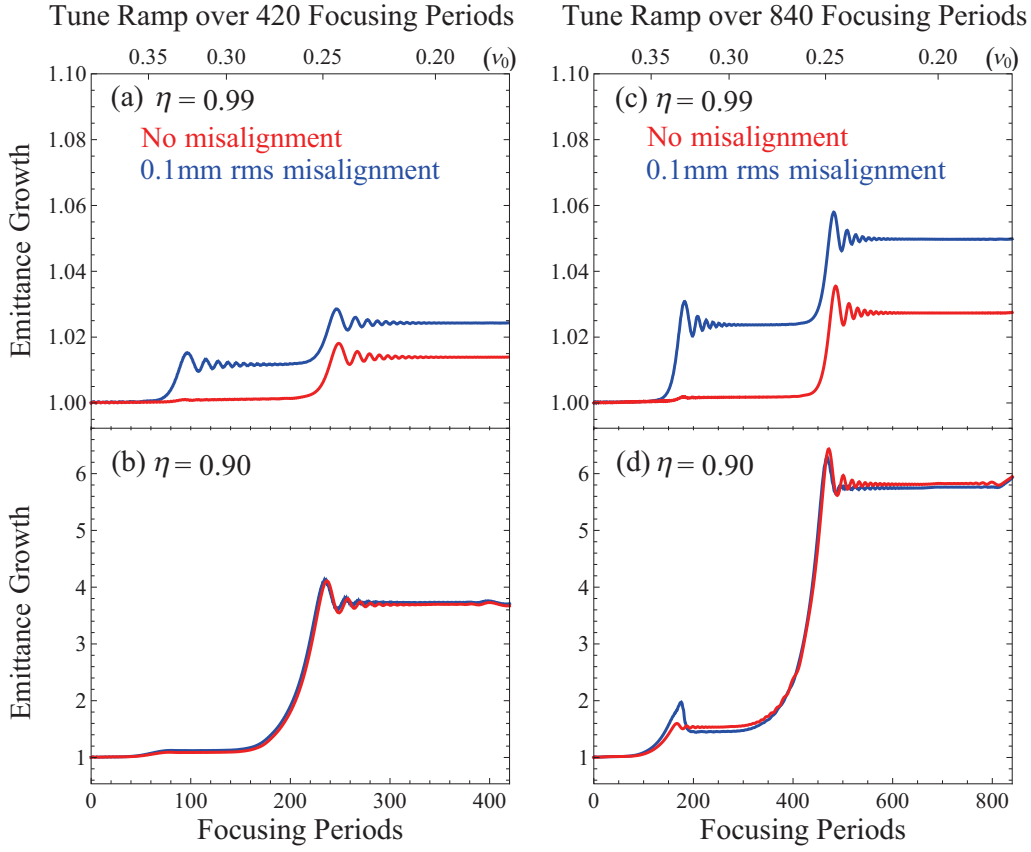
Figure 5.2: Warp simulation results with space charge. Input parameters here are similar to those adopted in Fig. 5.1, except that the collective Coulomb potential is now turned on. Two different tune depressions, i.e. $\eta = 0.99$ and 0.9, are chosen, for example. Red curves are obtained with no electrode misalignments while blue curves take into account rms misalignments of 0.1 mm.

but also to quarter integers. Since ν_0 crosses $1/4$ in EMMA, this quarter integer linear resonance might play a crucial role at high beam intensity. The existence of such a linear resonance has been widely known in linear transport theories (while the above criterion applies to all nonlinear modes as well). For instance, a 2D Vlasov theory has reached the same conclusion that the strong second-order ($m = 2$) resonance can be excited once the bare tune per unit FODO cell exceeds $1/4$. The theory even recommends avoiding the third-order ($m = 3$) resonance that occurs when the tune per cell goes beyond $1/6$ (60-degree phase advance).

The Warp simulations of resonance crossing at different speeds of bare-tune sweep result in the emittance evolution in Fig. 5.2. The emittance growth rates are much larger than the results in Fig. 5.1 where the Coulomb potential is ignored. In particular, the linear resonance at $\nu_0 \approx 1/4$ has seriously affected the plasma quality at high density while no such effect is identified in the simulations without space charge.

Although the large stop band near $\nu_0 \approx 1/4$ can include the effect from the fourth-order resonance as well, the linear instability of the $m = 2$ mode should be most responsible for the observed

emittance growth. In fact, if the fourth-order resonance is really dominant there, the third-order resonance near $\nu_0 \approx 1/3$ has to be much stronger because, first, it is a lower-order resonance than the fourth-order, second, the sextupole nonlinearity assumed in the simulations is greater than the octupole and, third, we only observe the third-order stop band in Fig. 5.1 (except for an extremely small emittance growth at $\nu_0 1/4$)

5.2.2   Ion-loss simulation

The tune depression η is the most important parameter that characterizes the collective behavior of an intense beam. In fact, the resonance condition (5.1) only contains the tune shift $\Delta \nu$ as a space-charge-related quantity that can uniquely be determined once the choice of η is made. The direct experimental determination of η is difficult not only in the LPT but also in any high-intensity accelerators because it requires a precise survey of phase space. No phase-space monitor is presently available in the S-POD system (while laser-induced fluorescence diagnostics is under development for a nondestructive measurement of plasma emittance). Despite the lack of detailed information of the ion distribution in phase space, it is still feasible to estimate an approximate magnitude of η by measuring the shifts of stop bands.

The results of the resonance crossing simulations in Fig. 5.2 only weakly depend on the initial plasma temperature T_p. Even if we change T_p to some degree, the emittance evolution patterns are not essentially affected as long as the starting value of η is maintained. On the other hand, T_p becomes meaningful when we numerically simulate the actual ion-loss process. In S-POD, a larger emittance growth of a plasma naturally gives rise to more severe particle losses. We can thus judge, through ion-loss measurements, how seriously the plasma is damaged by resonance crossing. The amount of ion losses depends on the mechanical design of the LPT and on the plasma temperature. While T_p is inessential in the emittance evolution, it does change the spatial extent of the plasma at the beginning. This parameter is, therefore, of importance in ion loss simulations. According to past S-POD experiments based on a similar LPT, the transverse temperature of an equilibrium plasma is typically a few thousand K. We here try three different values of T_p (i.e., 0.1, 0.2, and 0.3 eV) to check how much ion losses are expected in S-POD. An example is shown in Fig. 5.3 where we have assumed the same tune depression, tune ramping speed and range as considered in Fig. 5.2(d). In this simulation, we have simply removed particles once they hit the quadrupole rods. Not surprisingly, many particles are lost when the LPT operating point traverses the regions of large emittance growth. The loss rate is enhanced, as expected, at higher plasma temperature. We have also confirmed that almost no ion losses occur over a wide range of the crossing speed u when the tune depression is reduced to 0.99. The definition of the crossing speed u is

$$u = \frac{\nu_0^{\text{ini}} - \nu_0^{\text{fin}}}{N_{\text{cell}}}, \tag{5.2}$$

where ν_0^{ini} and ν_0^{fin} are the initial and finite bare tunes, and N_{cell} is the focusing periods required for the tune ramping.
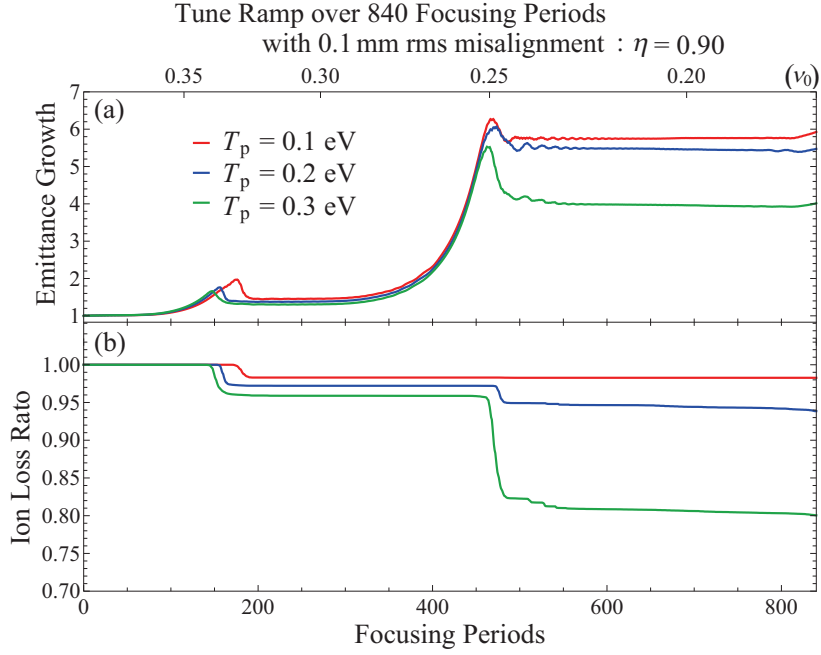
Figure 5.3: Results of ion-loss simulations with the Warp code. The input parameters are identical to those assumed in Fig. 5.2 (d), except for the initial plasma temperature T_p. The rms misalignments of the electrodes have been set at 0.1 mm. The ordinate of the lower panel represents the number of ions surviving, divided by its initial value. We here consider $T_p \approx 0.1$, 0.2, and 0.3 eV, recalling previous experimental data [55]. To simulate ion losses in actual experiments, macro-particles that have gone across the electrode boundaries are just removed. The observed T_p dependence of emittance evolution is caused largely by the macro-particle losses.

5.2.3 Comparison with experimental results

The experimental measurement data is compared with the ion-loss simulations in Fig 5.4. The ordinate represents the ratio of ion numbers before and after the full tune ramping from $v_0 = 0.4$ to 0.17. The initial plasma temperature has been set at $T_p = 0.3$ eV in all Warp simulations while four different tune depressions are assumed at the beginning. These results suggest that the effective tune depression η is initially near 0.85 at $N_{in} \approx 10^7$ and changed to about 0.95 at $N_{in} \approx 10^6$. The emittance growth rates calculated from these simulations at $u = 5.48 \times 10^{-4}$ (corresponding to 10-turn extraction from EMMA) are 1.0 for $\eta = 0.99$, 1.5 for $\eta = 0.95$, 3.4 for $\eta = 0.90$ with 5% ion loss, and 3.9 for $\eta = 0.85$ with 23% ion loss. We thus expect that only little deterioration of beam quality will take place in EMMA even with rather strong nonlinearity if the space-charge-induced tune shift is less than a few % of the bare tune.   Since the coherent resonance at $v_0 = 1/4$ intrinsically exists in any high-intensity machines even without imperfection fields, it is practically important to figure out how the plasma gets heated at this resonance depending on the crossing speed and initial particle density. The upper panel in Fig. 5.5 shows the experimental data obtains with various N_{in}'s. The operating tune v_0 is ramped from 0.31 to 0.23 to see the effect from the quarter-integer stop band. The corresponding Warp simulation results with several
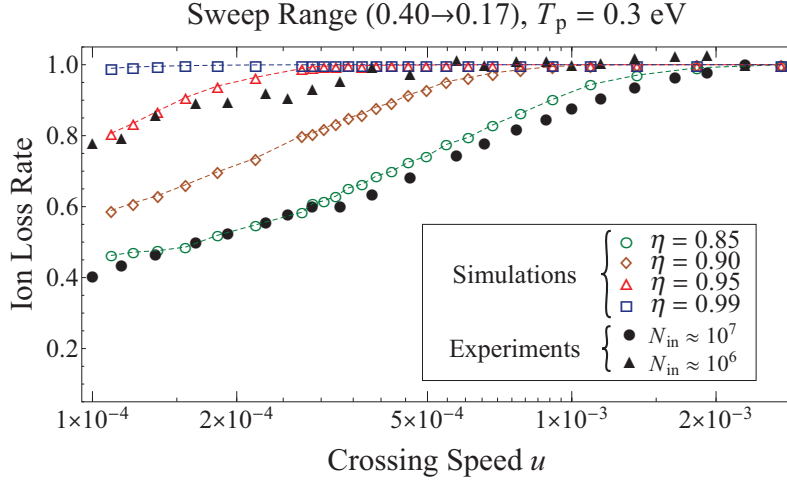
Figure 5.4: Comparison of measurement data with the corresponding ion-loss simulations of the resonance crossing. The sweep range is from 0.40 to 0.17. Empty symbols are the simulation results ($T_p = 0.3$ [eV]) , and filled symbols are the experimental results.

different values of η are given in the lower panel, which agree fairly well with the experimental observations. Although the current S-POD system has no emittance monitor, the good agreement between the experimental and numerical results justifies using the simulation data to draw an approximate scaling law of possible emittance growth after the intrinsic linear resonance crossing.

5.2.4 Scaling of emittance growth

Figure 5.6 shows some examples of the numerically evaluated final emittance at $\nu_0 = 0.24$ normalized by the initial value at $\nu_0 = 0.31$. Since the emittance behavior during resonance crossing is insensitive to the initial plasma temperature unless too many particles escape from the LPT acceptance (see Fig. 5.3), a lower plasma temperature (0.1 eV) has been assumed here to lighten particle losses. Even then, a considerable amount of ions are lost when a large emittance growth occurs. The open squares and triangles in Fig. 5.6 indicate numerical data with finite particle losses. We clearly see the linear dependence of the emittance ratio $\kappa_{1/4}$ on the tune depression η in the region where particle losses are negligible. For more information, results of about 1500 systematic Warp simulations with various u and η are summarized in Fig. 5.7. The white line in the picture indicates the border below which finite particle losses are detected during the resonance crossing. Naturally, the emittance growth becomes more severe for a slower crossing speed and/or higher particle density.

Each solid line in Fig. 5.6 is a simple linear fitting based on the function

$$\kappa_{1/4} - 1 = e_f(\eta_0 - \eta), \tag{5.3}$$

where the fitting constants η_0 and e_f both depend on the resonance crossing speed u. Note that space-charge-induced instabilities are self-limited; namely, the emittance growth is sooner or later
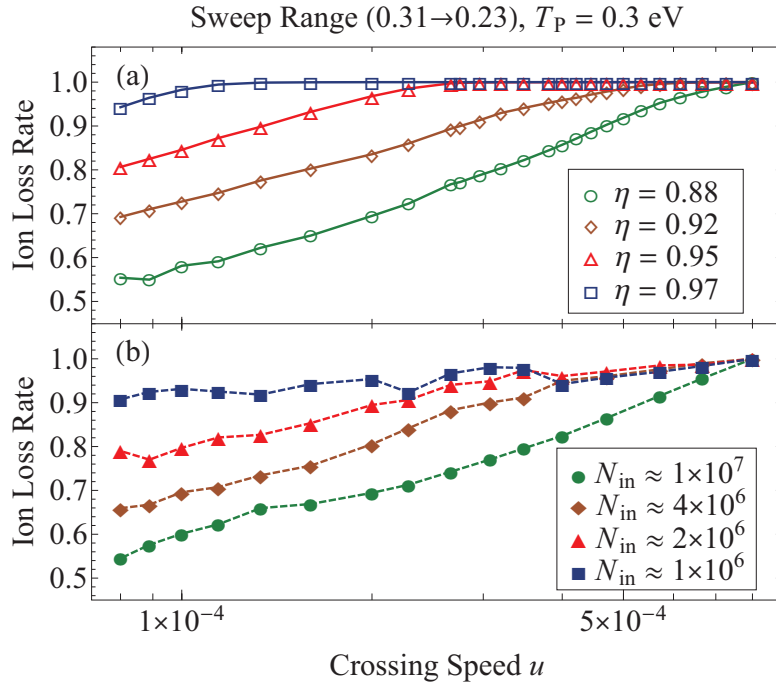
Figure 5.5: Comparison of measurement data with the corresponding ion-loss simulations of the resonance crossing. The sweep range is from 0.31 to 0.23. Experimental results of the quarter-integer resonance crossing with various initial ion numbers are plotted in the upper panel (a) as a function of the crossing speed u. The corresponding Warp simulations assuming the initial plasma temperature of 0.3 eV are shown in the lower panel (b).
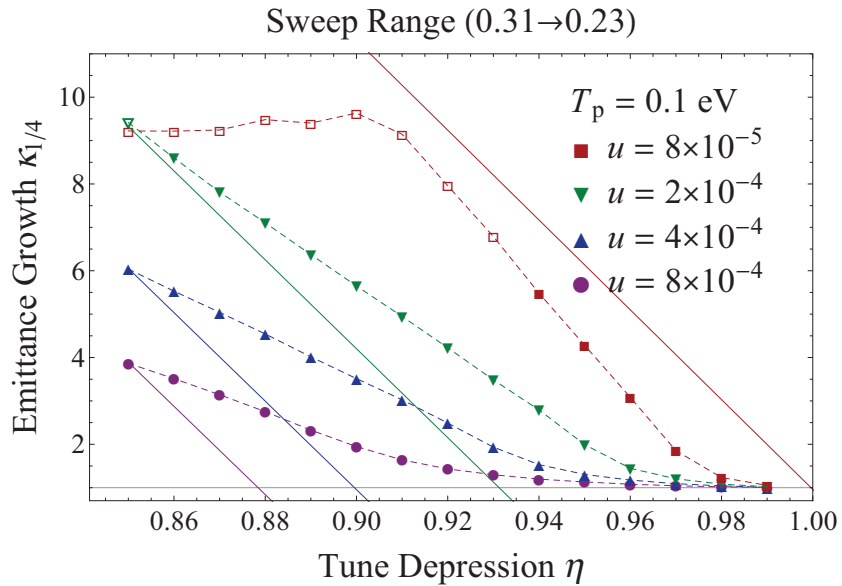
Figure 5.6: An examples of Warp simulation data for quarter-integer resonance crossing. The emittance growth rate $\kappa_{1/4}$ after crossing the stop band at $\nu_0 \approx 1/4$ is plotted at four different values of u as a function of η.
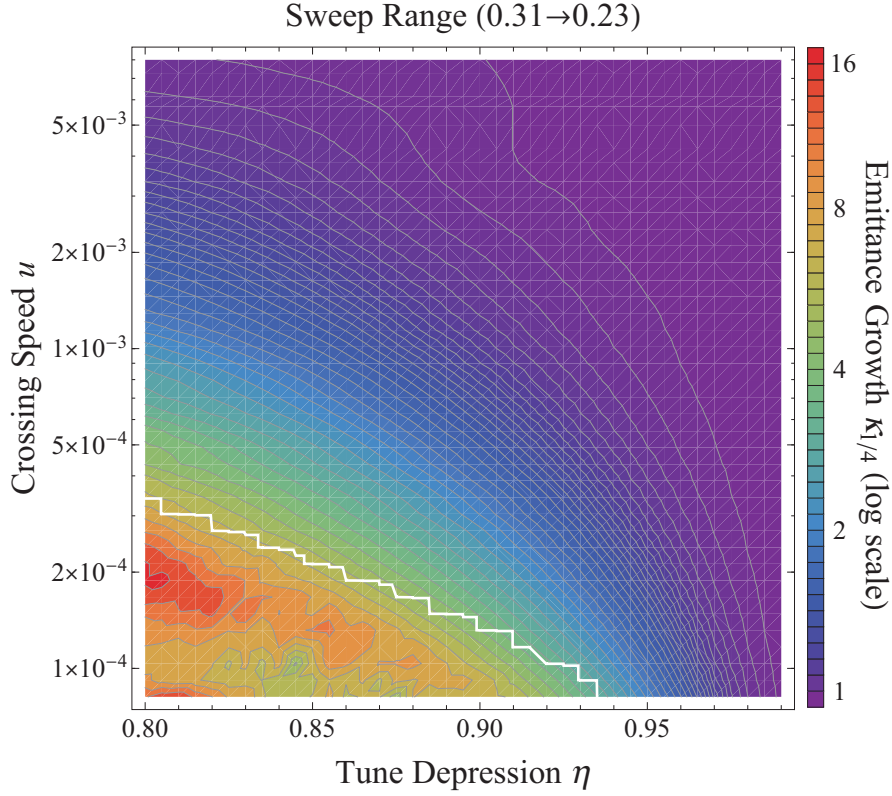
Figure 5.7: Warp simulation results in η-u space. The color chart shows the emittance growth with log scale. The final-to-initial emittance ratio $\kappa_{1/4}$ after the quarter-integer resonance crossing is evaluated from systematic Warp simulations and color-coded in η-u parameter space. The initial plasma temperature at $\nu_0 = 0.31$ has been set at 0.1 eV in all simulations. The white solid line indicates the border below which finite particle losses occur due to a large emittance growth before ν_0 reaches the final value 0.23.

stopped because it reduces the plasma density, thus weakening the space charge interactions. The fitting with Eq. (5.3) is, therefore, only valid when $\kappa_{1/4}$ is not too large. The parameter η_0 roughly represents the threshold tune depression at which the emittance starts to grow. For the examples in Fig. 5.6, we have $(e_f, \eta_0) = (121.9, 0.977)$ for $u = 8 \times 10^{-5}$, $(e_f, \eta_0) = (73.1, 0.964)$ for $u = 2 \times 10^{-4}$, $(e_f, \eta_0) = (51.0, 0.949)$ for $u = 4 \times 10^{-4}$, and $(e_f, \eta_0) = (38.7, 0.925)$ for $u = 8 \times 10^{-4}$. Figure 5.8 illustrates the u dependence of the two fitting constants. A quick estimate of the critical tune depression η_0 and the slope e_f can be made by approximating these curves with proper functions of u. The solid line in each panel is a simple trial fitting function; we have here adopted

$$\eta_0 \approx -g_{c1} \ln u + g_{c2} \quad \text{and} \quad e_f \approx h_{c1} u^{h_{c2}} \tag{5.4}$$

with the fitting constants $(g_{c1}, g_{c2}) = (0.028, 0.723)$ and $(h_{c1}, h_{c1}) = (0.896, 0.519)$. We are now able to plot $\kappa_{1/4}$ as a function of the crossing speed u by using the scaling law in Eq. (5.3) together with Eq. (5.4). The solid lines in Fig. 5.9 show four examples with different values of η while symbols represents Warp simulation results. We observe reasonable agreement between the
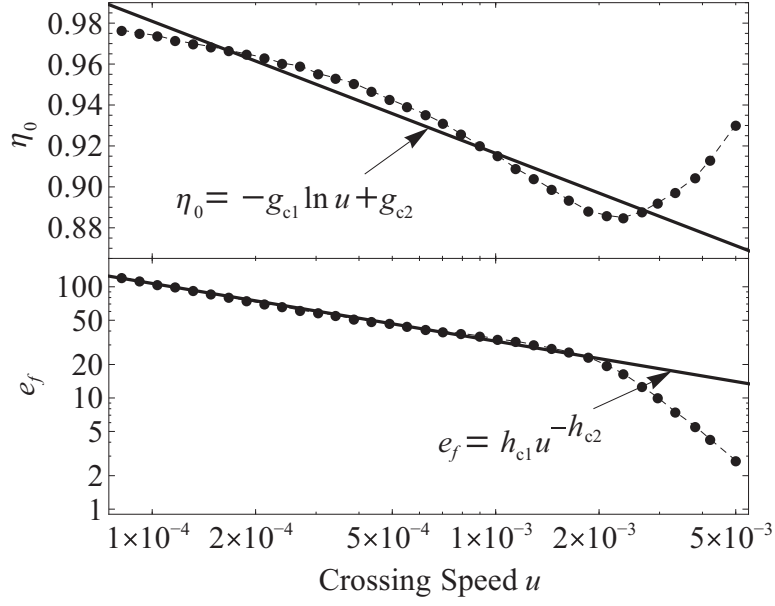
Figure 5.8: Fitting constant estimation. The parameters η_0 and e_f in Eq. (5.3) are evaluated from WARP simulation data as a function of u.
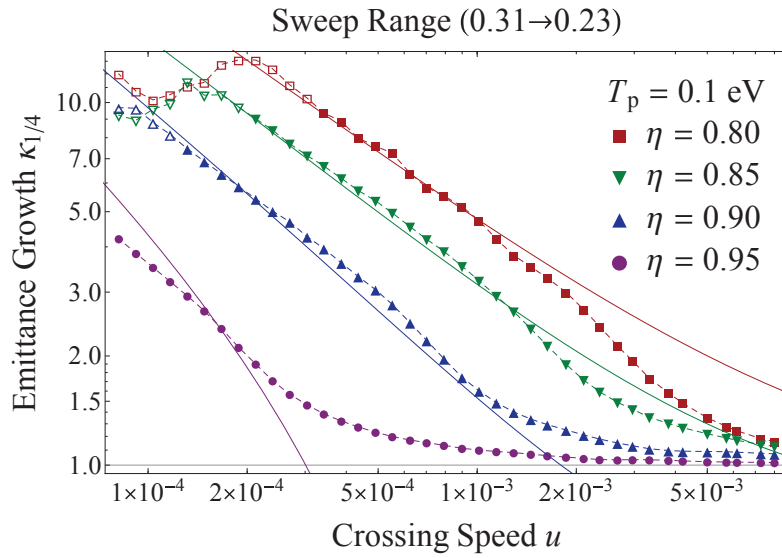
Figure 5.9: Warp simulation data of quarter-integer resonance crossing. The u dependence of the emittance growth rate $\kappa_{1/4}$ is plotted for four different initial values of η. The initial plasma temperature T_p has been set at 0.1 eV in all simulations here to minimize particle losses.

scaling law and PIC simulation results.

5.2.5 Summary

We have investigated fundamental features of collective resonance crossing by the multi-particle simulations and compared with the experimental results. When a machine holds very high lattice symmetry, three instability regions are identified in Chapter 4. We conclude that these instabilities are due mainly to the lowest- and second lowest-order resonances rather than to higher-order nonlinear resonances; namely, one of them at $\nu_0 \approx 1/4$ is the linear ($m = 2$) stop band and the other two at $\nu_0 \approx 1/6$ and $1/3$ are the third order ($m = 3$) while there could exist weak higher-order stop bands overlapping at these tunes. Although this interpretation is contradictory to that in Ref. [52], the coherent resonance criterion in Eq. (4.9) and other previous works on space-charge dominated beam transport [38, 49, 56, 11, 57, 58] support our conclusion. In addition, the present numerical results suggest that crossing the nonlinear stop band at $\nu_0 \approx 1/6$ is almost harmless. Another third-order resonance at $\nu_0 \approx 1/3$ is stronger, but at low particle density, the emittance growth from this resonance crossing should be negligible in the absence of excess nonlinearity due to electrode misalignments. The linear stop band at $\nu_0 \approx 1/4$, generated by the lowest-order resonance, is most dangerous and unavoidable at high density unless the tune variation range is sufficiently narrower than 0.25 per single focusing period. As the plasma becomes denser, this stop band grows causing serious emittance growth even at rather high resonance crossing speed.

We have also derived a simple scaling law of the emittance growth caused by the intrinsic resonance crossing at $\nu_0 \approx 1/4$. As shown in Eq. (5.3) and in Fig. 5.6, the emittance ratio $\kappa_{1/4}$ before and after the quarter-integer resonance crossing has approximate linear dependence on the tune depression η. This conclusion is consistent to the previous finding in Ref. [52]. The two fitting parameters can roughly be estimated from Eq. (5.4) as a function of the resonance crossing speed u.

5.3   Integer resonance crossing

We now pay particular attention to integer resonance crossing. Linear NS-FFAGs including EMMA are unique in routinely crossing multiple first-order integer resonances, in some cases more than ten times per acceleration cycle. Naturally, one should expect negative consequences of such a design feature. It is, however, widely held that, in the case of fast resonance crossing, betatron amplitudes will not grow significantly and the beam will not deteriorate. Such resonances do not generally occur in a regular LPT because of the symmetric excitation of the four LPT electrodes, which eliminates a periodic dipole component in the plasma confinement field. Here we intentionally introduce an rf dipole field to generate stop bands of integer resonances. Considering the typical low-intensity conditions of EMMA operation, a relatively small number of ions are confined in the LPT, to ensure that collective space charge effects remain negligible.

5.3.1   Modeling of dipole peturbation in S-POD

EMMA is a linear NS-FFAG for electrons, the main parameters of which are given in Table 5.1.

Energy range	10-20 [MeV]
Cell type	FD doublet
Number of cells	42
Integrated quadrupole gradient	0.402(QF) and 0.367(QD) [T]
Cell length	394.481[mm]
Ring circumference	16.568[m]

Table 5.1: Main parameters of the EMMA NS-FFAG.

The design consists of 42 doublets of quadrupoles in which the dipole component is achieved by simply sending the beam through the quadrupoles off axis. The magnets are mounted on precise slider mechanisms in order to vary the bending and focusing field components independently. In general, the predominant driving forces for integer resonances in a linear NS-FFAG are alignment errors of the quadrupole magnets that cause dipole field errors and errors in the dipole magnetic field itself if such a field is present. [1] The transverse closed orbit distortion (COD) in a circular accelerator due to a dipole error field $\Delta B/B$ is well known and obeys the differential equation

$$\frac{d^2 x_{\text{COD}}}{ds^2} + K_x(s) x_{\text{COD}} = -\frac{\Delta B}{B\rho},$$ (5.5)

where ρ is the local curvature of the design beam orbit, s is the path length, and K_x is the magnetic quadrupole focusing function determined by the machine lattice. When the average radius of the machine is R_c, application of the smooth approximation to Eq. (5.5) yields

$$\frac{d^2 x_{\text{COD}}}{d\theta^2} + v_0^2 x_{\text{COD}} = -R_c^2 \frac{\Delta B}{B\rho},$$ (5.6)

where v_0 is the bare tune and the angle $d\theta (= ds/R_c)$ increases by 2π every single turn. The dipole error is periodic and can thus be expanded into a Fourier series, where b_n and ϕ_n are constant parameters. The solution to Eq. (5.6) diverges when v_0 is an integer (integer resonance).

As mentioned above, the LPT is, in principle, free from integer resonances. A dipole driving force can, however, be provided by applying additional rf voltages to one or two of the four quadrupole electrodes [2, 59, 21]. We apply either pulsed or sinusoidal perturbing voltages of opposite signs to two horizontal electrodes. By neglecting nonlinearity of the transverse rf focusing fields and the space charge potential, the equation of the transverse ion motion in a LPT with a dipole driving field can be written as

$$\frac{d^2 x}{d\tau^2} + K_{\text{rf}}(\tau) x = -\frac{q\xi}{mc^2 R_0} V_D(\tau),$$ (5.7)

<hr/>

[1] In fact, in EMMA there is in addition a large septum leakage field of 0.6×10^3 Tm. To emulate this strong local dipole kick in S-POD, we need a rather high dipole voltage that causes almost instant ion losses due to the limited aperture of the current LPT design.
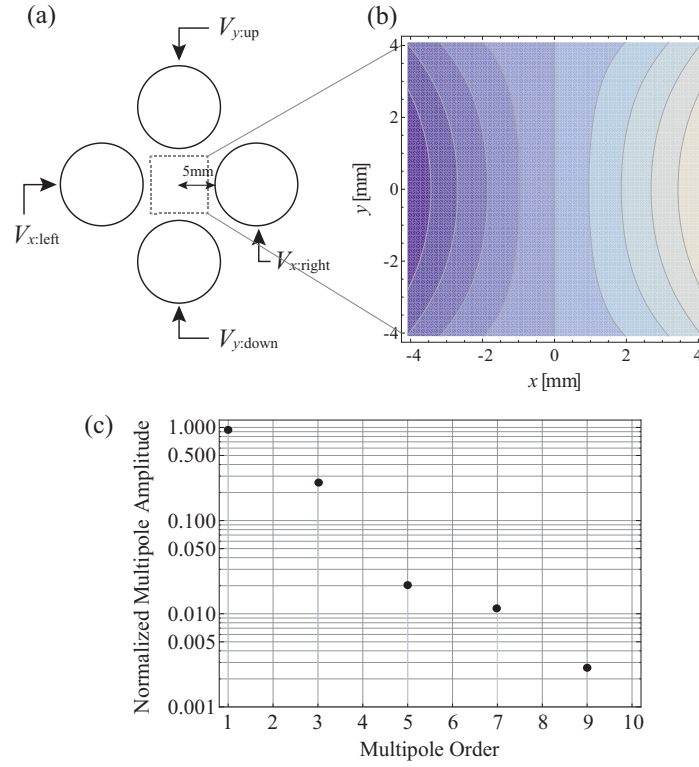
Figure 5.10: (a) rf voltages applied to the quadrupole electrodes of the trap. (b) Contour plot of the dipole field. (c) Normalized multipole amplitude of the dipole field. Other odd order multipoles are generated in the confinement region not only the dipole.

where m and q are the mass and charge state of confined ions, respectively, R_0 is the minimum distance to the electrode surface from the trap axis (in other words, the radius of the LPT aperture $R_0 = 5$ mm), $\tau = ct$ with c the speed of light, $K_{\rm rf}$ is the rf quadrupole focusing function, ξ is a constant factor depending on the geometry of the quadrupole electrodes ($\xi = 0.795$ in this case), and V_D is the dipole perturbation voltage indicated in Fig. 5.10. The applied voltage for four rods are,

$$V_{x:\rm right}(\tau) = V_Q(\tau) + V_D(t), \tag{5.8}$$

$$V_{x:\rm left}(\tau) = V_Q(\tau) - V_D(t), \tag{5.9}$$

$$V_{y:\rm up}(\tau) = V_{y:\rm down}(\tau) = -V_Q(\tau). \tag{5.10}$$

When the amplitude of the rf quadrupole voltages applied to the four electrode rods is V_Q, $K_{\rm rf}$ is equal to $K_{\rm rf}(\tau) = 2qV_Q(\tau)/mc^2R_0^2$. We now consider a NS-FFAG composed of $N_{\rm sp}$ identical doublet focusing cells. In the EMMA case, $N_{\rm sp} = 42$. A single turn around the machine then corresponds to P sinusoidal periods in the function $K_{\rm rf}$ (see Fig. 5.11). The time dependence of

K_{rf} in Eq. (5.7) is smoothed to give

$$\frac{d^2x}{d\theta_P^2} + \nu_0^2 x = -\left(\frac{N_{\text{sp}}\lambda}{2\pi}\right)^2 \frac{q\xi}{mc^2 R_0} V_D(\theta_P),\qquad(5.11)$$

where λ is the wavelength of single rf focusing period in the LPT and the angle $\theta_P(=2\pi\tau/N_{\text{sp}}\lambda)$ increases by 2π every turn. In general, the dipole perturbation VD is periodic with a periodicity of 2π and can be expressed, similarly to $\Delta B/B$, as $V_D = \Sigma_j w_j \cos(j\theta_P + \phi_j)$, where w_j and ϕ_j are constants. The on-resonance solution to Eq. (5.11), i.e., the diverging orbit under the condition $\nu_0 = n$, is given by

$$\begin{aligned}
x = {} & x_0 \cos(n\theta_P + \alpha) \\
& -\frac{1}{2}\left(\frac{N_{\text{sp}}\lambda}{2\pi}\right)^2 \frac{q\xi}{mc^2 R_0} \frac{w_n \theta_P}{n} \sin(n\theta_P + \phi_n) \\
& -\left(\frac{N_{\text{sp}}\lambda}{2\pi}\right)^2 \frac{q\xi}{mc^2 R_0} \sum_{j\neq n} \frac{w_j}{n^2 - j^2} \cos(j\theta_P - \phi_j),
\end{aligned}\qquad(5.12)$$

where x_0 and α are constant. Comparing the driving term in Eq. (5.11) with that in Eq. (5.6), we find that the physical orbit distortions in these systems are similar when

$$V_D \approx \frac{mc^2 R_0}{q\xi}\left(\frac{2\pi R_0}{N_{\text{sp}}\lambda}\right)\frac{\Delta B}{B\rho}.\qquad(5.13)$$

This formula allows us to make a quick estimate of the dipole rf voltage V_D equivalent to the strength of a certain error field $\Delta B/B$.

5.3.2   Ion losses on resonance

As an example of on-resonance loss, let us take a look at the ion loss behavior on the integer resonance driven by the eighth harmonic, namely, the time evolution of ion losses when the LPT operating point is in the middle of the stop band at $\nu_0 = 8$. To ensure there is no systematic error in setting the primary focusing frequency, an initial tune scan is performed. The selected tune is that which produces maximum ion losses corresponding to the center of the stop band. The results of S-POD measurements are given in Fig. 5.12 together with the corresponding Warp simulation data plotted by a solid line. The abscissa is not the simple time variable but has been scaled by the amplitude w_n of the eighth dipole harmonic, because the diverging term in Eq. (5.12) is proportional to $w_n\theta_P$. Various different values of wn are considered corresponding to different strengths of a dipole error source in EMMA.

In Fig. 5.12, we have chosen wn to be sufficiently low to avoid instant ion losses. We find that the loss behavior is always similar [as predicted by Eq. (5.12)] and agrees well with the Warp simulation unless the dipole perturbation is very small. The Warp simulations were done with a much wider range of choices of w_n, but no substantial difference was found. By contrast, the experimental results with very low wn (less than 0.1 V) are clearly different from the others. The
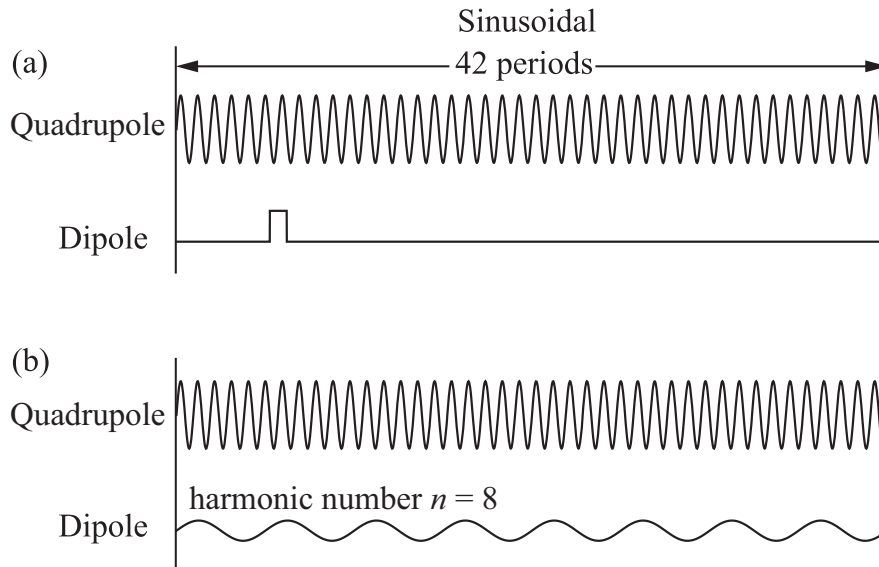
Figure 5.11: Typical waveforms of the driving rf voltages applied to the LPT electrodes. The doublet focusing is approximated by a sinusoidal waveform oscillating at 1 MHz. As for the dipole perturbation, two different rf waveforms are considered, namely, (a) a piecewise constant voltage emulating the local dipole field error such as a leakage field from the septum magnet in EMMA and (b) a sinusoidally varying voltage corresponding to a single Fourier harmonic of the pulse voltage in (a).

deviation from the ideal numerical result becomes larger as wn is lowered. This could be caused by nonlinearity of the focusing in the trap, which introduces an amplitude-dependent tune shift.

5.3.3 Single resonance crossing

We first explore what happens when the LPT operating point crosses a single integer resonance stop band. In order to see the effect from a single stop band with the single harmonic perturbation case. The integer stop band at $\nu_0 = 8$ is almost completely isolated in this case, except for a weak nonlinear resonance at $\nu_0 = 42/6$. The operating bare tune ν_0 is varied from the initial value of 9.5 down to 7.5 at various speeds. The rate of Art ions surviving after resonance crossing is plotted as a function of the crossing speed u in Fig. 5.13. Several different rf amplitudes are chosen for the dipole perturbation. Filled symbols are experimental results, while open symbols come from numerical simulations by the Warp code. The numerical data are in good agreement with the experimental observation. The slightly higher results from the simulation arise due to the sensitivity of ion loss to assumptions about the exact initial ion distribution. A similar systematic experiment of single resonance crossing was done with the twelfth harmonic w_{12} to excite another isolated stop band to cross-check this result. Essentially the same results as shown in Fig. 5.13 were obtained for crossing the stop band at $\nu_0 = 12$.

Guignard derived a formula to estimate coherent amplitude growth after a single integer reso-
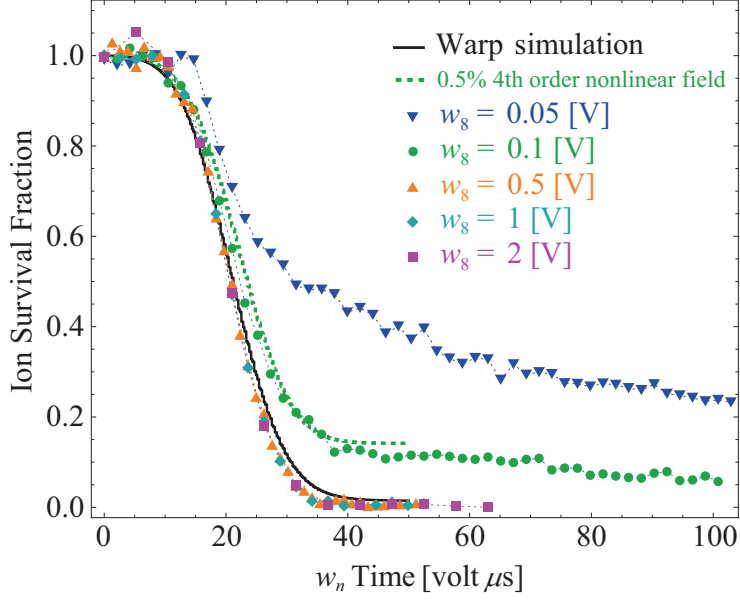
Figure 5.12: Time evolution of ion losses when the LPT operating point is fixed exactly on the integer resonance at $\nu_0 = 8$. Five different sinusoidal amplitudes are considered to change the resonance strength. The solid curve represents the corresponding Warp simulation result in which perfectly aligned quadrupole rods have been assumed, and the dashed curve where nonlinearities have been introduced. The initial plasma temperature is set at 0.5 eV.

nance crossing [60]:

$$\Delta\sqrt{\varepsilon} = \frac{\pi}{\sqrt{Q_\tau}}\frac{2R_c}{B\rho}\left|\frac{1}{2\pi}\int_0^{2\pi}\sqrt{\beta}\Delta B\exp(in\theta)d\theta\right|, \tag{5.14}$$

where ε is the amplitude of the coherent excitation of the dipole motion, Q_τ is the rate of change of tune per turn, and β is the betatron amplitude parameter. Using the relation Eq. (5.13) together with the Fourier coefficients w_n and b_n, we eventually obtain the following approximate dipole oscillation amplitude in terms of S-POD:

$$\Delta A_n = g_n^G \frac{w_n}{\sqrt{u}}, \tag{5.15}$$

$$g_n^G = \frac{q\lambda}{2\pi mc^2 R_0}\max(\beta_{\rm rf})\left|\int_0^{2\pi}\beta_{\rm rf}\sin(n\theta_P)\exp(in\theta_P)d\theta_P\right| \tag{5.16}$$

with $\beta_{\rm rf}$ defined by $\beta_{\rm rf} = (N_{\rm sp}\lambda)/2\pi R_0\beta$.

Figures 5.12 and 5.13 indicate that the numerical simulations can explain the experimental observations. This fact justifies the use of Warp or even a simpler 1D code for a quick estimate of the transverse amplitude of the plasma centroid after resonance crossing unless the nonlinear effect is too strong. The maximum centroid shifts ΔA_n numerically evaluated with various dipole perturbation strengths are plotted in Fig. 5.14 as a function of crossing speed u. The existence of
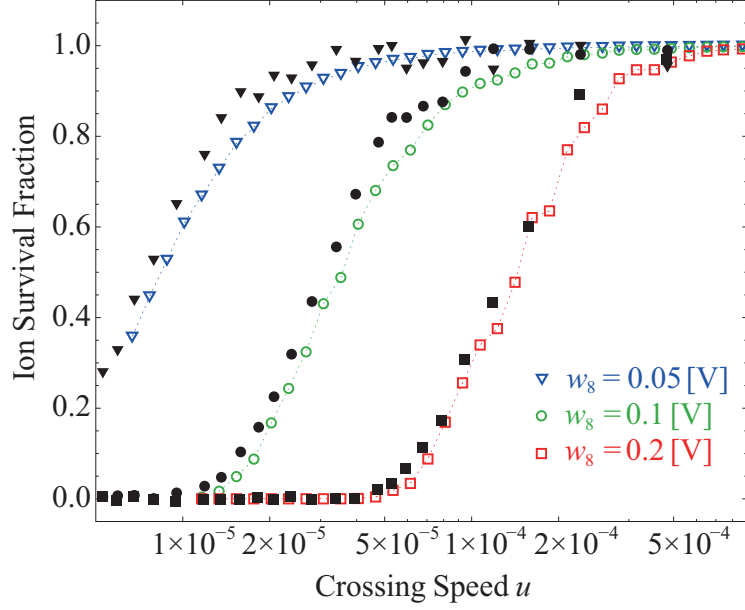
Figure 5.13: Fraction of ions remaining after integer resonance crossing. Fractional ion losses obtained with various dipole perturbation strengths are plotted as a function of crossing speed u. The bare tune ν_0 is reduced from 9.5 to 7.5. Filled and open symbols show, respectively, experimental data and Warp simulation results in which the initial ion distribution is Gaussian with a temperature of 0.5 eV.

the quadrupole electrodes is ignored in this simulation, so that we can maintain all initial particles even after the oscillation amplitude exceeds the LPT aperture size. A pure rf quadrupole focusing field is assumed to eliminate nonlinear effects. The fitting lines in Fig. 5.14 indicate that ΔA_8 scales as $\Delta A_8 = g_8 w_8/\sqrt{u}$, where the constant g_8 is close to 0.30. This is consistent with Eq. (5.15) derived without the smooth approximation [60] as well as the smooth-approximated formula in Refs. [61, 62]. Under the smooth approximation, we have the same scaling formula as Eq. (5.15) with a different coefficient, namely,

$$\Delta A_n = g_n^B \frac{w_n}{\sqrt{u}}, \tag{5.17}$$

$$g_n^B = \frac{N_{\rm sp}q\lambda^2}{4\pi mc^2 R_0} \frac{1}{n}. \tag{5.18}$$

Putting $n = 8$, we have $g_8^B = 0.20$, for example. In Fig. 5.15, we have compared this coefficient g_n^B with the nonsmoothed coefficient g_n^G and with Warp simulation results. The enhanced disagreement for a higher n value is found in g_n^B. We have confirmed that the prediction from the nonsmooth formula results in better agreement with numerical simulation results over a wide range of n value.

Figure 5.16 shows how ΔA_8 depends on the crossing speed. The solid curve is based on Guignard's formula when the maximum dipole oscillation amplitude reaches the LPT aperture of 5
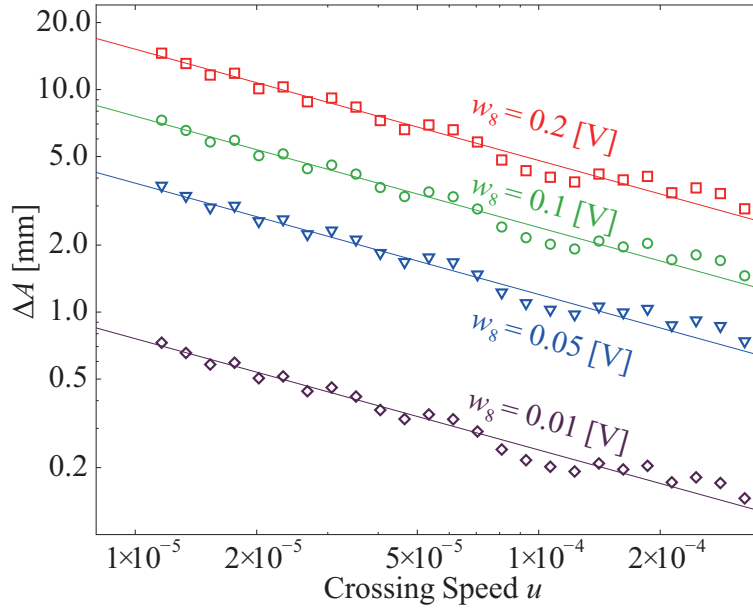
Figure 5.14: Numerical results obtained from 2D Warp simulations without space-charge inter-actions and external nonlinear fields. The maximum transverse amplitude of an ion plasma after crossing the integer resonance stop band at $n = 8$ is plotted as a function of crossing speed u.
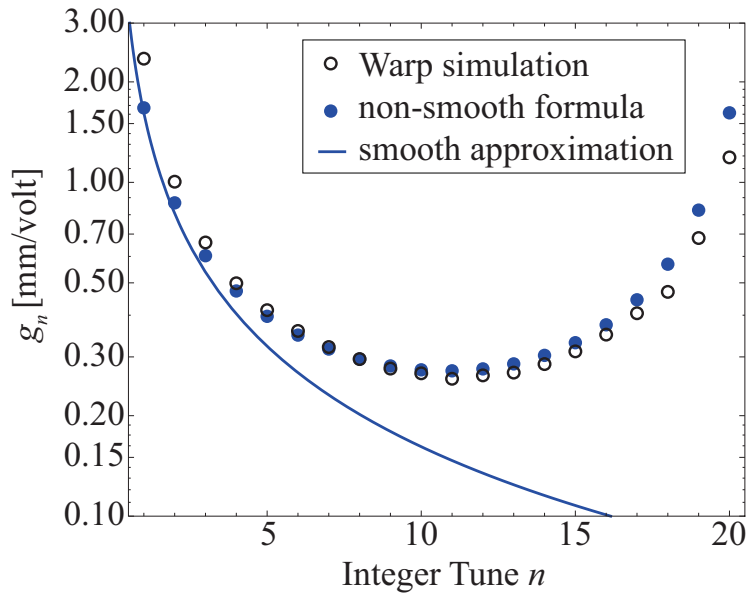
Figure 5.15: Comparison of the coefficient g_n^G in the nonsmoothed scaling formula (5.15) and g_n^B in the smoothed scaling formula (5.17). The values of g_n^G at different harmonic numbers n are plotted with black dots. The solid line comes from the definition of g_n^B in Eq. (5.17). Open circles represent the corresponding Warp simulation results.

mm. Results of S-POD measurements are plotted with black dots. Here, the experimental critical
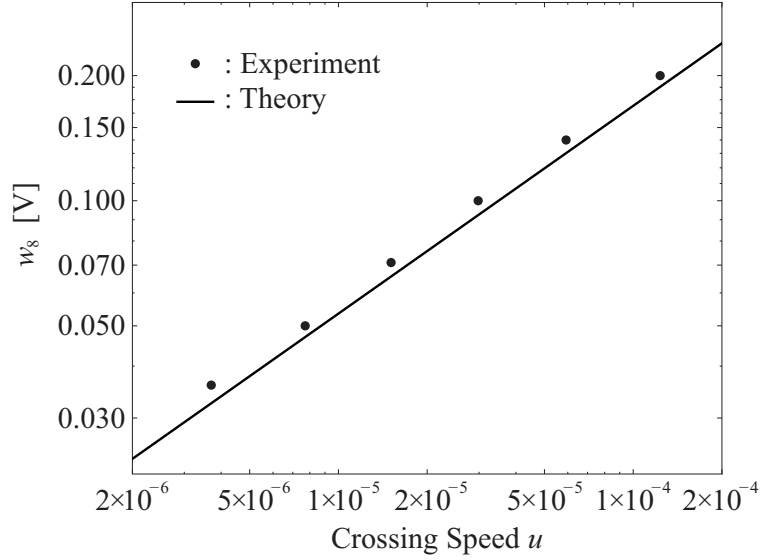
Figure 5.16: Crossing-speed dependence of the critical perturbation voltage at which the maximum transverse shift of the plasma centroid reaches 5 mm (the LPT aperture) after single resonance crossing at $\nu_0 = 8$. The solid curve is a theoretical estimate with the nonsmooth formula. Black dots are experimental data from S-POD.

perturbation voltage corresponding to the centroid of plasma oscillations reaching the aperture limit of 5 mm in S-POD is estimated from the experimental ion loss at a particular crossing speed as follows: As the plasma centroid starts to oscillate on an integer resonance, the plasma is scraped by the two horizontal electrodes. Since the oscillation frequencies of individual ions are identical to that of the plasma centroid oscillation about the trap axis, the ions remain in synchronous rotation about the trap axis. Therefore, roughly half of the ions confined in the LPT should hit the electrode surface when the horizontal shift of the original plasma approaches the aperture size (5 mm in radius). The black dots in Fig. 5.16 represent the measured perturbation voltage V_D at which 50% of initial ions are lost after crossing the stop band at $\nu_0 = 8$. We confirm that the theoretical estimate from Eq. (5.15) agrees fairly well with S-POD data.

5.3.4   Double resonance crossing

In practice, the operating point of a NS-FFAG crosses not one but more likely several integer stop bands. It is thus important to ask whether any new features appear when a few stop bands are crossed consecutively. Previous simulation studies have shown interesting beam behavior expected in multiple resonance crossing in which the phase of errors may not add and in some instances may even cancel [63]. To investigate this issue systematically, we now introduce the ninth dipole harmonic in addition to the eighth considered in the last section. The amplitudes of both harmonics are always set equal here for simplicity.

Numerical simulations based on a simple linear focusing model have shown strong oscillatory dependence of ion losses on the crossing speed as shown in Fig. 5.17, and the centroid oscillation
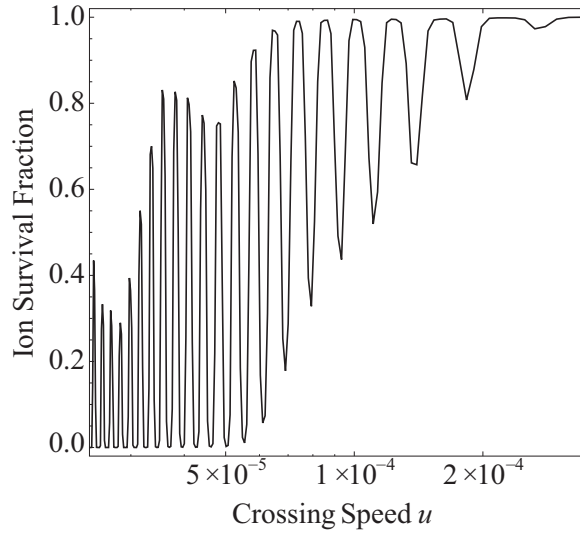
Figure 5.17: Ion loss simulation results of double resonance crossing in the absence of external field nonlinearity and space charge. The relative phase between the eighth and ninth dipole harmonics has been fixed at $0°$ and the amplitudes are $w_{8,9} = 0.05$ V in this example.
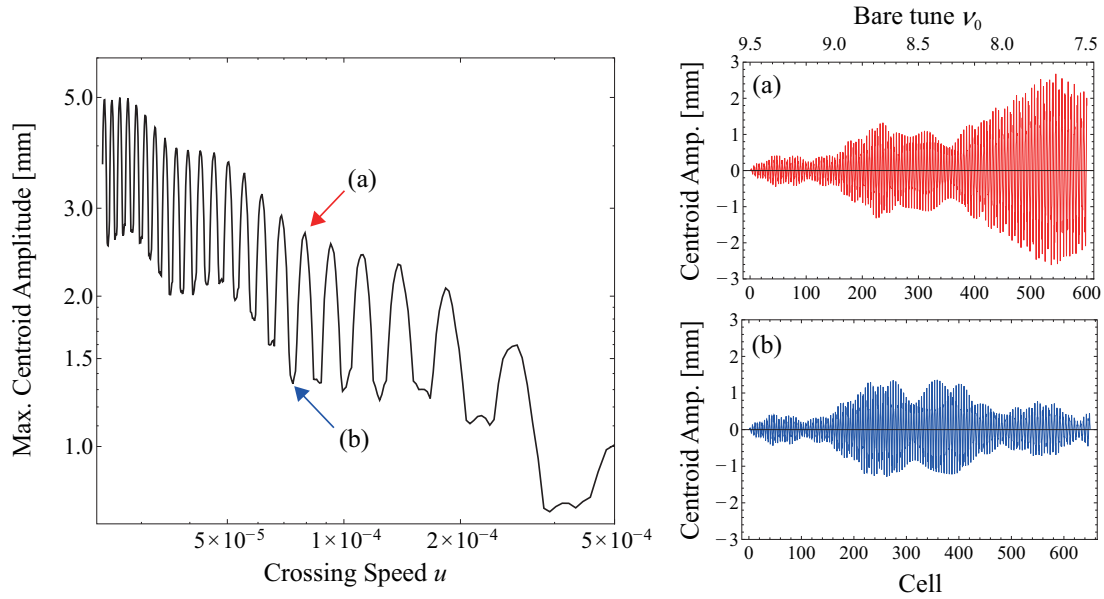
Figure 5.18: Centroid oscillation of double resonance crossing. The simulation parameters are the same as Fig. 5.17. (a) is the promotion condition of the centroid oscillation and (b) is the suppression condition.

amplitudes are shown in Fig. 5.18. When the second kick is given at the optimal timing, the ion losses from the second resonance crossing can be suppressed almost completely. Such a favorable effect can, however, be expected only when the external nonlinearity is negligible.

We made a conjecture that the amplitude of the coherent oscillation excited by the first integer
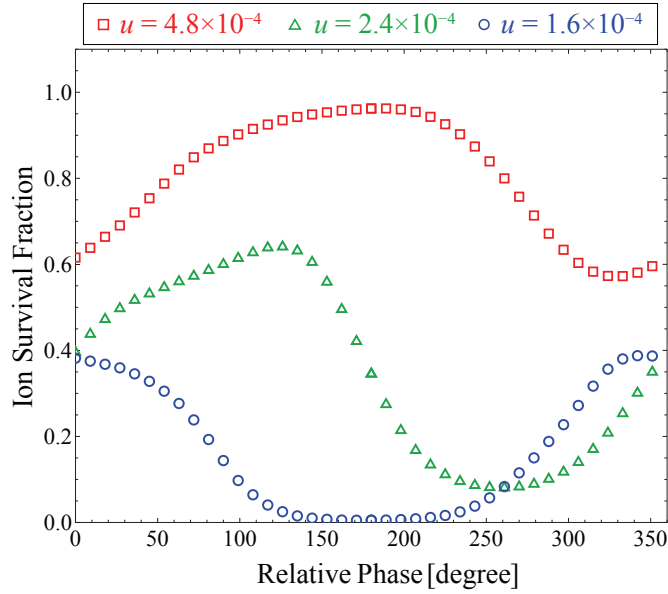
Figure 5.19: Dependence of the ion survival fraction on the relative initial phase of the two sinusoidal dipole perturbations of a fixed strength. Three different speeds of resonance crossing are considered with the Warp simulation, namely, $u = 1.6 \times 10^4$, $u = 2.4 \times 10^4$, and $u = 4.8 \times 10^4$. The amplitudes of the eighth and ninth dipole harmonics are fixed at 0.2 V.

resonance crossing could be subsequently enhanced or reduced depending on the phase of the coherent oscillation when the beam comes to the second integer resonance. To investigate this more thoroughly, the dependence on the relative initial phase was investigated numerically for a fixed perturbation with varying crossing speed in Fig. 5.19. The abscissa represents the relative initial phase of the two sinusoidal dipole perturbation waves. The relative phase of zero degrees means that both perturbations start to grow from zero voltage at the same time. A period of oscillation is observed in the ion survival fraction, which depends on the relative phase between the first and second integer resonances, confirming the idea that observed ion loss fluctuates depending on the phase relation. With a fixed crossing speed, the ion survival fraction depends on the dipole perturbation strength, as expected, but also the relative phase as seen in Fig. 5.20. In the best case, the effects of resonance crossing could be almost cancelled even with a sizable dipole perturbation such as 0.2 V if the relative phase between the two resonances is arranged to be 190°.

5.3.5 Summary

In summary, we have first verified the theory of integer resonance crossing over a wide range of resonance strengths and crossing speeds. We have found that the mechanism of resonance crossing in terms of parameter dependence agrees with previous analytical works. Additionally, we have found that the relative advance in the betatron phase between consecutive integer tunes needs to be considered when determining effects of amplitude growth from multiple resonance crossing. Nonlinear effects either due to the alignment of the trap in S-POD or due to chromaticity
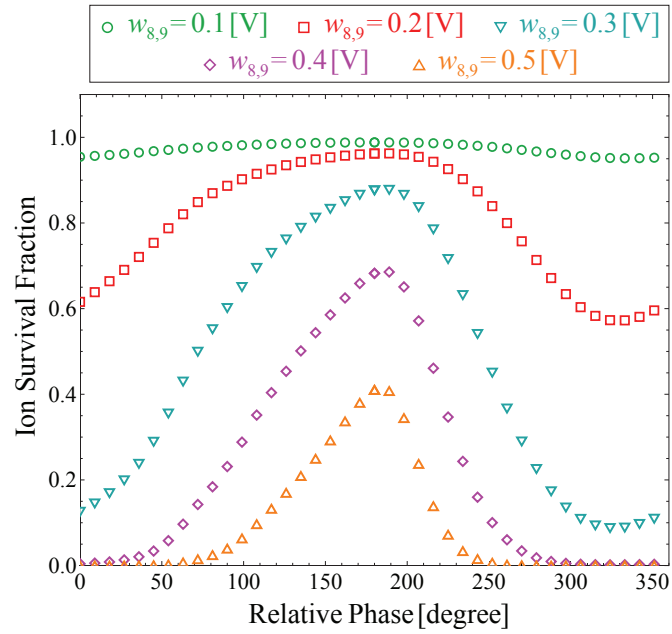
Figure 5.20: Dependence of ion losses on the relative initial phase of the two sinusoidal dipole perturbations of various strengths (Warp simulation). The crossing speed has been fixed at $u = 1.6 \times 10^4$.

and momentum spread in a FFAG are unavoidable. This means there is an interplay between the relative phase effects and nonlinear effects which will result in a real emittance growth after integer crossing, not just the excitation of dipole oscillations. As such, when the decoherence time is short relative to the traversal time from one integer to another, cancellation from consecutive excitations cannot be expected. The interplay between these various effects needs to be considered in the design of proton and ion NS-FFAGs or other accelerators that routinely perform integer resonance crossing.

Chapter 6

Design study of a modified Paul trap for nonlinear beam dynamics

The Paul trap is composed of four metallic rods symmetrically placed around the trap axis to provide an rf quadrupole field for transverse ion confinement. The collective motion of confined ions obeys the Hamiltonian Eq. (2.55). We now explicitly introduced the nonlinear perturbing potential δV originating from artificial errors

$$H = \frac{p_x^2 + p_y^2}{2} + \frac{1}{2}K(\tau)(x^2 - y^2) + \delta V(x, y; \tau) + \frac{q}{mc^2}\phi_{\text{sc}}(x, y; \tau), \qquad (6.1)$$

where the independent variable has been scaled from time t to $\tau = ct$ with c being the speed of light, ϕ_{sc} is the scalar potential of the Coulomb self-field generated by the ions, and the function $K(\tau)$ is proportional to the rf voltage applied to the quadrupole rods.

While the weak potential δV is usually ignored in standard textbooks [5], it does exist in a real trap, enhancing nonlinear resonances under certain conditions. Such a nonlinear potential is also present in any particle accelerator that always has finite mechanical imperfections and even nonlinear multipole magnets for beam orbit correction [1]. In a LPT, the main source of δV is the misalignments of the quadrupole rods. The non-hyperbolic surfaces of the rods can be another source of weak nonlinearity. In any case, the quadrupole electrodes give rise to not only the linear focusing potential but also the nonlinear perturbing potential. This means that it is impossible to control the strength of δV independently of the focusing field. In an accelerator, the time structures of $K(\tau)$ and $\delta V(\tau)$ are not necessarily identical; there is no direct correlation between these two functions especially when $\delta V(\tau)$ comes from correction magnets.

The purpose of this study is to show a possible design of a multipole ion trap optimized for a wider range of beam dynamics studies than the regular Paul trap. The proposed modified Paul trap has extra electrodes that enable us to control the strengths and time structures of low-order nonlinear fields separately from the linear focusing potential. We employ the Warp code throughout this design study to analyze the multipole field in the trap [26]. Although Warp is known as a Particle-In-Cell simulation code, it also has the function of an efficient Poisson solver. We here
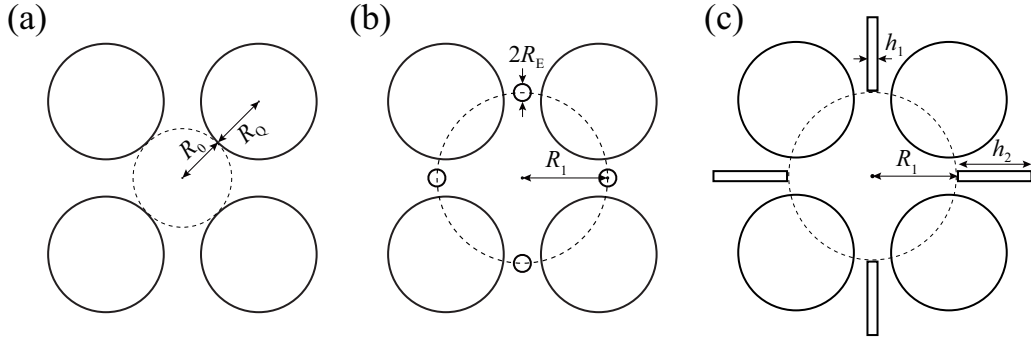
Figure 6.1: Cross sectional views of linear Paul traps. (a) regular Paul trap, (b) a modified Paul trap with extra multipole rods of radius R_E, (c) a modified Paul trap with extra planar electrodes of thickness h_1 and width h_2. The minimum distance from the trap axis to the quadrupole electrodes' surfaces is denoted as R_0 while R_1 stands for the distance to either (b) the center of each extra rod or (c) the edge of each extra plate.

numerically seek for the best conceptual design of the multipole trap, clarifying the dependence of nonlinear-field components on the electrode geometry.

6.1 Extra electrodes for nonlinear-field excitation

Fig 6.1(a) is a transverse cross section of a typical linear Paul trap with quadruple electrodes approximated by cylinders of radius R_Q. Extra electrodes should be small to avoid distortion of the linear focusing field. In addition, our purpose is to control of the sextupole and octupole nonlinearities. Fig 6.1(b) shows the case of extra electrodes formed from small cylinders between the quadrupole cylinders. However, a flat plate electrodes as illustrated in Fig 6.1 (c) are more practical. The reasons for this is difficult to accurately support a long tiny rod precisely. When $R_0 = 5$ mm, which is typical radius of our trap system, two neighboring quadrupole rods separated by a distance of only 3.7 mm.

Note also that we usually use an electron gun to ionize neutral atoms and inject an electron beam from side of transverse section within the trap aperture for non-neutral plasma production. Therefore, too thick an extra electrode is not acceptable. The diameter of the extra rods in Fig 6.1(b) should be 1 millimeter order. Such a thin wire is easy to bent, it causes longitudinal asymmetry of the plasma confinement field. From these technical considerations, we here adopt the trap geometry as illustrated in Fig. 6.1(c). It is actually easier to insert and fix a thin plate rather than a thin wire. The thickness and radial width of the four planar electrodes are denoted by h_1 and h_2, respectively. Each plate is symmetrically set the distance R_1 away from the trap axis. R_1 must be greater than the aperture radius R_0 ; otherwise, the number of ions we can confine in the trap is considerably reduced due to collisions with the plates. These extra plates are electrically isolated from each other, so that we can apply arbitrary rf voltages generated by independent power sources.

6.2 Optimization of the extra electrodes

The rf wavelength at the typical S-POD operating frequency f_{rf} of 1 MHz is roughly 300 m, much greater than the overall dimension of the Paul trap. We can thus employ the static-field approximation to analyze the transverse multipole fields with a specific design of electrodes. The scalar potential ϕ_{rf} of the plasma confinement field can be expressed as $\phi_{\text{rf}}(x,y;t) = F(x,y)T(t)$ where $F(x,y)$ satisfies the Laplace equation whose general solution written with the polar coordinates (r, θ) is

$$F(r, \theta) = \sum_{n=1}^{\infty} W_n \left(\frac{r}{R_0} \right)^n \cos(n\theta + \varphi_n) \tag{6.2}$$

with W_n and φ_n being constant parameters. In a standard sinusoidal excitation of the quadrupole electrodes, the time-dependent part is simply given by $T(t) = \cos(2\pi f_{\text{rf}}t + \text{const.})$. In beam physics applications, $T(t)$ is generally a periodic step function whose waveform emulates the discrete lattice structure of a particular machine. The quadrupole focusing potential corresponds to the $n = 2$ term in Eq. (6.2). The second multipole coefficient W_2 is, therefore, much larger than any other coefficients. A question now is how to control the coefficients of the sextupole ($n = 3$) and octupole ($n = 4$) terms by using the planar electrodes.

6.2.1 Suppression of nonlinear multipole components

The applicability of the S-POD system to various experimental purposes ought to be maintained even after a regular four-rod-type trap is replaced by the modified multipole trap. The potential δV must be weakened rather than enhanced when we wish to explore any beam dynamic effects where nonlinear driving forces are of no substantial importance. Conveniently, the extra electrodes are usable to improve the linearity of the plasma confinement field despite that they are originally introduced for nonlinearity enhancement. In an ideal Paul trap with no fabrication errors and no extra electrodes, W_6 is the lowest nonlinear coefficient that inevitably appears due to the symmetry of the trap structure. We can minimize the magnitude of W_6 by requiring $R_Q/R_0 \approx 1.15$ [64]. The ratio W_6/W_2 can then be made on the order of 10^{-4}. The planar electrodes shown in Fig. 6.1(c) can further reduce this ratio if we carefully choose their radial position and thickness.

If these extra plates are infinitely thin and inserted precisely in the middle of two neighboring quadrupole rods, they do not disturb the original electric field as long as they are grounded. That is obvious because the existence of such grounded plates has no influence on the boundary condition imposed by the original Paul-trap geometry. In reality, the plate thickness is finite, which distorts the original electric field and enhances W_6/W_2. Since the plates cannot be too thin from the viewpoint of precision machining and alignment, we here assume $h_1 = 1$ mm for example. We also assume temporarily that the plates are very wide ($h_2 \to \infty$). Figure 6.2 (b) shows the ratio W_6/W_2 plotted as a function of the radial position R_1 of the plates. W_6 has been completely eliminated at $R_1 \approx 8.5$ mm. It is always possible to find a similar operating condition for a different choice of
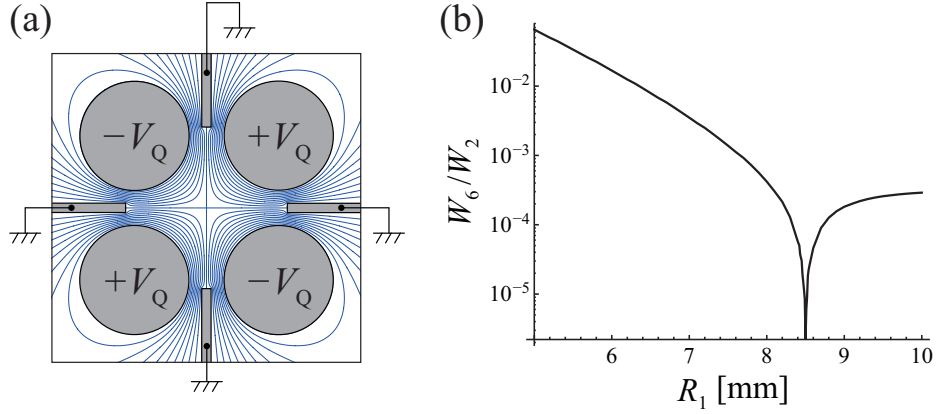
Figure 6.2: Electrodes' potentials in the normal operating mode where low-order nonlinearities are minimized. The left panel shows the equipotential lines when all four extra plates are grounded. The voltages of quadrupole symmetry are given to the four circular rods for transverse ion confinement. The plate thickness is chosen to be $h_1 = 1$ mm. The R_1-dependence of the ratio W_6/W_2 is plotted in the right panel.
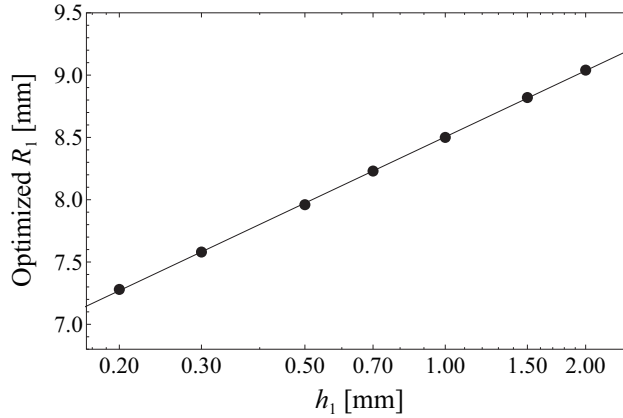
Figure 6.3: Calculation results of the Warp field solver with $R_0 = 5$ [mm] and the fitted line. W_6 is completely eliminated on the line.

h_1. The optimum value of R_1 at which W_6 vanishes fulfills the simple scaling law

$$\frac{R_1}{R_0} = 1.948 + 0.153 \log \frac{h_1}{R_0} \tag{6.3}$$

under the condition $R_Q/R_0 = 1.15$. Figure 6.3 shows the fitting result of Eq. (6.3).

We reasonably expect that this conclusion will approximately hold even if the plate width h_2 is finite. The position of the inner edge, namely, R_1 is definitely important, but on the other hand, the outer edge must have only little effect on the field within the trap aperture unless h_2 is too small. We have confirmed that in the present case, the aperture field is insensitive to h_2 if it exceeds about

80

4 mm. In the following discussion, therefore, we ignore the effect of the outer edge for simplicity, assuming that h_2 has been chosen sufficiently large.

6.2.2 Octupole control mode

We now investigate how to control low-order nonlinear components. It is easy to strengthen the octupole ($n = 4$) nonlinearity because the modified trap has four extra poles. W_4 can be made larger by applying equal potentials to the planar electrodes. Every four multipole components ($W_4, W_8, W_{12}, \cdots$) are then generated due to the symmetry of the boundary condition, but W_4 is much greater than other coefficients. The solid curves in Fig. 6.4(a) represent the equipotential lines when an identical voltage V_O is given to each plate. Figure 6.4(b) indicates the relative octupole strength achievable with the potential configuration in the left panel. W_4 is normalized by the quadrupole strength $\widetilde{W_2}$ in the normal operating mode shown in Fig. 6.2(a)[1]. The abscissa stands for the voltage ratio V_O/V_Q. The normalized magnitude of W_8 is also plotted for reference. When V_O is comparable to the linear focusing voltage V_Q, the magnitude of the octupole coefficient becomes a few percent of $\widetilde{W_2}$. This level of fourth-order nonlinearity is more than enough for a systematic study of octupole imperfection effects in a particle accelerator. The octupole field can be further strengthened by the use of thinner plates if necessary. According to Warp calculations, W_4 scales as

$$W_4/\widetilde{W_2} \approx 0.0166 \times (h_1/R_0)^{-0.441}, \tag{6.4}$$

when $V_O/V_Q = 1$, and the fitting result of Eq. (6.4) is shown in Fig. 6.5.

The strengths of nonlinear components are almost unchanged even if we excite the quadrupole rods simultaneously with the planar electrodes. The total electric field when the quadrupole rods also have the finite voltages $\pm V_Q$ is simply the superposition of the field in Fig. 6.2(a) and that in Fig. 6.4(a). This is because the sum of these two independent fields satisfies the same boundary condition as the total field has to do. Suppose that there are N independent electrodes of arbitrary cross sections fixed at certain transverse positions. Each electrode is assumed to have a constant voltage V_i ($i = 1, 2, \cdots, N$). The total static potential generated by these electrodes can be decomposed into N terms as $F(x, y) = \sum_{i=1}^{N} \psi_i(x, y)$ where ψ_i is the scalar potential derived from the Laplace equation under the boundary condition that all electrodes except for the i-th one are grounded. This is evident because the sum $\sum_{i=1}^{N} \psi_i$ is still a solution to the Laplace equation and satisfies the proper boundary condition.

6.2.3 Sextupole control mode

The effective excitation of the sextupole field is a bit tricky. Unlike the octupole control mode in Fig. 6.4(a), we need to add finite voltages not only to the planar electrodes but also to the

---

[1]In the following, we use the notation $\widetilde{W_2}$ for the quadrupole strength under the *normal operating condition* (Fig. 6.2) to distinguish it from W_2 of other operating modes; $\widetilde{W_2}$ is identical to W_2 of the normal operating mode with V_Q equalized either to V_O in Fig. 6.4 or to V_S in Fig. 6.6. Note that W_2 is zero in the nonlinearity control modes without electrodes' misalignments.
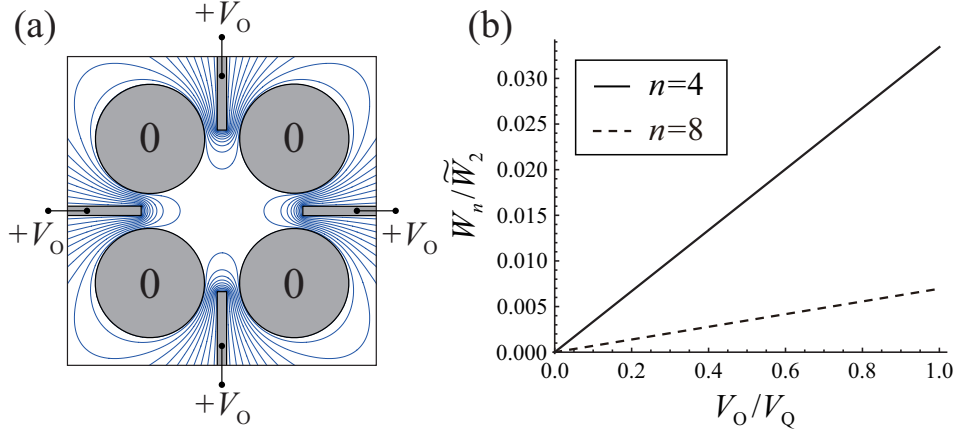
Figure 6.4: Electrodes' potentials in the octupole control mode. The left panel shows the equipotential lines when the four planar electrodes are given equal voltages V_O. All four quadrupole rods are grounded. The right panel shows the octupole strength W_4 normalized by $\widetilde{W_2}$, i.e. the quadrupole strength of the normal operating mode when $V_O/V_Q = 1$. The plate thickness is chosen to be $h_1 = 1$ mm. For reference, $W_8/\widetilde{W_2}$ is also plotted with a broken line.
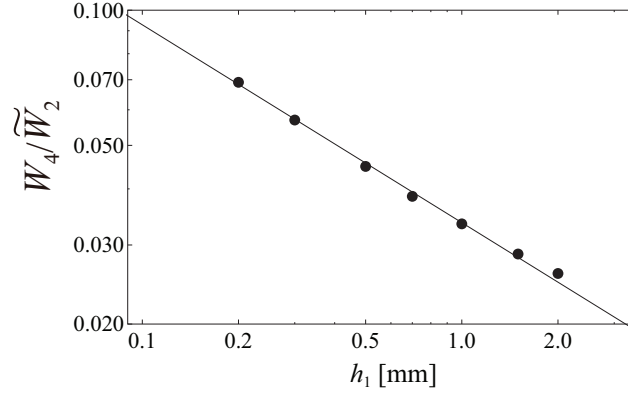
Figure 6.5: Calculation results of the Warp field solver with $R_0 = 5$ [mm] and the fitted line. $W_4/\widetilde{W_2}$ becomes larger as h_1 becomes smaller, because the inner radius R_1 changes according to Eq. (6.3).

quadrupole rods. Figure 6.6(a) shows an example of the boundary condition that allows us to enlarge the coefficient W_3. The potentials V_S of opposite signs are given to the horizontal plates while the vertical pair is grounded. In addition to $\pm V_S$, we apply the voltages $\pm V_{SQ}$ to the quadrupole rods as depicted. This electrode excitation pattern gives rise to every other multipole components. Particular attention must be paid to the dipole component W_1 because its order is the lowest. Fortunately, W_1 can be minimized in the vicinity of the trap's mechanical center by adjusting the ratio V_{SQ}/V_S. As is clear from Fig. 6.6(b), the dipole component disappears when $V_{SQ}/V_S \approx 0.02$. The
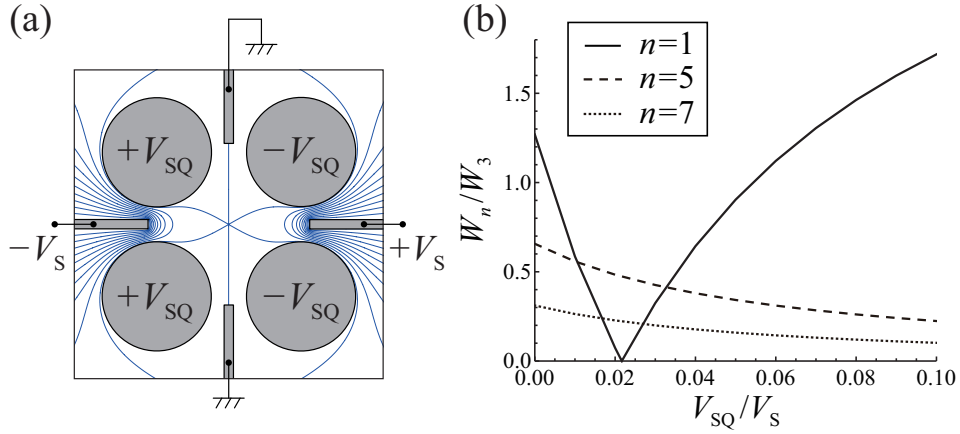
Figure 6.6: Electrodes' potentials in the sextupole control mode. The left panel shows the equipotential lines when the voltages $\pm V_{SQ}$ and $\pm V_S$ are applied to the quadrupole and horizontal planar electrodes for sextupole enhancement. The strengths of other low-order multipole components relative to the sextupole strength are plotted in the right panel as a function of the voltage ratio V_{SQ}/V_S. The plate thickness is chosen to be $h_1 = 1$ mm.
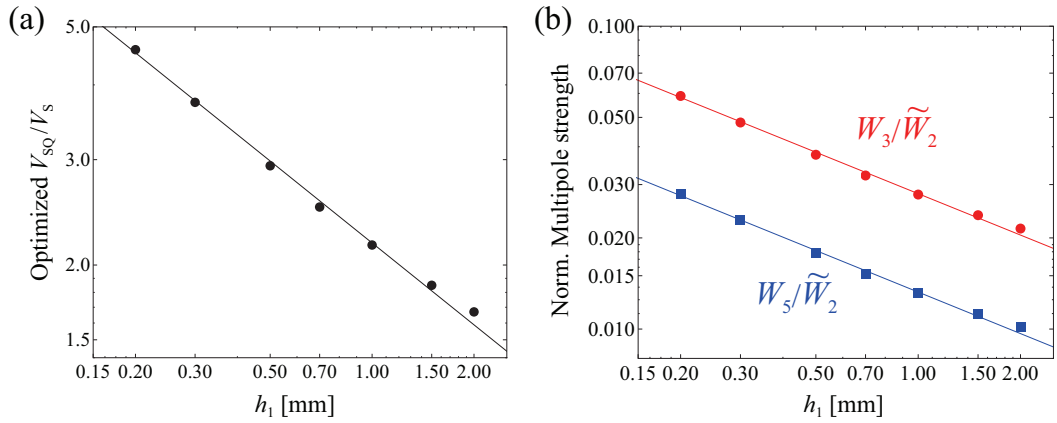
Figure 6.7: Calculation results of the Warp field solver with $R_0 = 5$ [mm] and the fitted line. (a) The optimum voltage ratio required for the minimization of W_1. (b) Normalized multipole strength of $W_3/\widetilde{W}_2$ and $W_5/\widetilde{W}_2$ assuming $V_Q = V_S$.

optimum voltage ratio required for the minimization of W_1 obeys the scaling law

$$\frac{V_{SQ}}{V_S} \approx 1.048 \times \left(\frac{h_1}{R_0}\right)^{-0.455}, \tag{6.5}$$

if the quadrupole rods are designed to satisfy the condition $R_Q/R_0 = 1.15$ and the four plates are fixed at the radial positions defined by Eq. (6.3). Figure 6.7(a) is the fitting result of Eq. (6.5).

The strengths of the sextupole ($n = 3$) and decapole ($n = 5$) components divided by the quadrupole strength $\widetilde{W}_2$ in the normal operating mode are evaluated in Fig. 6.8 under the con-
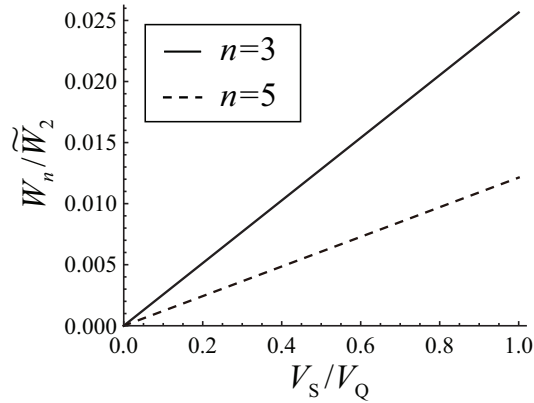
Figure 6.8: Strengths of sextupole ($n = 3$) and decapole ($n = 5$) fields vs. the potential ratio V_S/V_Q in the sextupole control mode. V_{SQ} has been adjusted to the optimum value required by the condition (6.5) to eliminate the dipole component W_1. The coefficients W_3 and W_5 are normalized by the quadrupole strength $\widetilde{W_2}$ evaluated under the normal operating condition with $V_Q = V_S$.

dition in Eq. (6.5). By increasing V_S to the same level of V_Q, W_3 becomes a few percent of $\widetilde{W_2}$. We have also found how these nonlinearities scale as a function of the plate thickness h_1. Provided that V_{SQ}/V_S satisfies the condition (6.5), the relative strengths follow the scaling laws $W_3/\widetilde{W_2} \approx 0.0135 \times (h_1/R_0)^{-0.454}$ and $W_5/\widetilde{W_2} \approx 0.0064 \times (h_1/R_0)^{-0.456}$ (see Fig. 6.7(b)) where we have assumed $V_Q = V_S$ as an example. Interestingly, the three ratios V_{SQ}/V_S, $W_3/\widetilde{W_2}$ and $W_5/\widetilde{W_2}$ have roughly the same power dependence on the geometric factor h_1/R_0.

6.2.4 Extra electrodes of a cylindrical shape

The basic feature of the multipole field within the trap aperture does not essentially change even if we replace the planar electrodes in Fig. 6.1(c) by the small circular rods in Fig. 6.1(b). Apart from a technical question of which trap geometry is easier to fabricate, the electric-field properties of both designs turn out to be very similar to each other. First of all, W_6 can be eliminated in the normal operating mode by adjusting the radius R_E of the extra rods. The scaling law in this case is given by

$$\frac{R_1}{R_0} = 2.162 + 0.225 \log \frac{R_E}{R_0} \tag{6.6}$$

instead of Eq. (6.3). In the octupole control mode, we simply apply an identical voltage V_O to all four extra rods just like the previous case in Fig. 6.4(a). When V_O is set equal to the quadrupole focusing voltage V_Q on the main rods, the octupole coefficient W_4 relative to the dominant quadrupole coefficient $\widetilde{W_2}$ scales as $W_4/\widetilde{W_2} \approx 0.0153 \times (R_E/R_0)^{-0.558}$. It is also possible in the sextupole control mode to minimize the dipole component near the trap axis. The optimum ratio of V_{SQ} and V_S for dipole suppression can be determined from the scaling law $V_{SQ}/V_S \approx 0.963 \times (R_E/R_0)^{-0.577}$.

6.3 Effect of electrodes' misalignments

It is important to figure out how the ideal multipole fields calculated in the last section are affected by the misalignments of the electrodes. Such an artificial error is unavoidable in practice, which results in considerable enhancement of all nonlinear fields. To check this error-induced effect, we randomly shift all electrodes about the ideal positions, and then, expand the resultant electric field into multipole components.

Table 6.1 summarizes the relative multipole strengths (%) in various operating modes explained in the last section. "Regular Paul trap" has the ordinary four-rod structure illustrated in Fig. 6.1(a). The "normal operating mode" corresponds to the electrode excitation pattern in Fig. 6.2(a) where all extra plates are grounded. We have assumed that V_S in the "sextupole control mode" and V_O in the "octupole control mode" are equal to V_Q in the "normal operating mode". V_{SQ} in the "sextupole control mode" is automatically determined from Eq. (6.5) once we choose V_S. The normalization constant $\widetilde{W_2}$ is evaluated under the boundary condition of the normal operating mode. Note that the centroid of an ion plasma in the trap is located at the multipole-field center where the dipole component vanishes. We, therefore, need to expand the scalar potential about the field center (instead of the original mechanical center) to make a reasonable estimate of W_n. We have here defined the field center under the boundary condition of the normal operating mode because the plasma is exposed to this strong focusing potential most of the time. The possible error-induced shift of the field center is on the order of 0.1 mm at most even with relatively large electrodes' misalignments; the maximum shift was actually 0.11 mm in Case II. This number is much smaller than the aperture size of 5 mm. As the transverse extent of an ion plasma confined in our trap is typically around 1 mm in radius, no extra ion losses will occur due to such a tiny shift of the plasma centroid.

The multipole coefficients in Table 1 are obtained by averaging a hundred independent Warp data based on a hundred different sets of random numbers to define the electrode positions. The quadrupole and planar electrodes are misaligned simultaneously. Two different sizes of root-mean-squared (rms) errors, i.e. 50 μm (Case I) and 100 μm (Case II), are considered in the table. As expected, all multipoles have been excited by the misalignments. The standard deviation of an error-induced multipole coefficient calculated from the one hundred samples is somewhat smaller than its central value listed in the table. The rms shifts of the plasma centroid are 31 μm for Case I and 63 μm for Case II. It is quite reasonable that the nonlinear fields become stronger on average as the rms alignment error increases. We recognize from the data in Table 6.1 that the magnitudes of low-order multipole coefficients grow almost linearly with respect to the rms error size. A practically important fact is that the introduction of the four extra plates does not deteriorate the field quality of the original Paul trap without the plates. The strengths of low-order nonlinear components caused by the error are insensitive to whether we add the four misaligned plates or not.

It is informative to point out that the extra electrodes may be utilized to reduce the low-order error-induced nonlinear fields in the normal operating mode. $W_3/\widetilde{W_2}$ is typically on the order of 0.1% as suggested in Table 1. This unwanted third-order component can be suppressed strongly by

Table 6.1: Multipole strengths in various operating modes. The multipole coefficients normalized by the quadrupole strength $\widetilde{W_2}$ (normal operating mode) are indicated in percent. It has been assumed that $V_S = V_Q$ in the sextupole control mode and $V_O = V_Q$ in the octupole control mode. The aperture size $R_0 = 5$ [mm], which determines the optimum radius of the quadrupole rods to be 5.75 [mm]. The thickness of the planar electrodes has been fixed at $h_1 = 1$ [mm]. The multipole expansion is carried out about the electric-field center (where $W_1 = 0$) defined in the normal operating mode. The dipole component then becomes non-zero in the sextupole and octupole control mode because the location of the field center slightly shifts when finite voltages are applied to the misaligned plates.

		$W_1/\widetilde{W_2}$	$W_2/\widetilde{W_2}$	$W_3/\widetilde{W_2}$	$W_4/\widetilde{W_2}$	$W_5/\widetilde{W_2}$	$W_6/\widetilde{W_2}$	$W_7/\widetilde{W_2}$	$W_8/\widetilde{W_2}$
Regular Paul trap	No error	0	100	0	0	0	0.032	0	0
	Case I	0	100	0.358	0.125	0.065	0.038	0.011	0.013
	Case II	0	100	0.715	0.251	0.130	0.056	0.021	0.027
Multipole trap (normal operating mode)	No error	0	100	0	0	0	0	0	0
	Case I	0	100	0.358	0.125	0.071	0.029	0.014	0.016
	Case II	0	100	0.716	0.250	0.143	0.058	0.029	0.033
Multipole trap (sextupole control mode)	No error	0	0	2.565	0	1.213	0	0.570	0
	Case I	0.093	0.074	2.567	0.054	1.215	0.026	0.571	0.010
	Case II	0.185	0.148	2.571	0.108	1.216	0.052	0.572	0.019
Multipole trap (octupole control mode)	No error	0	0	0	3.343	0	0	0	0.695
	Case I	0.135	0.087	0.106	3.349	0.051	0.032	0.030	0.697
	Case II	0.269	0.174	0.212	3.349	0.102	0.064	0.060	0.697

superimposing proper low voltages to all electrodes. These additional voltages for error-induced sextupole minimization are decomposed into two specific potential configurations; one is the configuration in Fig. 6.6(a) and the other the skew sextupole configuration obtained by rotating Fig. 6.6(a) by 90 degrees around the axis. Since the ratio V_{SQ}/V_S satisfies Eq. (6.5), we have only two free parameters, i.e. the voltage V_S in each configuration, to be adjusted. The optimum values of V_S's can be determined easily if the size and direction of each electrode's misalignment are known. Figure 6.9 is the minimization example of W_3 which is generated by the misalignment. We can find the sextupole component is reduced after the optimization of V_{SQ}^{normal} and V_{SQ}^{skew}. Such information about actual mechanical errors is indeed unknown, but we can at least measure the ion-loss rate due to sextupole resonance with many different combinations of the additional voltages. The data of systematic ion-loss measurements enable us to find the optimum V_S's for sextupole minimization. Those data also tell us how much mechanical errors are actually contained in the trap. Note that, Experimental simulations of intense beam dynamics by means of the S-POD system are far faster than any multi-particle computer simulations. An ion-loss measurement based on a particular AG focusing waveform is completed typically within ten seconds, regardless of the plasma density. In addition, the whole experimental process is automated, so we do not have to stay beside S-POD to retune fundamental parameters. Even if we execute a hundred independent measurements at a hundred different operating points, that takes only less than 17 minutes.
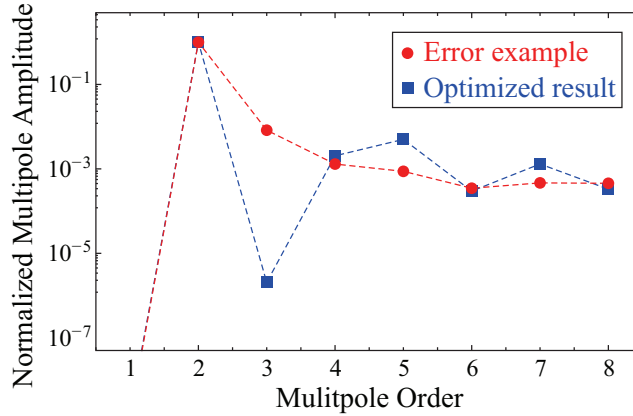
Figure 6.9: Calculation results of the Warp field solver. Red dots are the multipole strengths by the misaligned rods. Blue dots are the optimized result due to eliminate the sextupole component. In this example, we choose $V_S^{normal}/V_Q = -0.275$ and $V_S^{skew}/V_Q = 0.173$.

6.4 Particle tracking simulation

A major advantage in S-POD experiment is the high flexibility of the focusing function $K(\tau)$. In a particle accelerator, the lattice design uniquely determines the form of $K(\tau)$. If we wish to explore beam dynamics in a different lattice, we must construct another large-scale machine. By contrast, $K(\tau)$ can be modified over a wide range in S-POD because the rf voltages applied to the electrodes determines the external driving potential, in other words, this is just a matter of the electronics system. In the multipole ion trap, $K(\tau)$ is proportional to the quadrupole voltage V_Q in Fig. 6.2(a). The upper picture in Fig. 6.10 represents a typical rf waveform for V_Q imitating a so-called "FODO" channel. The rf power supply system developed for S-POD can readily produce much more complex waveform if necessary.

The extra planar electrodes of the multipole trap make it feasible for us to introduce a nonlinear periodic perturbation independently of the main focusing waveform. In the case of Fig. 6.10, the plates are excited every three FODO cells (the lower picture); namely, the period of $\delta V(\tau)$ in Eq. (6.1) is chosen three times longer than that of $K(\tau)$. This kind of situation commonly takes place in a circular machine where a small number of nonlinear magnets are added for beam orbit correction. Since the periodicities of the linear and nonlinear driving forces are different, we expect additional resonance stop bands to appear, depending on how often we turn on the nonlinear perturbation. In the present example, the nonlinearity of a particular order ($n = 3$ or 4) is considerably enhanced every three FODO periods. The stability threshold of the bare betatron tune ν_0 per lattice period is then 1.5 ($= 0.5 \times 3$). At zero beam intensity, the well-known incoherent resonance condition can be written as $n\nu_0 = m$ where n is the order of resonance, and m is a positive integer. We have assumed here that the horizontal tune ν_x and the vertical tune ν_y are equal, i.e. $\nu_x = \nu_y = \nu_0$, for the sake of simplicity while it is possible in S-POD to separate the two transverse tunes.

We performed test numerical simulations with the Warp code to verify the resonance condition,
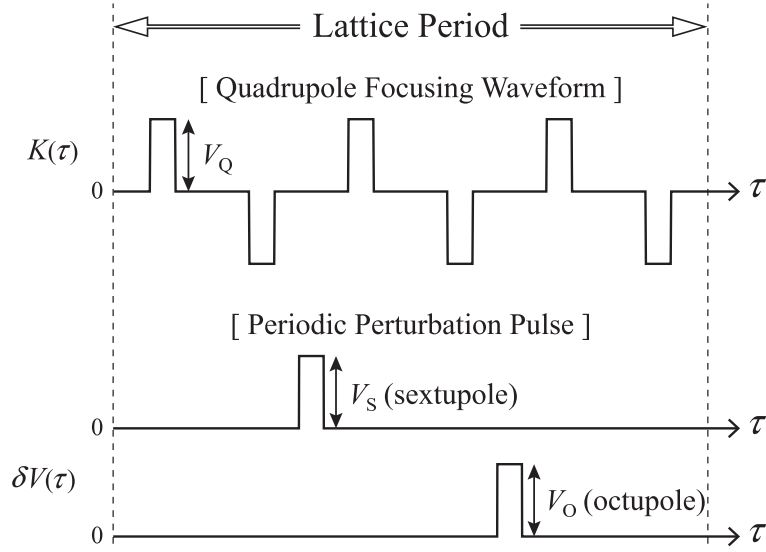
Figure 6.10: An example of the rf waveform emulating a FODO beam transport channel. The quadrupole filling factor is chosen to be 0.25. The lower picture indicates the timing when the octupole potential (V_O) in Fig. 3(a) or the sextupole potential (V_S and V_{SQ}) in Fig. 4(a) is switched on for nonlinearity enhancement. Each nonlinear perturbation pulse is excited every three FODO periods. The widths of all pulses are taken identical.

incorporating the detailed multipole field distributions evaluated in the previous sections. The time evolution of the rms emittance of an ion plasma in the multipole trap was computed assuming the rf waveform in Fig. 6. The emittance growth rates after a hundred FODO cells are plotted in Fig. 6.11 as a function of the bare tune ν_0. The solid line in each panel is obtained from Warp simulations in the absence of electrode alignment errors, while the broken line shows a typical case where all electrodes are randomly shifted by the rms average of 100 μm. The repetition frequency of a FODO waveform is set at 1 MHz, so the hundred cells correspond to 100 μs in an actual experiment. Figure 6.10(a) shows the Warp output obtained under the normal operating condition. We confirm that in the absence of the perturbation pulse, no resonance occurs over the whole tune range because the external force is perfectly linear in the modified trap without electrode misalignments (see Table 6.1). Serious instability can, however, be identified near $\nu_0 = 1$ when the electrodes are misaligned. This is due to the third-order resonance (the lowest-order nonlinearity) caused by the imperfection field. No other stop bands of higher order resonances are visible within a hundred FODO periods, except for a very weak fourth-order instability at $\nu_0 = 3/4$. Needless to say, the emittance growth rate depends on how the electrodes are misaligned. In this simulation, we have shifted all eight electrodes so that the averaged multipole coefficients of Case II (normal operating mode) in Table 6.1 are approximately reproduced.

Once the perturbation pulse is excited, the emittance growth picture becomes essentially different. Figure 6.11(b) represents the case where the sextupole potential in Fig. 6.6(a) is periodically switched on. The pulse height of the perturbation wave has been adjusted to satisfy $V_S = V_Q$ in each simulation. We observe clear instabilities at $3\nu_0 = m$, no matter whether the misalignments
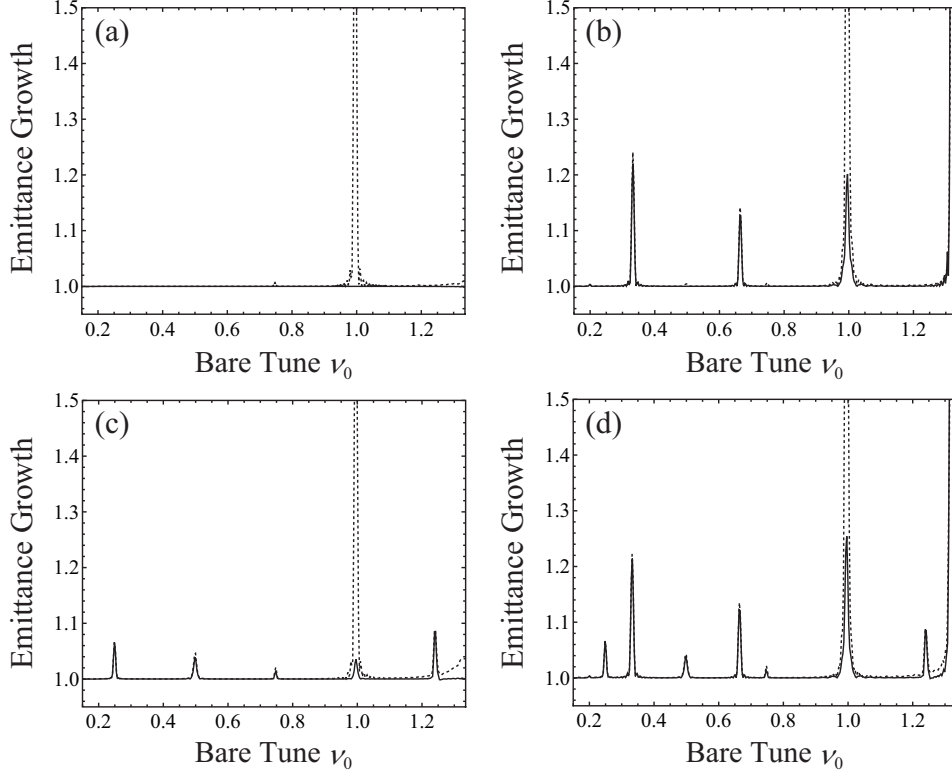
Figure 6.11: Warp simulation results assuming the time structures of $K(\tau)$ and $\delta V(\tau)$ in Fig. 6.10. The rms emittance growth rates after 100 FODO periods are plotted as a function of bare betatron tune ν_0. The Coulomb self-field potential has been ignored in these simulations. The panel (a) is the result under the normal operating condition where no perturbation pulse is excited. Other three panels correspond to the cases where we periodically switch on (b) only the sextupole pulse under the condition $V_S = V_Q$, (c) only the octupole pulse under the condition $V_O = V_Q$, and (d) both sextupole and octupole pulses.

are finite. The emittance behavior is changed to Fig. 6.11(c) by applying the octupole pulses instead of the sextupole pulses. We now observe small peaks at $4\nu_0 = m$ due to the fourth-order resonance. Figure 6.11(d) shows what happens when both sextupole and octupole perturbations are activated. Naturally, stop bands are generated at $3\nu_0 = m$ and $4\nu_0 = m$.

It is also possible to selectively drive only one sextupole or one octupole resonance at a specific tune. For this purpose, we use a sinusoidal waveform for $\delta V(\tau)$ instead of a stepwise pulse as in Fig. 6.10. The frequency of the sinusoidal perturbation has to be matched to that of a proper Fourier harmonic of the original periodic pulse.

6.5 Summary

We have proposed a simple design of a multipole ion trap dedicated to fundamental beam-physics experiments with the S-POD system. The modified Paul trap has four extra electrodes in between

the regular quadrupole rods, which control low-order nonlinearities in the plasma confinement potential. From a practical point of view, we focused our discussion on the insertion of thin metallic plates. An efficient Poisson solver was employed to study the dependence of the aperture field on the electrode geometry. It has been shown that the sextupole and octupole driving fields can be enhanced independently of the quadrupole focusing potential. In the so-called normal operating mode (Fig. 6.2), the modified trap operates just like an ordinary LPT; the field linearity can even be improved by placing the extra plates at the optimum positions defined by Eq. (6.3). The octupole field can be strengthened at an arbitrary moment simply by applying the same voltages to the four plates (Fig. 6.4). In the sextupole control mode, we excite the planar electrodes and quadrupole rods simultaneously in such a way as illustrated in Fig. 6.6. The applied voltages are chosen to minimize the dipole component according to Eq. (6.5).

When the electrodes are shifted from their ideal positions due to mechanical imperfections, all higher order components become finite. Such error-induced multipole fields are, however, sufficiently weak as long as the electrode misalignments are within a reasonable level. As shown in Table 1, the four extra plates newly introduced for nonlinearity control do not affect the field quality of the original Paul trap. Numerical simulations actually demonstrate that we can create the third- and/or fourth-order stop bands at specific tunes without enhancing unwanted resonances of other orders. The present design of a multipole ion trap thus widens the range of beam dynamics experiments we can do with the S-POD system. In particular, the stability of intense hadron beams in a variety of nonlinear lattices can be explored experimentally and much more quickly than any numerical simulations.

On the basis of this design study, we are now planning to construct a multipole ion trap for S-POD. The nominal operating frequency will be set at 1 MHz, the same as the existing Paul traps at Beam Physics Laboratory of Hiroshima University. The aperture radius R_0 is 5 mm, and then, the radius R_Q of the quadrupole rods has to be 5.75 mm. The thickness h_1 of the four extra plates is probably chosen 1 mm or less. In case $h_1 = 1$ mm, the inner edge of each plate is fixed 8.5 mm away from the trap axis, according to Eq. (6.3). The plate width h_2 should be greater than at least about 5 mm, so that the effect of the outer edge on the aperture field becomes negligible. Under these mechanical conditions, the sextupole and octupole strengths can be increased to a few percent of the dominant quadrupole strength with a perturbation voltage (V_S or V_O) of lower than about 100 V. The required perturbation voltage can be further lowered, if necessary, by using thinner plates[2]. In any case, we only need minor modifications to the current power-supply system of S-POD for future experimental studies of intense beam dynamics with the modified Paul trap.

---

[2]Then, the optimum radial position of the inner edge comes closer to the aperture radius R_0, according to Eq. (6.3).

References

[1] H. Okamoto and H. Tanaka, Nucl. Inst. Meth. A **437**, 178 (1999).

[2] H. Okamoto, Y. Wada, and R. Takai, Nucl. Instr. Meth. A **485**, 244 (2002).

[3] R. Takai *et al.*, Jpn. J. Appl. Phys. **45**, 5332 (2006).

[4] S. Ohtsubo *et al.*, Phys. Rev. ST – Accel. Beams **13**, 044201 (2010).

[5] R. P. Ghosh, *Ion Traps* (Oxford Science, Oxford, 1995).

[6] E. D. Courant and H. S. Snyder, Annals of Physics **3**, 1 (1958).

[7] S. Y. Lee, *Accelerator Physics* (World Scientific, NJ, 1999).

[8] Liouville, J. Math. Pures Appl. **3**, 342 (1838).

[9] I. Kapchinskij and V. Vladimirskij, Limitations of proton beam current in a strong focusing linear accelerator associated with the beam space charge, in *Proceedings of the International Conference on High Energy Accelerators and Instrumentation*, p. 274, CERN Scientific Information Service, Geneva, 1959.

[10] M. Reiser, *Theory and Design of Charged Particle Beams* (John Wiley & Sons, New York, 1994).

[11] I. Hofmann, L. J. Laslett, L. Smith, and I. Haber, Particle Accelerators **13**, 145 (1983).

[12] R. C. Davidson, *Physics of Nonneutral Plasmas* (Addison-Wesley, Reading, MA, 1990), Re-released, World Scientific, 2001, and references therein.

[13] R. C. Davidson and H. Qin, *Physics of Intense Charged Particle Beams in High Energy Accelerators* (World Scientific, New York, 2001), and references therein.

[14] R. L. Gluckstern, W.-H. Cheng, and H. Ye, Phys. Rev. Lett. **75**, 2835 (1995).

[15] I. Hofmann, Phys. Rev. E **57**, 4713 (1998).

[16] F. J. Sacherer, *Transverse Space-Charge Effects in Circular Accelerators*, PhD thesis, University of California, 1968.

[17] F. J. Sacherer, CERN Report No. Tech. Rep. No. CERN-SI-INT-DL-70-5, 1970 (unpublished).

[18] F. J. Sacherer, IEEE Trans. Nucl. Sci. **18**, 1105 (1971).

[19] R. C. Davidson, H. Qin, and G. Shvets, Phys. Plasma **7**, 1020 (2000).

[20] E. P. Gilson, R. C. Davidson, P. C. Efthimion, and R. Majeski, Phys. Rev. Lett. **92**, 155002 (2004).

[21] E. P. Gilson *et al.*, Phys. Plasmas **20**, 055706 (2013).

[22] J. P. Boris, in *Proceedings of the Fourth Conference on the Numerical Simulation of Plasmas, Nov 2-3*, pp. 3–67, 1970.

[23] S. M. Lund, T. Kikuchi, and R. C. Davidson, Phys. Rev. ST – Accel. Beams **12**, 114801 (2009).

[24] A. Freidman, D. P. Grote, and I. Haber, Phys. Fluids B **4**, 2203 (1992).

[25] D. P. Grote, *Three Dimensional Simulations of Space Charge Dominated Heavy Ion Beams with Applications to Inertial Fusion Energy*, PhD thesis, University of California at Davis, 1994.

[26] D. P. Grote, A. Friedman, G. D. Craig, I. Haber, and W. M. Sharp, Nucl. Inst. Meth. A **464**, 563 (2001).

[27] D. P. Grote, A. Friedman, I. Haber, and S. Yu, Fusion Eng. Design **32-33**, 193 (1996).

[28] D. P. Grote, A. Friedman, I. Haber, W. Fawley, and J.-L. Vay, Nucl. Inst. Meth. A **415**, 428 (1998).

[29] For more information, see http://warp.lbl.gov/ .

[30] For more information, see https://www.python.org/ .

[31] For more information, see http://www.scipy.org/ .

[32] For more information, see http://matplotlib.org/ .

[33] H. Sugimoto, *Multi-Particle Simulation Studies on the Generation and Stability of High-Density Coulomb Systems*, PhD thesis, 2011.

[34] M. Venturini and R. L. Gluckstern, Phys. Rev. ST – Accel. Beams **3**, 034203 (2000).

[35] H. Okamoto and K. Yokoya, Nucl. Instr. Meth. A **482**, 51 (2002).

[36] S. M. Lund and B. Bukh, Phys. Rev. ST – Accel. Beams **7**, 024801 (2004).

[37] S. Machida *et al.*, Nature **8**, 243 (2012).

[38] J. Wei, H. Okamoto, and A. M. Sessler, Phys. Rev. Lett. **80**, 2606 (1998).

[39] Y. Yuri and H. Okamoto, Phys. Rev. ST – Accel. Beams **8**, 114201 (2005).

[40] C. Johnstone, W. Wan, and A. Garren, in *Proceedings of the 18th Particle Accelerator Conference, New York, TN*, p. 3068, IEEE, New York, 1999, 1999.

[41] R. Barlow *et al.*, Nucl. Inst. Meth. A **624**, 1 (2010).

[42] S. Machida and D. J. Kelliher, Phys. Rev. ST – Accel. Beams **10**, 114001 (2007).

[43] E. Keil and A. M. Sessler, Nucl. Inst. Meth. A **538**, 159 (2005).

[44] E. Keil, A. M. Sessler, and D. Trbojevic, Phys. Rev. ST – Accel. Beams **10**, 054701 (2007).

[45] D. Trbojevic, E. D. Courant, and M. Blaskiewicz, Phys. Rev. ST – Accel. Beams **8**, 050101 (2005).

[46] S. L. Sheely, K. J. Peach, H. Witte, D. J. Kelliher, and S. Machida, Phys. Rev. ST – Accel. Beams **13**, 040101 (2010).

[47] C. Johnstone, M. Berz, K. Makino, S. Koscielniak, and P. Snopok, Int. J. Mod. Phys. A **26**, 1690 (2011).

[48] N. Madsen *et al.*, Phys. Rev. Lett. **83**, 4301 (199).

[49] K. Okabe and H. Okamoto, Jpn. J. Appl. Phys. **42**, 4584 (2003).

[50] S. Machida, Phys. Rev. ST – Accel. Beams **11**, 094003 (2008).

[51] S. Y. Lee, G. Franchetti, I. Hofmann, F. Wang, and L. Yang, New J. Phys. **8**, 291 (2006).

[52] S. Y. Lee, Phys. Rev. Lett. **97**, 104801 (2006).

[53] M. Aiba, S. Machida, Y. Mori, and S. Ohnuma, Phys. Rev. ST – Accel. Beams **9**, 084001 (2006).

[54] S. Machida, Nucl. Phys. Proc. Suppl. **155**, 332 (2006).

[55] K. Ito, S. Ohtsubo, H. Higaki, K. Izawa, and H. Okamoto, J. Plasma Fusion Res. **8**, 959 (2009).

[56] M. Reiser, *Theory and Design of Charged Particle Beams* (John Wiley & Sons, New York, 1994), and references therein.

[57] J. Struckmeier and M. Reiser, Part. Accel. **14**, 227 (1984).

[58] A. V. Fedotov, I. Hofmann, R. L. Gluckstern, and H. Okamoto, Phys. Rev. ST – Accel. Beams **6**, 094201 (2003).

[59] H. Okamoto *et al.*, Nucl. Inst. Meth. A **733**, 119 (2014).

[60] G. Guignard, Intersecting Storage Rings Division Report No. CERN 77-10 (1977).

[61] R. Baartman, in *Proceedings of the FFAG Workshop, Vancouver, B. C., Canada*, 2004.

[62] S. Koscielniak and R. Baartman, in *Proceedings of the 21st Particle Accelerator Conference, Knoxville, TN*, p. 3206, IEEE, Piscataway, NJ, 2005, 2005.

[63] S. R. Mane and W. T. Weng, Nucl. Inst. Meth. A **306**, 9 (1991).

[64] D. R. Denison, J. Vacuum Sci. Technol. **8**, 266 (1971).

[65] H. Okamoto, A. M. Sessler, and D. Möhl, Phys. Rev. Lett. **72**, 3977 (1994).

[66] X. P. Li *et al.*, Phys. Rev. ST – Accel. Beams **9**, 034201 (2006).

[67] S. Machida and M. Ikegami, Simulation of space charge effects in a synchrotron, in *Proceedings of the Workshop on Space Charge Physics in High Intensity Hadron Rings*, p. 73, American Institute of Physics, New York, 1998.

[68] H. Okamoto and S. Machida, Nucl. Inst. Meth. A **482**, 65 (2002).

[69] S. M. Lund and S. R. Chawla, Nucl. Inst. Meth. A **561**, 203 (2006).

[70] L. Verlet, Phys. Rev. **159**, 98 (1967).

[71] R. Takai, *Development of a Linear Paul Trap System as a Beam-dynamics Simulator*, PhD thesis, 2007.

[72] K. Okabe, *Theoretical study of space charge effects in high density ion beams*, PhD thesis, 2005.

[73] K. Izawa, *Feasibility study of the nano-ion-beam generator using Coulomb crystals in a linear Paul trap*, PhD thesis, 2011.

公表論文

(1) Experimental study of resonance crossing with a Paul trap
Hiroki Takeuchi, <u>Kei Fukushima</u>, Kiyokazu Ito, Katsuhiro Moriya, Hiromi Okamoto and Hiroshi Sugimoto
Physical Review Special Topics - Accelerators and Beams **15**, 074201, pp. 1 - 14 (2012).

(2) Experimental verification of resonance instability bands in quadrupole doublet focusing channels
<u>Kei Fukushima</u>, Kiyokazu Ito, Hiromi Okamoto, Shisei Yamaguchi, Katsuhiro Moriya, Hiroyuki Higaki, Toshihiro Okano and Steven M. Lund
Nuclear Instruments and Methods in Physics Research Section A **733**, pp. 18 - 24 (2014).

(3) Design study of a multipole ion trap for beam physics applications
<u>Kei Fukushima</u> and Hiromi Okamoto
Plasma and Fusion Research **10**, 1401081, pp. 1 - 9 (2015).

参考論文

(1) Theoretical study on the stability of Coulomb crystallized beams in periodic focusing channels
Kei Fukushima, Hiromi Okamoto and Hiroshi Sugimoto
Proceedings of the 8th Annual Meeting of Particle Accelerator Society of Japan, pp. 1134 - 1137 (2011).

(2) Plasma traps for space-charge studies: status and perspectives
Hiromi Okamoto, Masahiro Endo, Kei Fukushima, Hiroyuki Higaki, Kiyokazu Ito, Katsuhiro Moriya, Toshihiro Okano, Shisei Yamaguchi and Akihiro Mohri
Proceedings of the 52nd ICFA Advanced Beam Dynamics Workshop on High-Intensity and High-Brightness Hadron Beams (HB2012), pp. 235 - 239 (2012).

(3) Experimental studies of resonance crossing in linear non-scaling FFAGs with the S-POD plasma trap
Suzanne L. Sheehy, David J. Kelliher, Shinji Machida, Chris R. Prior, Kei Fukushima, Kiyokazu Ito, Katsuhiro Moriya, Toshihiro Okano and Hiromi Okamoto
Proceedings of the 4th International Particle Accelerator Conference (IPAC2013), pp. 2675 - 2677 (2013).

(4) Experimental simulation of beam propagation over long path lengths using radio-frequency and magnetic traps
Hiromi Okamoto, Masahiro Endo, Kei Fukushima, Hiroyuki Higaki, Kiyokazu Ito, Katsuhiro Moriya, Shisei Yamaguchi and Steven M. Lund
Nuclear Instruments and Methods in Physics Research Section A **733**, pp. 119 - 128 (2014).

(5) Beam dynamics studies with non-neutral plasma traps
Hiromi Okamoto, Kei Fukushima, Hiroyuki Higaki, Daiki Ishikawa, Kiyokazu Ito, Takaaki Iwai, Katsuhiro Moriya, Toshihiro Okano, Kazuya Osaki and Mikio Yamaguchi
Proceeding of the 5th International Particle Accelerator Conference (IPAC2014), pp. 4052 - 4056 (2014).

(6) Study of resonance crossing in non-scaling FFAGs using the S-POD linear Paul trap
David J. Kelliher, Shinji Machida, Chris R. Prior, Suzanne L. Sheehy, Kei Fukushima, Kiyokazu Ito, Katsuhiro Moriya, Hiromi Okamoto and Toshihiro Okano
Proceeding of the 5th International Particle Accelerator Conference (IPAC2014), pp. 1571 - 1573 (2014).

(7) Recent results from the S-POD trap systems on the stability of intense hadron beams
Hiromi Okamoto, Kiyokazu Ito, <u>Kei Fukushima</u> and Toshihiro Okano
Proceeding of the 54th ICFA Advanced Beam Dynamics Workshop on High-Intensity, High-Brightness and High-Power Hadron Beams (HB2014), pp. 178 - 182 (2014).

(8) Experimental study of integer-resonance crossing in a non-scaling fixed field alternating gradient accelerator with a Paul ion trap
Katsuhiro Moriya, <u>Kei Fukushima</u>, Kiyokazu Ito, Toshihiro Okano, Hiromi Okamoto, Suzanne L. Sheehy, David J. Kelliher, Shinji Machida and Chris R. Prior
Physical Review Special Topics - Accelerators and Beams **18**, 034001, pp. 1 - 13 (2015).

(9) Experimental study on dipole motion of an ion plasma confined in a linear Paul trap
Kiyokazu Ito, Toshihiro Okano, Katsuhiro Moriya, <u>Kei Fukushima</u>, Hiroyuki Higaki and Hiromi Okamoto
Hyperfine Interactions, DOI 10.1007/s10751-015-1196-y, 9 pages (2015).